COMPUTER SIMULATIONS FOR IMPROVED ATOMIC-LEVEL CONTROL AND UNDERSTANDING OF MOLECULAR ELECTRONIC DEVICES

By

William R. French

Dissertation

Submitted to the Faculty of the

Graduate School of Vanderbilt University

in partial fulfillment of the requirements

for the degree of

DOCTOR OF PHILOSOPHY

in

CHEMICAL ENGINEERING

May, 2013

Nashville, Tennessee

Approved:

Professor Peter T. Cummings

Professor Clare McCabe

Professor Kane Jennings

Professor Kalman Varga

To Christi, the apple of my eye,
and Granma Carolyn, whose warmth and kindness live on.

ACKNOWLEDGMENTS

The first person I want to thank is my research advisor, Professor Peter Cummings, for his invaluable guidance, and for giving me the freedom and autonomy to develop as an independent researcher. Professor Cummings's passion and enthusiasm for scientific research sparked my own excitement in the field of molecular simulation and computational nanoscience. I am also grateful to my committee members for critiquing my research and pushing me to a higher level. A big thank you goes to Dr. Chris Iacovella, whose insight and knowledge have constantly challenged me to improve my approach to research, writing, and presenting. I greatly appreciate his mentorship and credit him for much of my success in graduate school.

I appreciate the help I received from several members of the Cummings lab, especially for their practical and technical advice when I first entered the lab. These people include Dr. Hugh Docherty, Dr. Junhwan Jeon, Dr. Adam Skelton, Dr. Michael Rouha, and Li Wan. My collaborators in physics are also deserving of credit, as my background is not in quantum mechanics and I therefore leaned on them heavily for guidance in this area of my project. These people include Dr. Brandon Cook, who previously worked with Professor Kalman Varga in the Physics and Astronomy Department at Vanderbilt, and, more recently, Dr. Ivan Rungger, Amaury Melo Souza, and Professor Stefano Sanvito at Trinity College in Dublin, Ireland. Two undergraduate students, Amulya Pervaje and Andrew Santos, worked with me during my Ph.D., and I am grateful to them for their eagerness to learn and for their contribution to my project. I am also thankful to the ChBE administrative assistants, Mary Gilleran, Rae Uson, and Julie Canada, for helping me plan travel, coordinate reimbursement, and perform other important tasks.

I am indebted to the developers of the freely available software tools and packages that I used for my research. Without these invaluable tools much of my work would not have been possible. Thank you to the developers of LAMMPS (lead developer: Dr. Steve Plimpton), Visual Molecular Dynamics (lead developer: John Stone), SIESTA (lead developer: Dr. Pablo Ordejon), and SMEAGOL (lead developer: Dr. Alexandre Rocha). I also appreciate prior work in the Cummings group by Dr. Yongsheng Leng and Dr. Qing Pu, who developed and validated many of the tools and force fields for the molecular electronics project.

The highlight of my time at Vanderbilt was meeting my wife and best friend, Christi. We met in January 2010 and married 27 months later in Brentwood, TN. Her support during my Ph.D. has been unwavering. I cannot imagine my time in Nashville without her being a part of it. I have also developed lifelong friendships during my time at Vanderbilt. I am especially thankful for the close friendships of Jason Ballengee, Margarita Prieto, Stijn Smeets, Doris Palomino, and Svenja Hector. I am also thankful for the support and friendship of many others within and outside of the ChBE department, including Taylor Murphy, Juan Rojas, Neil Templeton, Elizabeth Adolf, Steve Vilt, Juan Tuberquia, Courtney Taylor, Carlos Escobar, John Burnam,

Niki Burnam, Chris Muller, Sudipta Chakraborty, Hank Clay, Hayley Clay, Jamie Ausborn, Laura Anzaldi, Shann Yu, Dr. Ron Zimmer, Tish Warren, Jonathan Warren, among others. My church community at Trinity Church Nashville has been an additional source of support and inspiration for the past few years. In particular I want to thank my Trinity small group: Matt Givens, Melanie Givens, Avory Givens, Will Harvey, Casey Harvey, Lara Jazmin, Cory Caswell, and Tyler Rydosz.

Thank you to all my friends and family back in Bryan/College Station, Texas. Thank you to my parents for encouraging me in my studies and for believing in me. Thank you to my brother, Doug, and sister, Phyllis, for their love, friendship, and support. Thank you also to my friend Jose, who is like a brother to me. Lastly, I want to thank my late grandmother, Carolyn Alford. Granma Carloyn was extremely supportive of my academic endeavors, and I will always appreciate and remember the warm smiles and encouraging words she shared with me.

Finally, I gratefully acknowledge financial support from the U.S. Department of Education Graduate Assistance in Areas of National Need (GAANN) Fellowship under Grant No. P200A090323 and the U.S. Department of Energy under Grant No. DEF-G0203ER46096. Computing resources were provided by the National Energy Research Scientific Computing Center, which is supported by the Office of Science of the U.S. Department of Energy, under Grant No. DOE KC0204010-ERKCZ01, the National Science Foundation through TeraGrid resources provided by Texas Advanced Computing Center and Oak Ridge National Laboratory, under Grant No. TG-DMR090099, and the National Institute for Computational Sciences, under Project-ID UT-TNEDU014.

TABLE OF CONTENTS

LIST OF TABLES

LIST OF FIGURES

LIST OF ABBREVIATIONS

ASIC approximate self-interaction corrections

BDT benezene-1,4-dithiolate

CMOS complementary metal-oxide-semiconductor

COM center of mass

DFT density functional theory

GCMC grand canonical Monte Carlo

GPU graphics processing unit

HOMO highest occupied molecular orbital

HR-TEM high-resolution tunneling electron microscopy

IETS inelastic electron tunneling spectroscopy

LAMMPS Large-scale Atomic/Molecular Massively Parallel Simulator

LJ Lennard-Jones

MAC monatomic chain

MC Monte Carlo

MCBJ mechanically controllable break-junction

MD molecular dynamics

ME molecular electronics

MJ molecular junction

NW nanowire

QM quantum mechanical

RMSD root-mean-square deviation

SAM self-assembled monolayer

SGCMC semigrand canonical Monte Carlo

SIESTA Spanish Initiative for Electronic Simulations with Thousands of Atoms

STM-BJ scanning tunneling microscopy break-junction

TB-SMA second-moment approximation to the tight binding potential

UFF universal force field

CHAPTER I

INTRODUCTION

During the last 50 years, the micro/nanoelectronics industry has followed a trend known as Moore's Law, where, as a result of the continued miniaturization of on-chip circuit elements, computing speeds have doubled every two years or so.[1] As the electronics industry approaches the end of Moore's Law,[2] new paradigms for building smaller, faster electronics are needed. Molecular electronics (ME) is one promising alternative, with essential circuit functionality (*e.g.*, switching,[3] gating,[4] rectification[5]) having been demonstrated at the single-molecule level. Reed and co-workers[6] were the first to measure the conductance through a molecular junction (MJ) when in 1997 they applied the mechanically controllable break-junction (MCBJ) method to form a MJ consisting of a single benzene-1,4-dithiolate (BDT) molecule bridged across two Au nanotips. In the MCBJ technique, a Au nanowire (NW) is first immersed in a solution of BDT, which self-assembles onto the NW surface. The NW is then elongated and ruptured, the solvent is allowed to evaporate, and the BDT-coated Au tips are brought in and out of contact with one another repeatedly, occasionally resulting in the formation of a covalently bonded Au-BDT-Au junction as detected by I-V measurements. Since the landmark study by Reed *et al.*,[6] measuring single-molecule conductance has now become a fairly routine procedure, with MJs consisting of various types of metal contacts and organic molecules having been investigated.[3–5,7–53]

While proof-of-concept devices have shown great promise, significant barriers to ME commercialization remain. The precise fabrication of large ME circuit arrays[54,55] capable of executing a set of instructions and storing bits of data is itself a formidable task. More fundamentally, however, doubts have been raised concerning the reliability of device stability[14,15,32] and reproducibility[56] on the single-molecule level. For example, the measured conductance of the same molecule varies between laboratories and for different experimental techniques,[51,56] and the measured conductance of MJs formed repeatedly between metallic electrodes can occasionally lack reproducibility.[10,25] Moreover, a long-standing discrepancy exists between the experimentally measured and theoretically calculated values of single-molecule conductance for simple organic molecules, namely BDT.[56–58]

Theoretical calculations are an indispensible tool in ME for their ability to directly correlate atomic-level structure with observables in experiment (*e.g.*, conductance). Quantum mechanical (QM) studies have greatly advanced the community's understanding of electron transport through molecules and the important factors controlling conductance. However, many calculations[57,59–63] employ unrealistic simplifications that ultimately make it difficult to connect theory and experiment. The recent incorporation of dynamic atomic

motion induced by mechanical elongation[64–67] and/or thermal effects[68–71] has extended the applicability of theoretical calculations, but many important environmental factors (*e.g.*, non-planar electrodes, temperature effects, elongation rate effects) have not yet been included. This dissertation presents results from several studies[72–76] aimed to elucidate how environmental factors impact the behavior of molecular- and atomic-scale junctions. Atomic-level modeling and simulation are used to investigate important aspects of MCBJ experiments in which proof-of-concept ME devices consisting of a single molecule bridged across fractured Au NW tips are formed.

Chapter II first outlines the history of single-molecule conductance measurements. A summary of the important theoretical advances and findings are also presented, and the role of Au NW elongation is discussed. Next, in Chapter III, a detailed account is provided of the simulation and theoretical tools applied throughout this dissertation. The development of a physically accurate and robust model is an essential design step for systems of interest in nanoscience. Previous work in the Cummings group focused on developing, testing, and validating models and methods for Au NW elongation in vacuum[77,78] and in solvent.[79–82] Chapter III details the application and extension of these methods, which are used throughout the subsequent chapters.

In Chapter IV, molecular dynamics (MD) simulations are applied to study the impact of physisorbing adsorbates on the structural and mechanical evolution of Au NWs under elongation, which is an important process in MCBJ experiments.[72] Various adsorbate models are applied in the simulations, with each model resulting in a different surface coverage and mobility of the adsorbed phase. The local structure and mobility of the adsorbed phase remains relatively uniform across all segments of an elongating Au NW, except for the thinning region of the NW where the high mobility of Au atoms disrupts the monolayer structure, giving rise to higher solvent mobility. The Au NW trajectories are analyzed by measuring the ductile elongation of the NWs and detecting the presence of characteristic structural motifs. The findings of this analysis indicate that adsorbates facilitate the formation of high-energy structural motifs and lead to significantly enhanced NW ductility. In particular, the simulations result in a large number of Au monatomic chains (MACs)[78] and helical structures possessing mechanical stability in excess of results in vacuum. Conversely, a molecular species that interacts weakly (*i.e.*, does not adsorb) with Au NWs worsens the mechanical stability of MACs.

Next, in Chapter V, hybrid MD-Monte Carlo (MC) simulations[82] are performed to examine MJs composed of BDT bonded between gold nanotips.[73] The simulations are performed using classical force fields derived from QM calculations,[80] enabling the study of much larger system sizes and longer time scales in comparison to QM studies. Additionally, molecule identity swap MC moves are incorporated to improve the sampling of the preferred metal-molecule bonding geometries. The updated hybrid MD-MC simulation tool is applied to study the importance of environmental factors and inter-electrode distance on the formation and structure of bridged molecules. First, the complex relationship between monolayer density and tip separa-

tion is investigated, with results revealing that the formation of multi-molecule junctions is counterintuitively favored at low monolayer density, while single-molecule junctions are favored at high density. Two factors that are often neglected in simulation,[8,28,31,46,59] tip geometry and monolayer interactions, are next shown to affect the bonding geometry and tilt angle of bridged BDT molecules. This is an important finding since it has been previously demonstrated that both bonding geometry and tilt angle can affect conductance by at least an order of magnitude,[11,22,50,83] while also impacting the measured inelastic electron tunneling spectra.[84] Finally, the structure of bridged molecules at 298 and 77 K are found to be similar.

Chapter VI presents results from hybrid MD-MC simulations combined with high-fidelity conductance calculations to probe structure-conductance relationships in Au-BDT-Au junctions under elongation and/or thermal motion.[74] The conductance calculations are performed using approximate self-interaction corrected (ASIC)[85] density functional theory (DFT) in combination with the Green's function method. This approach corrects the spurious self-interaction errors of standard DFT, and hence more accurately describes the energy level lineup between BDT and the Au contacts.[67,86,87] The results of the junction elongation simulations demonstrate that large increases in conductance are associated with the formation of Au monatomic chains (MACs) directly connected to BDT. An analysis of the electronic structure of the simulated junctions reveals that enhancement in the *s*-like states in Au MACs causes the increases in conductance. Other structures also result in increased conductance but are too short-lived to be detected in experiment, while MACs remain stable for long simulation times. Examinations of thermally evolved junctions with and without MACs show negligible overlap between conductance histograms, indicating that the increase in conductance is related to this unique structural change and not thermal fluctuation. These results provide an excellent explanation for a recently observed anomalous experimental result,[43] and should aid in the development of mechanically responsive molecular electronic devices.

Investigations of conductance fluctuations in thermally evolving Au-BDT-Au junctions are also presented in Chapter VI.[75] Conductance fluctuations are typically attributed to the combined motion of the molecule and electrodes,[68,71] however for highly deformed MJs the electrodes may play an increased role. Behavior from structurally ideal junctions (electrodes with flat surfaces) is compared to structurally realistic, experimentally representative junctions resulting from break-junction simulations. The enhanced mobility of metal atoms in structurally realistic junctions results in significant changes to the magnitude and origin of the conductance fluctuations. Fluctuations are larger by a factor of 2-3 in realistic junctions compared to ideal junctions. Moreover, in junctions with highly deformed electrodes, the conductance fluctuations arise primarily from changes in the Au geometry, in contrast to results for junctions with non-deformed electrodes, where the conductance fluctuations are dominated by changes in the molecule geometry. These results provide important guidance to experimentalists developing strategies to control molecular conductance for device applications,

and also to theoreticians invoking simplified structural models of junctions to predict their behavior.

In Chapter VII, the role of NW size and temperature in the failure mechanism of Au NWs is investigated.[76] A large-scale statistical analysis ($>$ 2000 independent simulations) of the elongation and rupture of Au NWs is performed, probing the validity and scope of the recently proposed ductile-to-brittle transition that occurs with increasing NW length.[88] To facilitate this, the second-moment approximation to the tight-binding (TB-SMA)[89] potential is ported to HOOMD-Blue,[90] a MD package which runs on highly parallel graphics processing units (GPUs), obtaining performance that exceeds simulations run on 64 CPU cores. Leveraging the performance of the GPU-implemented code, a large number of replicates for different NW sizes and temperatures are performed. In a statistical sense, the NWs obey the ductile-to-brittle model quite well, however, the deformation of small NWs is highly stochastic and can lead to rupture behavior that deviates from the model prediction. Additionally, temperature is shown to be a useful parameter, along with NW size, for tuning the NW failure mechanism.

Finally, Chapter VIII summarizes the main conclusions of the dissertation, and makes recommendations for future work.

CHAPTER II

BACKGROUND

2.1 Nanotechnology and Molecular Electronics

Nanotechnology is an emerging, multidisciplinary fields with potential applications in areas ranging from the physical and chemical sciences,[91] to medicine[92] and energy storage.[93] The novel and promising properties available at the nanoscale have fueled widespread nanostructured materials research over the past few decades. In extreme cases, drastically different chemical, mechanical, optical, and transport properties can emerge for a nanostructured material in comparison to its macroscopic counterpart.[94] For instance, bulk gold is a relatively inert substance, while gold nanoparticles are extremely reactive due to the increased flexibility of gold-gold bonds in low-coordination environments.[95]

The electronics industry is an area where nanotechnology has become increasingly important, with device dimensions now in the 30-nm range.[96] The fabrication of circuit components (*e.g.*, transistors, gates, memory elements) with increasingly small feature sizes over the past half century has spurred the remarkable trend known as Moore's Law,[1] in which computing speeds have doubled roughly every two years. Moore's Law has been enabled by the progress of "top-down" approaches in electronics manufacturing. Top-down in this context refers to the fabrication of circuit elements via etching into a silicon substrate using photolithography to create complementary metal-oxide-semiconductor (CMOS) chips. However, doubts are being raised about the scalability of current photolithographic techniques below the 20-nm range, and the cost of these techniques continues to increase.[97] Further decreases in feature sizes will also introduce new problems related to device reliability, such as performance that is sensitive to dopant atom placement[98,99] and quantum effects.[2] If Moore's Law is to continue, new devices must be engineered that can overcome the limited scalability of photolithography and CMOS-based devices.

ME is a field with the potential to miniaturize electronic devices beyond what is possible with current top-down approaches.[58,100–103] The concept of ME was popularized by Aviram and Ratner in 1974 when they conceived a simple molecular rectifier.[104] In ME, molecular-sized components self-assemble together from the "bottom-up" to form integrated circuit elements. The major fabrication step in ME is self-assembly, in which initially disordered molecular components spontaneously (*i.e.*, without external stimulus) arrange into their thermodynamically favored configuration, *e.g.*, the formation of an ordered, self-assembled monolayer (SAM) of organic molecules onto a metallic surface.[105–108] Self-assembly is a cheaper alternative than photolithography. ME also has the advantage of high device tunability through adjustments in the chemi-

cal configuration, size, and electrode coupling strength of the molecular building block(s). Proof-of-concept ME devices have been fabricated on the single-molecule level, with essential functionality such as switching,[25] rectification,[5] and gating[4] having been demonstrated. The ultimate miniature electronic device, a single-atom transistor, was also recently fabricated,[109] although severe practical limitations (*e.g.*, thermal instability) make it less promising than a ME device and will likely prevent its commercialization. Another advantage of ME is that devices with no analog in existing CMOS-based technology may be fabricated by harnessing the unique behavior at the nanoscale, *e.g.*, devices exhibiting single-electron phenomena[110] and mechanically induced resonant tunneling.[43]

2.2 Molecular Junctions

Single-molecule conductance measurements were pioneered by Reed and co-workers[6] in 1997. The authors used a MCBJ[111] apparatus for trapping individual (as few as one) molecules of BDT between fractured Au NW tips. The MCBJ technique was originally developed for investigating electron transport through nano- and atomic-scale metallic constrictions.[111] Reed *et al.*[6] were the first to apply the method for studying single-molecule conductance. In the MCBJ method a notched NW is attached to a long flexible beam, which is bent using a pushing rod. This exerts an elongating force onto the NW with subpicometer resolution.[112] As shown in Figure 2.1, Reed and co-workers adapted this to single-molecule measurements by first allowing

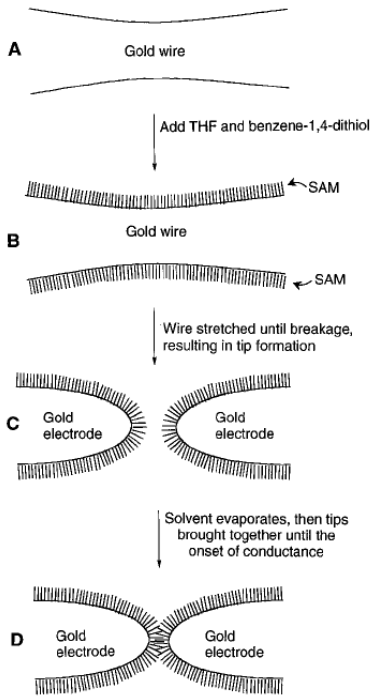

Figure 2.1. Schematic of the MCBJ process employed by Reed *et al.*[6] to form Au-BDT-Au junctions.

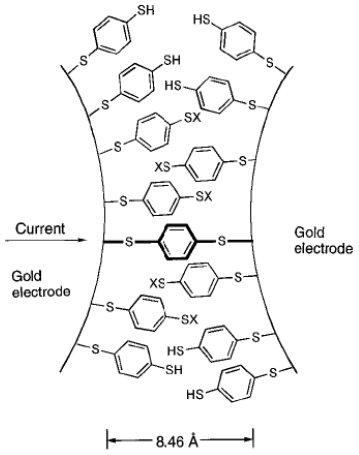

Figure 2.2. Illustration from the work of Reed *et al*.[6] of a single BDT molecule bridged across two BDT-coated Au nanotips.

BDT dissolved in tetrahydrofuran (THF) to self-assemble onto a Au NW. The NW was next elongated and ruptured, yielding two BDT-coated Au nanotips. The solvent was then evaporated and I-V data were collected as the nanotips were repeatedly brought in and out of contact. These data showed evidence of a single BDT molecule bridging between the two Au tips, as shown in Figure 2.2. Since these initial experiments, the MCBJ method has been applied to measure the conductance through a variety of organic molecules.[3,7–22]

In addition to the MCBJ method, numerous other techniques are used for measuring single-molecule conductance, including the scanning tunneling microscopy break-junction (STM-BJ),[5,10,23–43] conductive probe atomic force microscopy,[29,44–47] electromigration,[4] and $I(t)/I(s)$[48–53] methods. The most widely used approaches are the MCBJ and STM-BJ methods. Xu *et al*.[113] were among the first to apply the STM-BJ method to study single-molecule conductance. In this approach, a metallic STM tip is repeatedly driven in and out of a SAM-covered metal surface. Molecules are occasionally trapped between the tip and surface during this process. The $I(t)/I(s)$ methods are similar to the STM-BJ method except in the $I(t)/I(s)$ methods the STM tip does not contact the underlying metal surface. Instead, the STM tip is placed a small distance above a SAM-covered surface and molecules spontaneously bridge between the surface and STM tip. An illustration of the STM-BJ method is shown in Figure 2.3, along with individual conductance traces (offset along the *x*-axis) and histograms of the conductance plateaus observed during tip retraction. Histograms of large values of conductance (Figure 2.3B) show preferred peaks at integer multiples (n) of the conductance quantum (77.5 μS). These peaks are thought to correspond to the presence of n Au atoms in the junction neck for electrons to transport through. Figure 2.3D exhibits similar features on a scale that is two orders of magnitude smaller. In this case the peaks are ascribed to the presence of n molecules connected in parallel between the STM tip and

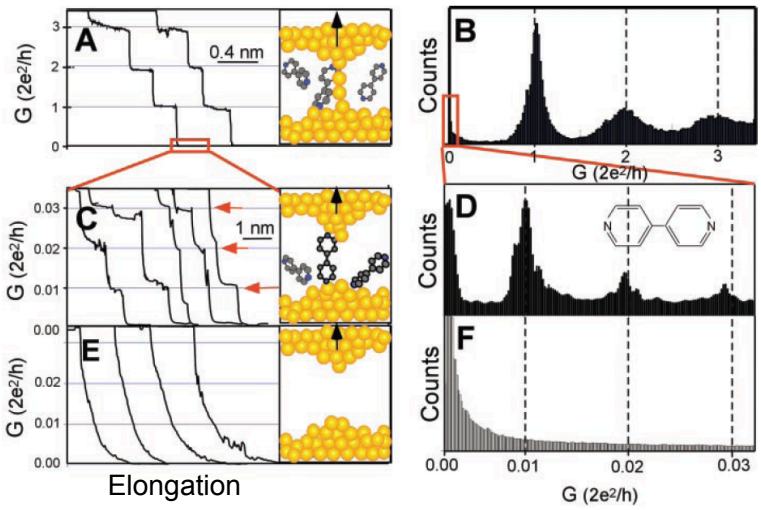

Figure 2.3. Conductance traces (left) from STM-BJ experiments performed by Xu *et al*.,[113] with (A) large conductance plateaus corresponding to atomic-scale, metallic junctions, (C) small conductance plateaus corresponding to molecular junctions, and (E) no plateaus in control experiments where no molecules were present. (B), (D), and (F) show the corresponding conductance histograms for a large number of curves obtained like those in (A), (C), and (E), respectively.

surface. This statistical approach applied by Xu *et al*.[113] reveals not only the presence of parallel molecular bridges, but also the inherent variability in single-molecule conductance. This variance is often attributed to mechanical- and/or thermal-induced structural differences between junctions. Specifically, previous studies have demonstrated the sensitivity of conductance to bonding site,[114] tip geometry,[51] BDT orientation,[50] and the presence of additional molecules in the local environment surrounding the bridged molecule.[35]

While single-molecule, proof-of-concept ME devices have shown considerable promise for real-world applications, many experimental features remain poorly understood. For example, in recent experiments performed by Tsutsui and co-workers,[16] the authors observed surprisingly low levels of Au-BDT-Au stability at 77 K compared to 298 K, which they attributed to "pre-straining" effects induced through the presence of parallel junctions prior to the formation of a single-molecule junctions. In other cases, inconsistencies in the measured conductance through the same molecule using different methods were observed.[51,56] Additional experiments reported a lack of reproducibility in conductance for molecular junctions formed repeatedly.[10,25] Explaining unexpected behavior in ME experiments is difficult due to the extremely short length and time scales impacting device behavior. Alternate experimental methods such as force measurements[46,47] and inelastic electron tunneling spectroscopy (IETS)[4,17,22,43] are sometimes used to provide additional clues about structure and dynamics. However, the most direct approach is to calculate the conductance from atomistically resolved models that closely mimic the experimental system.[8,30,31,35,41,52] In this way, the atomic-level structure can be directly correlated with the conductance behavior.

Table 2.1. Comparison of the computed zero-bias conductance values for BDT using various theoretical approaches. The most-probable experimental value published by two independent research groups is also included for comparison. Abbreviations are introduced for the tight-binding linear muffin-tin orbital in the atomic sphere approximation (TB-LMTO-ASA) method, the source and sink method (SSM), and approximate self-interaction corrected DFT (ASIC-DFT).

Method	Conductance (μS)
DFT-Jellium[57]	3
TransSIESTA[115]	35
DFT + Bulk States[116]	7
TB-LMTO-ASA[117]	5.5
SSM[118]	1.55
ASIC-DFT[86,87]	4.6
Hartree Fock[119]	44.2
GW Calculations[119]	64.3
Experiment[16,23]	0.85

Modeling and simulations of molecular junctions intensified shortly after the pioneering work of Reed and co-workers.[6] Di Ventra *et al.*[57] used quantum mechanical methods to calculate the I-V characteristics of BDT sandwiched between two jellium (*i.e.*, ideal) electrodes. While the resulting I-V curve reproduced the shape of the experimental I-V curve measured by Reed and co-workers,[6] the exact values differed by over two orders of magnitude. Additional sets of calculations by Emberly *et al.*[59] suggested that the Reed *et al.*[6] experiments had actually measured the I-V curve for two overlapping BDT molecules bonded to one tip each, instead of the assumed single BDT molecule bridging two tips. This explanation was supported by subsequent BDT experiments[16,23] showing much higher conductance values than those reported by Reed and co-workers.[6] Since these initial studies, better conformity has been obtained between the experimentally measured and theoretically calculated values of conductance for various molecules.[56] The exception to this is BDT, where experiment and theory generally differ by over an order of magnitude,[56] depending on the details of the calculations. Table 2.1 lists the calculated values for the zero-bias conductance of BDT sandwiched between Au(111) surfaces using various methods. It is important to note that the geometry input to each calculation varies slightly depending on the assumed geometry and whether the geometry was optimized. Table 2.1 demonstrates the wide variance in the calculated zero-bias conductance between different methods, and complicates the task of comparing to experimental measurements.

Additionally, it is unlikely that the assumed geometry in the theoretical calculations is representative of the experimental junction structure. Thiolate-terminated molecules such as BDT are known to cause extensive deformation to metallic contacts.[26,47] In fact, the S-Au bond is strong enough to pull out small monatomic

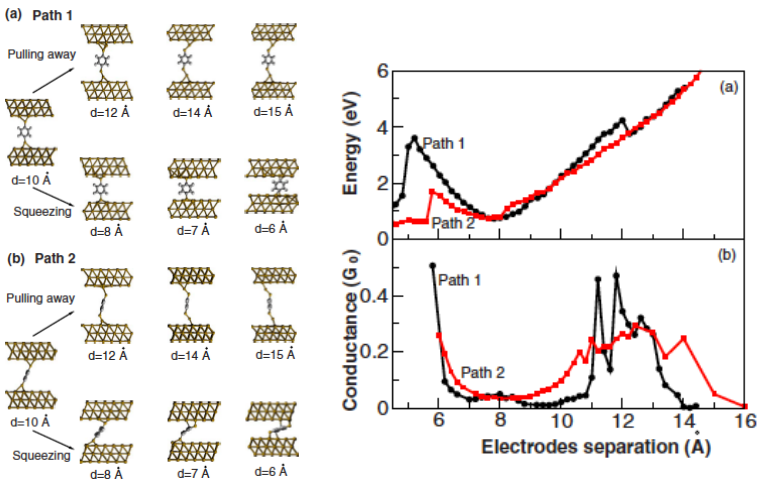

Figure 2.4. Results from work of Sergueev *et al.*[66] showing (left) two independent Au-BDT-Au junctions under elongation and (right) the energy and conductance of the junctions as a function of electrode separation.

chains (MACs) of Au atoms from step edges[120] and tips.[64] The impact of this deformation may drastically alter the computed conductance relative to that of a structurally ideal junction. As an important first step for resolving these differences, recent theoretical investigations[64–67] performed conductance calculations on geometries resulting from molecular junction elongation simulations. Sergueev *et al.*[66] performed elongation simulations of a single BDT molecule sandwiched between two Au(111) surfaces. Using DFT geometry optimizations to simulate elongation/compression and the source and sink method (SSM)[118] to compute conductance, the evolution of the zero-bias conductance was calculated for an initially upright and tilted BDT molecule, as shown in Figure 2.4. At large values of elongation, the junctions increased in conductance due to mechanically induced resonant tunneling. This result was subsequently reported in experiment,[43] thus illustrating the utility of a simulated break-junction theoretical approach for not only providing interpretations to experimental results but also discovering novel transport mechanisms.

In addition to including elongation effects into conductance calculations, thermal effects have also been considered by several groups.[68–71] These studies have demonstrated the high sensitivity of the computed conductance to relatively small changes in the geometry of the junction. For example, Andrews *et al.*[68] performed classical MD simulations of BDT thermally evolved between Au(111) surfaces, then computed the resulting conductance histogram by periodically extracting snapshots from the simulation for input into Hückel-based electron transport calculations. The histograms computed by Andrews *et al.*[68] and by other authors[69–71] reproduced the shape of curves observed in experiment, suggesting that in experiment the distribution in conductance is indeed caused by an ensemble of junction structures.

While theoretical methods for computing the conductance through molecular junctions have improved

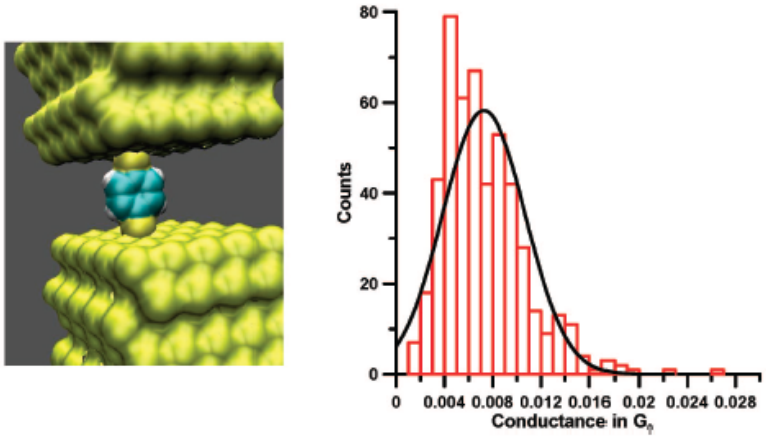

Figure 2.5. Results from work of Andrews *et al*.[68] showing (left) the simulated junction consisting of a single BDT molecule thermally evolving between two Au(111) surfaces and (right) the resulting computed conductance histogram.

recently, many of the approximations adopted in the calculations ultimately make it difficult to connect the results to experiment. For example, in Figures 2.4 and 2.5 the electrodes are modeled as perfectly flat surfaces and the effect of a surrounding monolayer is neglected. In experiment, the electrodes are likely to be disordered, deformed, or contain nanoscale defects such as steps or vacancies,[26,47] while the bridged molecule is likely to interact with nearby adsorbed molecules or solvent.[35] In order to make more meaningful connections to experiment, methods capable of incorporating these environmental factors are needed.

2.3 Gold Nanowires

Au NWs play an important role in MCBJ and STM-BJ molecular conductance experiments, where their elongation and failure immediately proceed, and therefore influence, the formation of a molecular junction. Understanding and controlling the structure and behavior of metallic junctions would ensure a stable, consistent platform for forming molecular junctions and measuring their properties. Numerous experimental studies[112,121–124] of Au NWs undergoing elongation have been performed to elucidate their novel structures and properties. These studies primarily employed a MCBJ or STB-BJ apparatus for measuring conductance and/or force during elongation. The structure of the neck can be inferred based on these data, *e.g.*, in single-atom constrictions the number of electron transport channels is limited to one, and thus a conductance value equal to the conductance quantum results.[122,123] Other structures such as monatomic chains (MACs),[125–127] helices,[125,127–129] and polytetrahedra[130] can appear in the constriction, some of which have been observed by high-resolution tunneling electron microscopy (HR-TEM).[125,127–129] Determining the variables that influence the formation of such structures has been a focus of many experimental and theoretical studies.[78,127,130] One important variable that has been largely ignored is the impact of solvent or an adsorbed species on the

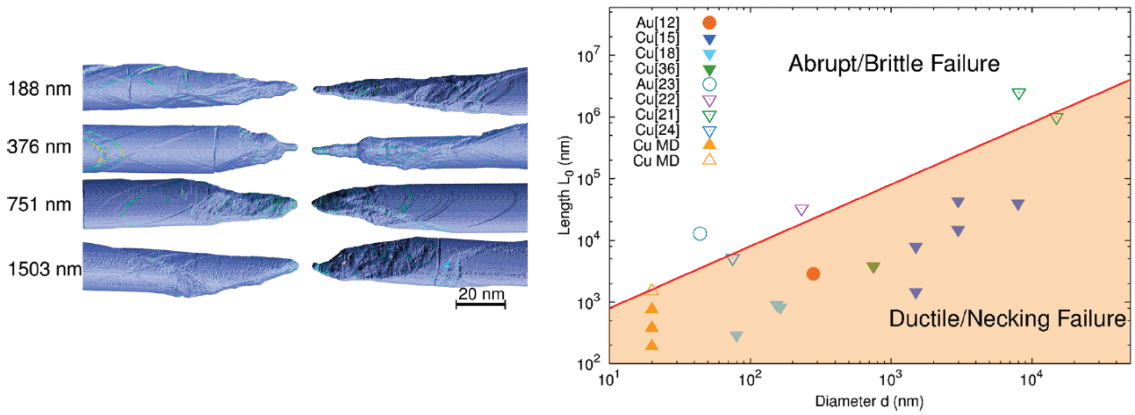

Figure 2.6. Results from work of Wu *et al.*[88] showing (left) failure structures of Cu NWs of various lengths and (right) a comparison of the observed failure behavior vs. the predicted failure behavior of metallic NWs. The filled and unfilled symbols correspond to ductile and brittle failure, respectively.

formation and stability of characteristic structures. The influence of molecular adsorption is likely to play an important role in NW elongation, and may provide a method for tuning the structures emerging during elongation.

Beyond their importance in molecular conductance experiments, Au NWs exhibit outstanding mechanical properties in excess of bulk Au.[131] Numerous experimental studies[131–134] have been performed to investigate the failure process and mechanism of Au (and other FCC metals) NWs. One recent simulation study performed by Wu *et al.*[88] reported a ductile-to-brittle transition for metallic NWs with increases in NW length. Figure 2.6 shows breaking structures of NWs with different lengths. As the NW length is increased, the NWs become noticeably less ductile, with little evidence of necking or plasticity at large lengths. Wu *et al.*[88] proposed a simple model for explaining the observed transition in failure behavior, and their model results agreed well with their simulations and prior experimental and theoretical work. Although this is an important result, a limited number of independent trajectories were analyzed for assessing the proposed transition, and the effects of temperature and ultra-small diameter were not considered. As stochastic thermal motion can significantly alter the structural pathway of elongating metallic NWs,[72,78,130] and sub-3-nm-diameter NWs have been fabricated in experiment,[128,135] the inclusion of these variables would help to clarify the validity and scope of the ductile-to-brittle transition.

CHAPTER III

SIMULATION AND COMPUTATIONAL METHODS

3.1 Interaction Models

3.1.1 Au-Au Metallic Bonding Potential

The second-moment approximation to the tight-binding potential (TB-SMA)[89] is applied throughout all chapters of this dissertation to describe Au-Au interactions. Simple pairwise potentials such as the 12-6 Lennard-Jones potential fail to properly describe many of the properties (*e.g.*, vacancy formation energies, surface structure, and relaxation properties) of transition metals.[89] Semi-empirical potentials, whose functional forms are derived from electronic structure considerations and then fit to experimental data, are better suited for simulations of transition metals. For instance, TB-SMA contains a many-body term that is modeled after the square-root dependence of the band energy on the second moment electron density of state:

$$E_B^i = -\left\{\sum_j \xi^2 e^{-2q(r_{ij}/r_0-1)}\right\}^{1/2}, \tag{3.1}$$

where E_B^i is the many-body energy of atom i. TB-SMA also contains a pairwise repulsive term given by

$$E_R^i = \sum_j A e^{-p(r_{ij}/r_0-1)}. \tag{3.2}$$

The total TB-SMA energy is then

$$E_C = \sum_i (E_B^i + E_R^i). \tag{3.3}$$

Values for the parameters A, ξ, p, q, and r_0 for Au are shown in Table 3.1, and are obtained from fits to the Au experimental cohesive energy, lattice parameter, and elastic constant.[89] An energy cutoff, r_{cut}, of 5.8 Å, is applied such that any pair of Au atoms separated by a distance greater than r_{cut} do not interact. Differentiating equation 3.1 yields an expression for force that depends on the electron density, ρ, of atoms i and j, where

Table 3.1. TB-SMA parameters for Au. Energy is reported in units of eV and kcal/mol, as eV is commonly used for metals while kcal/mol is used throughout this dissertation.

A (eV)	A (kcal/mol)	ξ (eV)	ξ (kcal/mol)	p	q	r_0 (Å)
0.2061	4.753	1.790	41.28	10.229	4.036	4.079

$\rho_i = \sum_j e^{-2q(r_{ij}/r_0-1)}$. Thus, the total force acting on each atom is calculated in two stages, with each stage looping over atom i's neighbors. This amounts to an additional computational cost compared to pairwise interaction models, where only a single loop over atom i's neighbors is performed.

Previous work in the Cummings group[77] showed that TB-SMA provided a closer match to quantum mechanical calculations of elongating Au NWs in comparison to other commonly used semi-empirical potentials (embedded-atom method[136] and glue model[137]). TB-SMA agreed closely with DFT calculations of the evolving energy and structure of a small Au NW under elongation, while the embedded-atom method and glue model failed to properly capture low-coordination effects on the NW surface and in the NW neck.

3.1.2 Propane Adsorbate Potentials

The adsorbate potentials described here are applied in Chapter IV, where the impact of an adsorbed monolayer on the behavior of elongating Au NWs is considered.

Au surfaces are known to interact strongly with several functional groups (*e.g.*, thiols, amines, and carboxylic acids).[138] Thiols (*i.e.*, -SH functional groups) in particular are widely used in nanoscale applications due to their ability to form strong linkages with metallic surfaces.[62] Beyond thiols, various other functional groups (*e.g.*, sp^2 carbon and sp^2 nitrogen)[139,140] exhibit strong physical interactions and weak chemical interactions with Au surfaces. For example, Schneebeli *et al.*[34] recently performed single-molecule conductance measurements on "anchor-less" molecules by taking advantage of the strong interactions between strained benzene rings and Au tips.

Here, the selection of adsorbates is limited to those that physisorb to Au surfaces. Explicit modeling of a chemisorbed species requires a more sophisticated simulation methodology[82] (see subsection 3.1.3) in order to accommodate the interface between the metallic surface and reactive headgroup. A recent study based on post-Hartree-Fock calculations found that the dominant interaction between a Au(111) surface and a physical adsorbate was dispersion.[141] This interaction is modeled using the 12-6 Lennard-Jones (LJ) potential:

$$U_{LJ} = 4\varepsilon_{ij}\left[\left(\frac{\sigma_{ij}}{r}\right)^{12} - \left(\frac{\sigma_{ij}}{r}\right)^{6}\right], \tag{3.4}$$

where r is the interatomic distance, ε_{ij} is the potential well depth, and σ_{ij} is the interatomic distance at which the energy between atoms i and j is zero. The Au atoms are treated as uncharged particles and the effects of Au polarizability, which should be minimal in the presence of a non-polar adsorbate, are neglected.

Two models are employed to simulate an adsorbate species. The first model is a LJ sphere model, in which the adsorbate is represented as a single, uncharged sphere (see Figure 3.1a). The naming convention LJ/Prop-X is used for the LJ sphere model, where X is the ratio of the adsorbate-Au LJ well depth, $\varepsilon_{Ads.-Au}$, to the

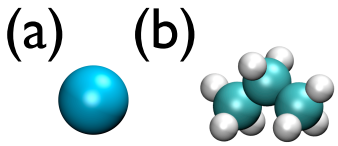

Figure 3.1. Adsorbate models: (a) Lennard-Jones propane (LJ/Prop-X), (b) all-atom propane (AA/Prop-Y). Images are drawn to scale. Many of the images in this work, including this one, were rendered in Visual Molecular Dynamics.[143]

Table 3.2. Adsorbate-adsorbent well depth energies.

System	$\varepsilon_{Ads.-Ads.}$ (kcal/mol)	$\varepsilon_{Ads.-Au}$ (kcal/mol)	$\frac{\varepsilon_{Ads.-Au}}{\varepsilon_{Ads.-Ads.}}$
LJ/Prop-0.5	0.553	0.277	0.50
LJ/Prop-1.0	0.553	0.553	1.00
LJ/Prop-2.0	0.553	1.106	2.00
LJ/Prop-3.0	0.553	1.659	3.00
LJ/Prop-4.0	0.553	2.212	4.00
AA/Prop-UFF	1.686	0.286	0.17
AA/Prop-MP2	1.686	0.447	0.27
AA/Prop-FCC	1.686	2.898	1.72

adsorbate-adsorbate well depth, $\varepsilon_{Ads.-Ads.}$. Thus, LJ/Prop-2.0 refers to a system in which $\varepsilon_{Ads.-Au}$ exceeds $\varepsilon_{Ads.-Ads.}$ by a factor of two. In accordance with previous work by Pu *et. al.*,[81] the adsorbate-adsorbate LJ parameters (σ = 4.66 Å, ε = 0.553 kcal/mol) are fit to the critical parameters of propane. The adsorbate-adsorbate parameters are held constant for all LJ/Prop-X simulations. Propane is chosen because of its simple structure and because it exists as a liquid at room temperature and sufficiently high pressures. While the LJ parameters of the LJ/Prop-X model are chosen to reproduce the properties of liquid propane, by adjusting $\varepsilon_{Ads.-Au}$, as reported in this work, a more general case adsorbate is modeled. The values of $\varepsilon_{Ads.-Au}/\varepsilon_{Ads.-Ads.}$ used in Au NW elongation simulations are listed in Table 3.2 and represent realistic interaction strengths for species that exhibit strong physical interactions with Au surfaces (*e.g.*, sp^2 carbon and sp^2 nitrogen). The manual adjustment of $\varepsilon_{Ads.-Au}$ can also be viewed as analogous to inducing adsorption by altering the electrochemical potential of Au NWs in real experiments.[142] Systems in which $\varepsilon_{Ads.-Au}/\varepsilon_{Ads.-Ads.} < 1.0$ represent cases where the propane molecules prefer to interact with one another rather than the Au NW. Such molecules can be thought of as a generic solvent that collides with (instead of adsorbing to) the Au NW during the elongation process. This was the scenario studied previously in the Cummings group.[81]

Table 3.3. Propane force field parameters.

Lennard-Jones Parameters and Partial Charges

System	Atom	ε_i (kcal/mol)	σ_i (Å)	q_i
LJ/Prop-X	-	0.553	4.660	-
AA/Prop-Y [144]	C	0.066	3.500	-0.24
AA/Prop-Y [144]	H	0.030	2.500	0.06

Adsorbate-Au Lennard-Jones Parameters for AA/Prop-Y

System	ε_{Au-C} (kcal/mol)	σ_{Au-C} (Å)	ε_{Au-H} (kcal/mol)	σ_{Au-H} (Å)
AA/Prop-UFF [144,145]	0.05	3.20	0.03	2.71
AA/Prop-MP2 [141]	0.10	3.83	0.04	3.53
AA/Prop-FCC [144,146]	0.59	3.03	0.40	2.56

AA/Prop-Y Bond Stretch Parameters [144]

Type	r_{eq} (Å)	K_r ((kcal/mol)/Å^2)
C-C	1.529	268.0
C-H	1.090	340.0

AA/Prop-Y Bond Angle Bending Parameters [144]

Type	θ_{eq} (°)	K_θ ((kcal/mol)/rad^2)
C-C-C	112.7	58.35
C-C-H	110.7	37.50
H-C-H	107.8	33.00

AA/Prop-Y Torsional Parameters, in kcal/mol [144]

Type	V_1	V_2	V_3
C-C-C-H	0.000	0.000	0.366
H-C-C-H	0.000	0.000	0.318

Next, a more detailed adsorbate model is studied: all-atom propane (see Figure 3.1b). The naming convention AA/Prop-Y is used for the all-atom model, where Y represents the study in literature from which the C-Au and H-Au LJ parameters are taken. The AA/Prop-UFF and AA/Prop-FCC parameters are obtained by mixing C and H parameters from the OPLS-AA force field with Au parameters from references[145,146] using geometric mixing rules. The AA/Prop-MP2 C-Au and H-Au parameters were calculated explicitly in reference[141] using Moller-Plesset second-order perturbation theory (MP2). The use of these three separate sets of parameters allow varying levels of interaction strength between propane and gold to be simulated (see Table 3.3). To estimate the adsorbate-Au well depth, $\varepsilon_{Ads.-Au}$, of the all-atom models, the energy between an isolated adsorbate molecule and a single Au atom is computed at various fixed distances; the same procedure is followed for two adsorbate molecules to estimate $\varepsilon_{Ads.-Ads.}$. Results are listed in Table 3.2.

Besides the adsorbate-adsorbent interactions, all other interactions in the AA/Prop-Y simulations are held fixed. Partial charges, intermolecular parameters, and intramolecular parameters are taken from the OPLS-AA force field,[144] and are shown in Table 3.3. The C-H nonbonded cross-interactions are calculated by applying geometric mixing rules to the OPLS-AA LJ parameters. The OPLS-AA force field contains terms for nonbonded and bonded interactions, with the sum of these interactions providing the total energy:

$$U_{Tot} = U_{LJ} + U_{Coul} + U_{Electro} + U_{Bond} + U_{Angle} + U_{Torsion}, \tag{3.5}$$

where U_{Bond}, U_{Angle}, and $U_{Torsion}$ are the bond stretching, angle bending, and torsion energy, respectively. The nonbonded interactions are described using the LJ potential (equation 3.4), and the short- and long-range electrostatic interactions. The long-range electrostatic interactions, $U_{Electro}$, are computed with the particle-particle particle-mesh solver (precision of 1.0 x 10^{-5}), while the short-range electrostatic interactions are calculated with the Coulombic potential:

$$U_{Coul} = \frac{q_i q_j e^2}{r}, \tag{3.6}$$

where q_i and q_j are the partial charges of atom i and atom j and e is the charge of an electron. Note that a scaling factor of 0.5 is applied to equation 3.4 and equation 3.6 for atoms separated by exactly three bonds. The bond stretching energy is given by:

$$U_{Bond} = K_r (r - r_{eq})^2, \tag{3.7}$$

where K_r is the harmonic force constant and r_{eq} is the equilibrium bond distance. The angle bend energy takes on a similar form:

$$U_{Angle} = K_\theta \left(\theta - \theta_{eq}\right)^2, \tag{3.8}$$

where K_θ is the harmonic force constant, θ is the bond angle, and θ_{eq} is the equilibrium bond angle. Finally, the torsion energy is calculated using:

$$U_{Torsion} = \frac{V_1}{2}\left[1 + cos\phi\right] + \frac{V_2}{2}\left[1 + cos2\phi\right] + \frac{V_3}{2}\left[1 + cos3\phi\right], \tag{3.9}$$

where V_1, V_2, and V_3 are the Fourier series coefficients and ϕ is the dihedral angle.

3.1.3 S-Au Chemical Bonding Potentials

The potentials described here are applied in Chapters V and VI for simulations involving Au and BDT. Modeling the S-Au bonding geometry is a non-trivial task, as Au adatoms and surface vacancies are often present, and S atoms may bond to multiple energetically competitive Au sites (*e.g.*, on-top, on-bridge; see Figure 3.2).[114,147,148] An extra level of complexity is added in the case of self-assembled monolayers (SAMs), as the number of interaction sites can become large, limiting the level of accuracy available for describing the S-Au interaction. One of the more complete approaches for modeling SAMs is a hybrid molecular mechanical and quantum mechanical (MM/QM) scheme, where the S-Au interaction is treated within an *ab initio* framework while the interacting monolayer tails are treated within a computationally cheaper classical framework.[149] Despite this approach's advantage in accuracy, the system sizes accessible for study are still limited, and obtaining ergodic sampling in MM/QM simulations is difficult. An alternative is to parameterize a classical potential using *ab initio* methods and then to implement this potential within atomistic and/or molecular simulations. This approach permits much larger length scales and longer time scales to be sampled, resulting in more meaningful statistics in comparison to *ab initio* techniques.

Previous work[80] in the Cummings group utilized DFT calculations to calibrate a Morse potential for

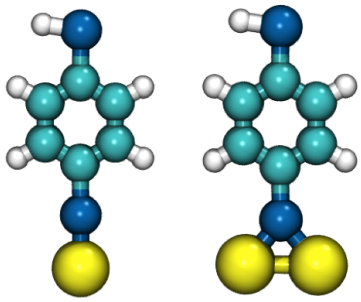

Figure 3.2. On-top (left) and on-bridge (right) configurations used for modeling of the S-Au chemical bond.

Table 3.4. The Morse potential parameters for describing S-Au chemical bonding. Each set of parameters represents the average of applying three separate DFT functionals. Note, the D_e value listed for the on-bridge site applies for a single S-Au pair. The total on-bridge energy is calculated as the sum of the two S-Au pairs.

Site	D_e (kcal mol^{-1})	r_e (Å)	α (Å^{-1})
On-Bridge	28.7	2.44	1.67
On-Top	49.4	2.29	1.72

describing BDT bonding on different gold clusters. The Morse potential, in this case, comes in the form:

$$U_{Morse}(r) = D_e e^{-\alpha(r-r_e)}\left[e^{-\alpha(r-r_e)} - 2\right], \tag{3.10}$$

where r is the S-Au bond length and D_e, α, and r_e are adjustable parameters selected to reproduce the bonding character of different S-Au motifs. Two of the Au clusters considered by Leng and co-workers represent cases where the BDT is bonded at an on-top site and an on-bridge site (see Figure 3.2). Previous experimental[28,150] and theoretical[62,80,147,149] studies have demonstrated that the on-bridge site is the energetically favored bonding site for benzenethiolate[62,80,150] and alkanethiolates,[28,147,149] while on-top sites are important in low-coordination environments.[28]

3.1.4 BDT Intermolecular and Intramolecular Potentials

The potentials described here are applied in Chapters V and VI, where simulations involving BDT are performed. Parameters for describing the inter- and intramolecular interactions for BDT are taken from the Universal Force Field (UFF),[145] and are shown in Table 3.5. Cross-interaction LJ parameters for different atomic species are calculated from Lorentz-Berthelot combining rules (*i.e.*, ε_{ij} is calculated as a geometric mean while σ_{ij} is calculated as an algebraic mean). Angle bending and torsion parameters for interactions involving Au atoms are derived from prior work in the Cummings group,[79] and are also listed in Table 3.5. The total energy is given by equation 3.5, with the addition of the S-Au Morse potential energy calculated from equation 3.10 and an intramolecular inversion term, which is introduced below.

The functional forms for several of the terms in equation 3.5 differ between the OPLS-AA and UFF force fields. Within UFF, the LJ, bond stretch, angle bending, and torsion energy terms are given by:

$$U_{LJ,UFF} = D_{ij}\left[\left(\frac{\sigma_{ij}}{r}\right)^{12} - 2\left(\frac{\sigma_{ij}}{r}\right)^{6}\right], \tag{3.11}$$

$$U_{Bond,UFF} = \frac{1}{2}k_{ij}\left(r - r_{eq}\right)^2, \tag{3.12}$$

Table 3.5. BDT force field parameters. The values listed for the on-bridge site are for a single S-Au pair.

Lennard-Jones Parameters

Atom	D_{ij} (kcal/mol)	σ (Å)
C	0.105	3.851
H	0.044	2.886
S	0.274	4.035
Au	0.039	3.293

Bond Stretch Parameters

Type	r_{eq} ((kcal/mol)/Å^2)	k_{ij} (Å)
C-C	925.83	1.379
C-H	708.61	1.085
C-S	588.45	1.800
S-H	438.30	1.429

Bond Angle Bending Parameters

Type	K_θ ((kcal/mol)/rad^2)	θ_{eq} (°)
C-C-C	222.72	120
C-C-H	114.23	120
C-C-S	201.01	120
C-S-H	102.16	92.1
C-S-Au (on-top)	145.50	105.4
C-S-Au (on-bridge)	71.52	110.8

Torsion Parameters

Type	$1/2V_\phi$ (kcal/mol)	ϕ_{eq} (°)
X-C-C-X	13.474	180
C-C-S-H	3.9528	90
C-C-S-Au (on-top)	2.920	90
C-C-S-Au (on-bridge)	1.229	90

Inversion Parameters

Type	k_{ijkl} (kcal/mol)	ω_{eq} (°)
Central carbon atom	6	0

Table 3.6. Partial charge assignment for BDT, in bulk (*i.e.*, benzene-1,4-dithiol) and bonded to Au.

Atom	Bulk BDT	S7 bonded to Au	S8 bonded to Au	S7 and S8 bonded to Au
C1	-0.49	-0.33	-0.49	-0.34
C2	-0.06	-0.10	-0.06	-0.06
C3	-0.06	-0.06	-0.10	-0.06
C4	-0.49	-0.49	-0.33	-0.34
C5	-0.06	-0.06	-0.10	-0.06
C6	-0.06	-0.10	-0.06	-0.06
S7	0.06	0.13	0.06	0.06
S8	0.06	0.06	0.13	0.06
H9	0.20	0.20	0.20	0.20
H10	0.20	0.20	0.20	0.20
H11	0.20	0.20	0.20	0.20
H12	0.20	0.20	0.20	0.20
H13	0.20	n/a	0.15	n/a
H14	0.20	0.15	n/a	n/a

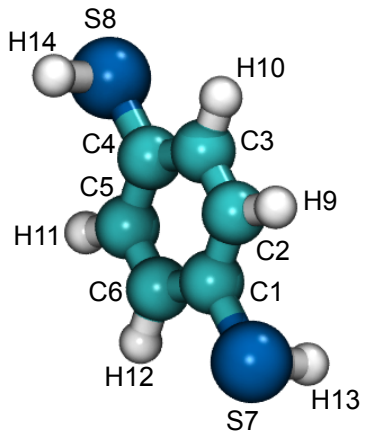

Figure 3.3. Atom labels for assignment of BDT partial charges in Table 3.6.

$$U_{Angle,UFF} = \frac{k_{ijk}}{2sin^2\theta_0}\left(cos\theta - cos\theta_{eq}\right)^2, \tag{3.13}$$

$$U_{Torsion} = \frac{1}{2}V_\phi\left[1 - cos(n\phi_{eq})cos(n\phi)\right], \tag{3.14}$$

respectively. In equations 3.11-3.14 the force constants are defined as D_{ij}, k_{ij}, k_{ijk}, and V_ϕ. Note that n=2 for all torsion angles considered in this work. UFF incorporates an inversion term, which for BDT serves to

enforce the rigidity of the benzene ring. The inversion energy is given by:

$$U_{Inversion} = k_{ijkl}\left(1 - cos\omega_{ijkl}\right), \tag{3.15}$$

where k_{ijkl} is the force constant and ω_{ijkl} is the angle between the il axis and the ijk plane (where atom i is bonded to atoms j, k, and l). For BDT, equation 3.15 is applied for all six carbon atoms.

When a S-Au chemical bond forms, there is redistribution of the partial charges within BDT.[79] This charge transfer does not lead to significant geometric changes within BDT, however it can impact monolayer packing through short- and long-ranged electrostatic interactions. DFT calculations performed previously in Cummings group[79] determined the partial charges residing on the atoms from Mulliken population analysis[151] for BDT bonded to Au. The average of three different functionals are applied here and are shown in Table 3.6. No charge is assigned to Au atoms, while the bulk BDT (*i.e.*, benzene-1,4-ditthiol) partial charges are taken from UFF.[145] The short-range electrostatic interactions are computed with U_{Coul} (equation 3.6) while the long-range corrections are computed using an Ewald summation or the particle-particle particle-mesh solver (precision of 1.0 x 10^{-5}).

3.2 Simulation Protocols

3.2.1 Stretch-and-Relax Molecular Dynamics Nanowire Elongation Procedure

This simulation technique is applied throughout all chapters of this dissertation. NW elongation is simulated by applying a stretch-and-relax simulation protocol[77,78,81,82] in the Large-scale Atomic/Molecular Massively Parallel Simulator (LAMMPS)[153] package. Two rigid layers of "gripping" atoms (colored in green and red in Figure 3.4) are placed on both ends of a [100]-oriented, cylindrical NW. The gripping atoms on the right side of the NW are displaced by 0.1 Å in the [100] direction between periods of MD in the canonical ensemble (constant NVT, where N is the number of atoms, V is volume, and T is temperature). In Chapter VII, the NW is pulled from both sides, with the gripping atoms on the left and right sides of the wire periodically displaced by 0.05 Å in the [$\bar{1}$00] and [100] directions, respectively. The effective elongation rate is controlled by adjusting the simulation time between displacements of the gripping atoms. Typical rates range

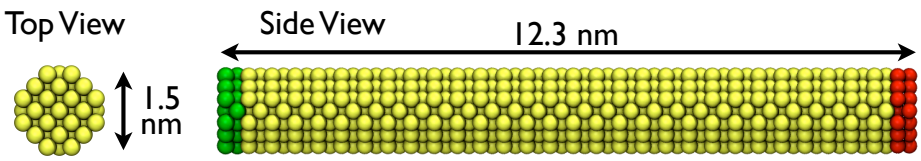

Figure 3.4. Example of an initial NW geometry. The gripping atoms are colored in green and red, while dynamic atoms are colored yellow. This figure is reproduced from previous work.[152]

from 0.1-2.0 m/s; subtle differences in the structural pathway during elongation have been observed in this range, however the resulting spectrum of ruptured tip geometries does not vary significantly.[152]

The temperature is controlled with the Nosé-Hoover thermostat[154,155] and the equations of motion are integrated using the velocity Verlet algorithm with a time step of 2.0 fs. Periodic boundary conditions are applied in all three directions; in some cases the box length in the direction of stretching is increased to coincide with the increasing NW length, while in others the box size is fixed during the simulation at a size that is sufficiently large to ensure that the NW does not interact with itself during elongation and rupture. Prior to elongation, each independent elongation simulation is initialized with a random Gaussian distribution of atomic velocities resulting in a temperature of 0.01 K. The NW is then allowed to relax its structure at 0.01 K for 100-200 ps. An additional 100-200 ps of MD are next performed while ramping the temperature up to its target value.

3.2.2 Semigrand Canonical Monte Carlo Sampling

This method is applied for the Au/BDT simulations presented in Chapters V and VI. The spontaneous formation of a molecular junction at fixed interelectrode distance occurs on time scales of $\sim$0.1 s in experiment;[50] this includes time required for bond formation and for the molecule to explore sufficient phase space for bridging. These time scales are inaccessible with MD simulations, where time steps for integrating the equations of motion are typically on the order of 10^{-15} s. To overcome the slow kinetics of chemisorption, Metropolis-type[156] Monte Carlo (MC) simulations, where configurational space is sampled in a random way, are often applied. Specifically, grand canonical Monte Carlo (GCMC) simulations can simulate an interface (in this case, a Au NW surface) in equilibrium with a bulk solution of molecules by setting the chemical potential of the molecules to a value appropriate for the bulk.[157] In addition to efficiency limitations, conventional MD simulations cannot handle the reactive nature of gold-thiol self-assembly. In contrast, the path to an equilibrium state is of no importance in MC, so unphysical move types such as molecule identity swaps can be performed to treat reactions.[158]

During MC sampling, on-top and on-bridge bonding of BDT to a NW surface is realized by performing the simulations within the semigrand canonical ensemble.[159] In previous work in the Cummings group,[81,82,157] MC sampling was performed in the grand canonical ensemble (constant μVT, where μ is chemical potential, V is volume, and T is temperature), with the Au NW surface in equilibrium with a bulk solution of BDT. Semigrand canonical Monte Carlo (SGCMC) simulations are akin to GCMC simulations in all respects except that in SGCMC simulations the composition of a mixture is sampled. Thus, in addition to the BDT center-of-mass (COM) displacement, COM rotation, insertion, and deletion moves of GCMC, the identity of a BDT may be swapped between those capable of bonding on-top and on-bridge. The identity of a newly

created BDT molecule is chosen at random, with equal probability of bonding at on-top or on-bridge sites. Bridge sites are taken to be those pairs of Au surface atoms separated by a distance of 2.51-3.25 Å. The main advantage of performing simulations in the semigrand canonical ensemble is that molecule swap moves ensure more efficient and complete sampling of the S-Au bonding geometry. The acceptance probability for a swap move is

$$p_{acc} = min[1, \frac{f_1}{f_2} e^{-\beta \Delta U}], \tag{3.16}$$

where $\beta = \frac{1}{kT}$ (k is Boltzmann's constant and T is temperature), ΔU is the change in energy due to the molecule identity swap, and f_i represents the fugacity of species i. Since the two BDT species are considered thermophysically equivalent, $f_1 = f_2$ and equation 3.16 reduces to a simple expression reminiscent of the acceptance criterion for a standard molecule COM displacement or rotation.

The SGCMC simulations are initialized with bulk BDT (*i.e.*, beznene-1,4-dithiol) placed on a lattice surrounding the Au NW. As a BDT moves (or is inserted) close to the Au NW, the probability of it chemisorbing onto the NW surface increases. To improve the efficiency of the MC simulations, the formation of a S-Au bond is modeled using a bonding cutoff, such that if a S atom moves within 3.66 Å of the appropriate bonding site (on-top or on-bridge, depending on the identity of the molecule), the S-H bond dissociates (with the H atom discarded from the simulation) and the S atom covalently bonds to the Au site. Recall that the MC method does not provide information about the dynamics of bond formation, but rather produces thermodynamically favored, equilibrium configurations. To ensure a smooth transition between S-Au bonded and unbonded states, the S-Au bond stretching term used in previous work[82] is slightly modified. The potential energy between a S and Au atom is described using

$$U_{S-Au}(r) = \begin{cases} -\int_r^{r_{cut}} \nabla U_{Morse}(r)\, dr - \int_{r_{cut}}^{\infty} \nabla U_{LJ,UFF}(r)\, dr & \text{for } r < r_{cut} \\ \\ U_{LJ,UFF}(r) & \text{for } r \geq r_{cut}, \end{cases} \tag{3.17}$$

where U_{Morse} and $U_{LJ,UFF}$ are defined in equations 3.10 and 3.11, respectively. For predicting S-Au bond formation and breakage, a value of r_{cut} = 3.66 Å is chosen. This value corresponds to the minimum on the S-Au LJ curve, ensuring a relatively smooth transition in both the energy and force between a S-Au pair at r_{cut}.

During MC sampling, constant-μVT moves are performed until the density of BDT in the simulation box remains relatively constant. This is followed by constant-NVT moves in which the packing of the BDT SAM is relaxed and additional BDT may attach to the surface. In the fixed-μVT simulations, a given move type

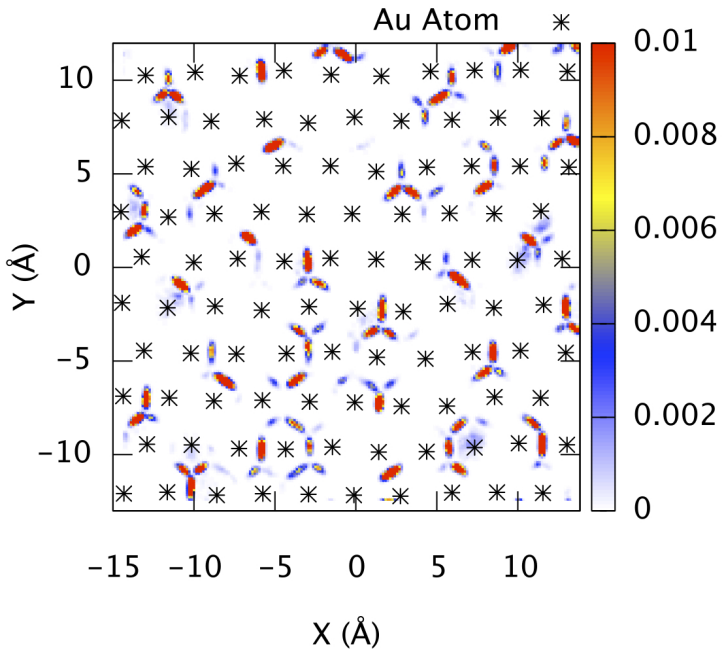

Figure 3.5. The distribution of the positions of BDT S atoms bonded to the Au(111) surface, for surface coverage 0.27. The color bar indicates the relative frequency of a particular $x-y$ position for each of the bonded S atoms. The black stars indicate the positions of the Au atoms on the first layer of the surface.

is selected with probabilities 0.45, 0.45, 0.04, 0.04, and 0.02 for BDT center-of-mass (COM) displacement, COM rotation, insertion, deletion, and identity swap, respectively. For fixed-NVT MC moves, move types are selected with probabilities 0.49, 0.49, and 0.02 for BDT COM displacement, COM rotation, and identity swap, respectively. In all cases the maximum BDT displacement and rotation is adjusted to obtain a 40% acceptance rate.

In accordance with the previous work of Pu *et al.*[81] the excess chemical potential, μ_{ex}, of both BDT species is set to -0.525 kcal/mol. Periodic boundary conditions are applied in all three directions, except in Chapter V where reflective walls are placed at the boundary of each BDT-coated Au tip during tip compression. Finally, for computational efficiency, the Au atoms are held fixed while the BDT molecules are modeled as rigid molecules from an optimized structure using UFF.[145]

To validate that SGCMC simulations enable BDT molecules to explore their preferred adsorption sites, constant-NVT moves for a BDT monolayer on the Au(111) surface are performed at a surface coverage 0.27. Here, surface coverage is defined as the number of chemisorbed BDT molecules divided by the number of Au atoms on the surface. After reaching equilibrium, 10 million MC moves are performed with configurations

saved every 5,000 steps. In Figure 3.5 the distribution of positions of BDT S atoms bonded to the relaxed Au(111) surface is shown. The Au(111) surface is a frequently used substrate for preparing self-assembled monolayers composed of thiol-terminated organic molecules.[62,147,149,150] Among the challenges of modeling the S-Au interface includes capturing the strong chemical bonding and mobility of S atoms around numerous possible bonding sites. Previous work has demonstrated that on-bridge and on-top sites are the relevant bonding sites for BDT and other thiol-terminated organic molecules,[62,80,147,149,150] with the on-bridge site being energetically favored.[62,80,147,149] The results in Figure 3.5 demonstrate that the SGCMC simulation protocol predicts S atom pathways predominantly along the energetically preferred on-bridge sites, with areas of red, orange, and yellow appearing between two Au atoms. Adsorption at on-top sites occurs to a limited degree, as evidenced by a few light blue areas directly above (or close to) a single Au atom. Thus, the SGCMC method predicts reasonable bonding geometries, in agreement with previous experimental and theoretical results.

3.2.3 Hybrid MD-MC Simulations

This simulation scheme is applied in Chapters V and VI to simulate the elongation and rupture of BDT-coated Au NWs. It is also used to mechanically and/or thermally evolve Au-BDT-Au junctions. In the hybrid MD-MC scheme, elongation of a Au NW is combined with chemisorption of BDT molecules onto the Au NW surface. During the MD simulations, all bonds are fixed. SGCMC sampling is then applied to sample the preferred bonding geometries, with the results passed back to the MD simulations. This approach accommodates the dynamic packing and bonding of the BDT SAM on the deforming Au NW surface.

SGCMC sampling is performed after some interval (between 0.1-1.0 Å) of MD stretching. The amount of SGCMC sampling is determined by the stretching interval. A large interval requires more SGCMC moves to fully sample the sites on a deformed NW surface. Tests are performed to ensure that the SGCMC sampling is sufficient. In all cases, applying more MC moves and/or applying MC moves at more frequent elongation intervals does not change the results significantly.

The entire procedure for simulating MCBJ experiments is outlined in Figure 3.6. The majority of the simulation time is spent within the loops on the left and right of the diagram, both of which rely on the hybrid MD-MC scheme. The left loop represents stretching of a BDT-coated NW until rupture, while the right loop involves the repeated formation and mechanical and/or thermal evolution of a Au-BDT-Au junction. The resulting ensemble of molecular junctions obtained from the MD-MC simulations are input to electronic structure calculations, which are described in the next section. Between the two loops in Figure 3.6 the bulk BDT (*i.e.*, benzene-1,4-dithiol) is discarded from the simulation box to model the evaporation of excess solvent that occurs in real experiments.

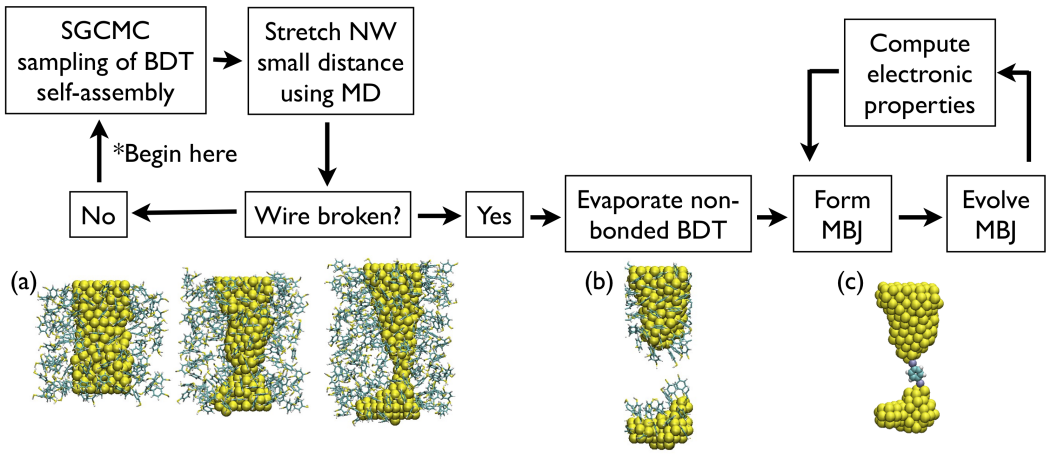

Figure 3.6. Flow diagram of procedure for MCBJ simulations. The images shown below depict the simulation process for a 256-atom Au rectangular slab, beginning with (a) the stretching of the slab in the three images to the left, followed by (b) the evaporation of the non-bonded BDT surrounding the ruptured Au tips, and finally (c) the formation of a Au-BDT-Au junction.

3.3 Quantum Mechanical Calculations

Classical mechanics do not apply for describing electron transport.[57] In order to calculate the conductance through a molecular junction, the relevant energy levels must be solved by quantum mechanical (QM) methods. Here, a description is provided of the QM techniques used to calculate electron transport through the simulated Au-BDT-Au junctions in Chapter VI.

3.3.1 Density Functional Theory Calculations

Density functional theory (DFT) is a QM method developed for efficiently solving the ground-state electronic structure of molecules and solids.[160,161] A DFT package called SIESTA[162,163] (Spanish Initiative for Electronic Simulations with Thousands of Atoms) is used in this dissertation to self-consistently solve the electronic structure of simulated Au-BDT-Au junctions. SIESTA is a numerical implementation of DFT designed to handle very large systems through highly parallel algorithms that scale well to a large number of processors. It employs a local-atomic-orbital (LAO) basis set and uses norm-conserving pseudopotentials for describing interactions between inner and outer shell electrons.

For the calculations performed in this dissertation, a double-ζ with polarization function (DZP) LAO basis set is used for all atoms, except for conductance histogram calculations (these require calculations for a large number of junctions), where a 6*s*-only single-ζ basis set is used for the lead atoms (the DZP basis is still used for the remaining atoms).[87] For the exchange and correlation functional, approximate self-interaction corrections (ASICs)[85] are applied to the local density approximation (LDA), which more accurately predicts

the energy level lineup between BDT and Au leads than standard DFT.[67,86,87] ASICs are used for all non-metal atoms, where self-interaction errors are most prominent. Note that whereas for isolated molecules applying the full ASIC usually gives good agreement with experimental values for ionization potentials (IPs), in general the IP decreases as the molecule is brought closer to a metallic electrode due to image charge formation in the metal.[164] To take into account this metal induced reduction of the IP, a scaling parameter equal to 0.5 is used for the amount of ASIC that is added.[85] A confining energy shift of 0.03 eV and a cutoff of 600 Ry for the grid integration are applied for all calculations. Since the system is periodic in all three directions, Bloch's theorem[165] is applied in which the wave functions are expressed in terms of reciprocal space vectors. The electron density is confirmed to converge with respect to the k-point sampling. In most cases, a 3 x 3 Monkhorst-Pack k-point sampling of the surface Brillouin zone suffices.

3.3.2 Conductance Calculations

Once the electron density is known, conductance can be calculated using the Landauer-Büttiker formalism[166] written in terms of Green's functions (GFs). The DFT+GF method is currently the most widely used approach for computing electron transport through molecules, due to its versatility and computational efficiency.[60,61,64–67,86,87,118,167–169] In this dissertation, the DFT+GF approach as implemented in the SMEAGOL package[170,171] is applied to calculate the zero-bias conductance. The zero-bias conductance is given by

$$G = T(\varepsilon_F)G_0, \tag{3.18}$$

where T is the transmission probability, ε_F is the electrode Fermi level, and $G_0=\frac{2e^2}{h}$ (e is the charge of an electron and h is Planck's constant) is the conductance quantum. The transmission is calculated and averaged across multiple k points. For each lead size, the convergence of the transmission with respect to the k-point sampling is carefully verified.

Figure 3.7 shows a typical Au-BDT-Au junction setup for a SMEAGOL calculation. The extended

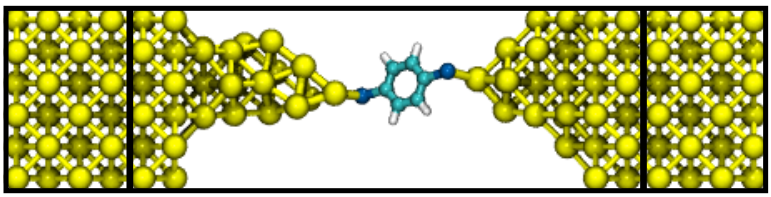

Figure 3.7. Schematic of the simulation cell used in a typical SMEAGOL calculation. The semi-infinite lead consists of four perfect layers of Au(100) and is attached to both sides of the extended molecule. Two additional perfect Au(100) layers are added to ensure sufficient charge screening.

molecule consists of twelve perfect layers of Au(100) atoms (six layers on each side), deformed Au tips, and a BDT molecule connected to both tips. Before computing the conductance, the electronic structure of the semi-infinite leads (four layers enclosed by the box on the left and right of the extended molecule) is computed. Since the left and right leads are the same, this calculation is only performed once.

3.3.3 Method Validation

3.3.3.1 Benchmark Calculations of Ideal Junctions

To assess the accuracy of the interaction potentials, the conductance of four benchmark systems is calculated for comparison to results in literature, with the geometry of each system first optimized by using the interaction potentials described in subsections 3.1.1, 3.1.3, and 3.1.4. Each system contains a single BDT molecule sandwiched between two Au electrodes. The electrodes tested are: (100) surfaces, (111) surfaces, (100) tips, and (111) tips, as shown in Figure 3.8. Each lead consists of six layers, with Au(100) and Au(111) containing eight and twelve atoms per layer, respectively. To ensure converged transmission for these small-lead configurations, 6 x 6 Monkhorst-Pack k-point sampling is applied (except for the (111) tips, where 12 x 12 is used). The geometry of each system is optimized by applying the following "quench" MD minimization protocol. After positioning each S atom at the on-bridge (for surfaces) or on-top (for tips) site of each electrode, the BDT geometry and electrode-electrode distance are relaxed by applying the Nosé-Hoover thermostat at 0.01 K and treating each electrode as a rigid body free to move in the axial direction; the BDT

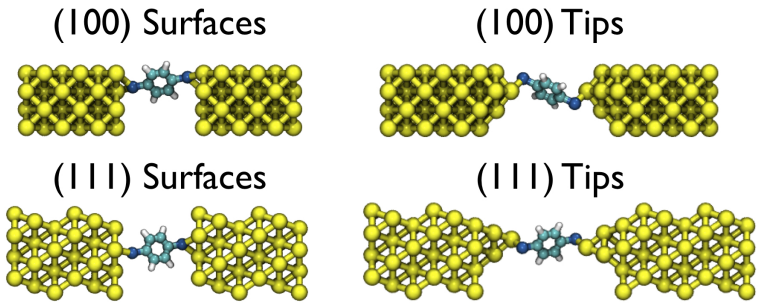

Figure 3.8. Benchmark geometries.

Table 3.7. Results for benchmark conductance calculations.

	(100) Surfaces	(111) Surfaces	(100) Tips	(111) Tips
$G\ (\frac{2e^2}{h})$	0.060	0.061	0.083	0.143
$\varepsilon_{HOMO} - \varepsilon_F$ (eV)	-1.708	-1.548	-1.427	-1.106
$T(\varepsilon_{HOMO})$	0.825	1.004	1.365	1.695

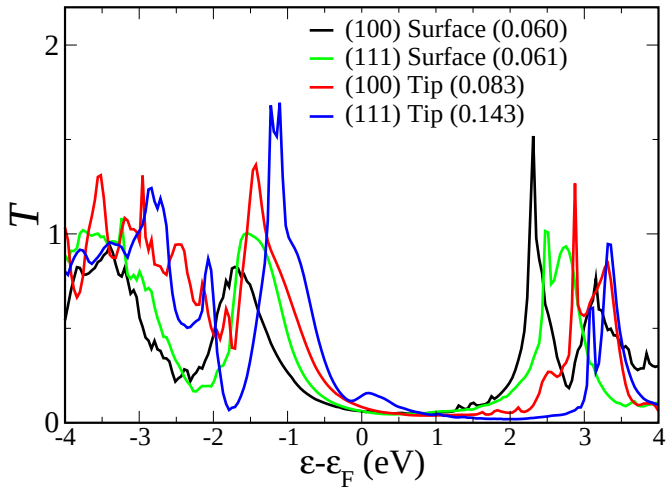

Figure 3.9. Transmission curves for the four benchmark geometries. The zero-bias conductance is listed in parentheses in the legend.

and Au atoms in the first two layers (and tips, if applicable) of each surface are then allowed to relax at 0.01 K.

Table 3.7 summarizes the results for the benchmark calculations. Figure 3.9 plots the transmission curves for each system. Excellent agreement is obtained between the zero-bias conductance ($0.061G_0$) with previous results ($0.06G_0$)[87] for BDT bonding at the on-bridge sites on two Au(111) surfaces. The metal-molecule coupling differs depending on the crystallographic orientation of the electrodes. Sen *et al.*[63] observed stronger coupling for alkanedithiolates connected to Au(100) surfaces than Au(111) surfaces. The metal-molecule coupling is also stronger for BDT connected to Au(100) surfaces, as evidenced by the lower energy and transmission at the highest occupied molecular orbital (HOMO) for Au(100) surfaces than Au(111) surfaces. The coupling strength decreases further for both tip geometries, as expected, with the (100) tip exhibiting stronger coupling than the (111) tip. Interestingly, the conductance increases for weaker metal-molecule coupling, in contrast to results for alkanedithiolates.[63] This difference occurs due to the proximity of BDT's HOMO to ε_F, as sufficient weakening of the metal-molecule coupling gives rise to near-resonant tunneling through the junction, thus increasing the conductance.

Thus, applying the Au and BDT interaction potentials in combination with SMEAGOL transport calculations producess conductance values that are consistent with results from literature for ideal, DFT-optimized junctions.

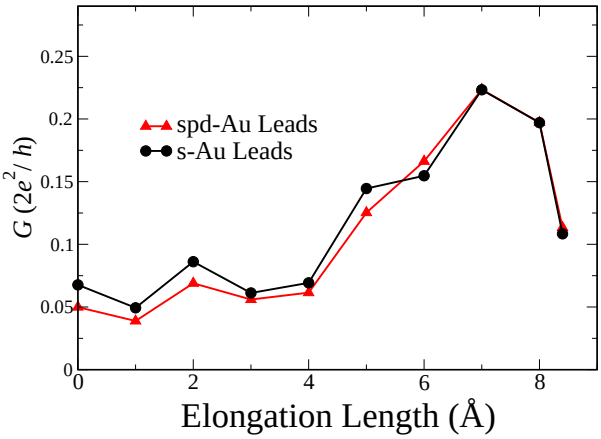

Figure 3.10. Comparison of the calculated conductance trace using the DZP 5*d*6*s*6*p* and SZ 6*s*-only basis set for the lead atoms.

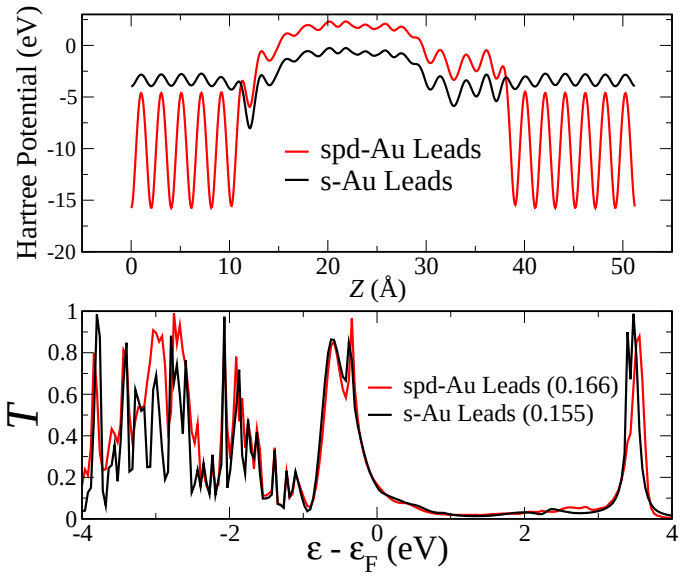

Figure 3.11. Detailed comparison for the reduced and full basis sets. Calculated Hartree potential (top) and transmission (bottom) using the DZP 5*d*6*s*6*p* and SZ 6*s*-only basis set for the lead atoms. The zero-bias conductance is shown in parentheses of the legend.

3.3.3.2 Reduced Basis Set for Conductance Histogram Calculations

To reduce the computational cost of the conductance histogram calculations, a 6*s*-only single-ζ basis set is applied for the lead atoms (the full basis set is still applied for all other atoms).[87] The zero-bias conductance and transmission resulting from application of a reduced basis set compare well with results obtained using the full basis set. Figure 3.10 compares the conductance for multiple geometries during elongation of a Au-BDT-Au junction. Figure 3.11 provides a detailed comparison for a single geometry at elongation length =

6 Å in Figure 3.10. While there is less charge present in the leads for the simplified basis set, the features in the transmission, especially around ε_F, are still adequately captured.

3.4 Analysis Methods

A number of methods are applied throughout this dissertation to analyze simulation results. Below is a description of the most important or commonly used methods.

3.4.1 Identification of Nanowire Surface Atoms

This analysis tool is applied in Chapter IV and V to quantify monolayer surface coverage (defined as the number of monolayer molecules divided by the number of Au surface atoms). Atoms located on the surface of a NW play an important role throughout this dissertation. In vacuum, surface atoms experience stress and high energies as a result of low coordination. In the presence of an adsorbing species, NW surface atoms interact directly with the adsorbate and provide sites for BDT bonding. Figure 3.12 illustrates the procedure used for identifying surface atoms. Probe particles are shot towards the NW surface from a variety of different angles and positions, with the code detecting the first atom that the probe particle collides with. A list of surface atoms is stored in memory so that no atom is counted more than once. The size of the probe particle is an important parameter in the algorithm; sizes that are too small may penetrate the NW surface

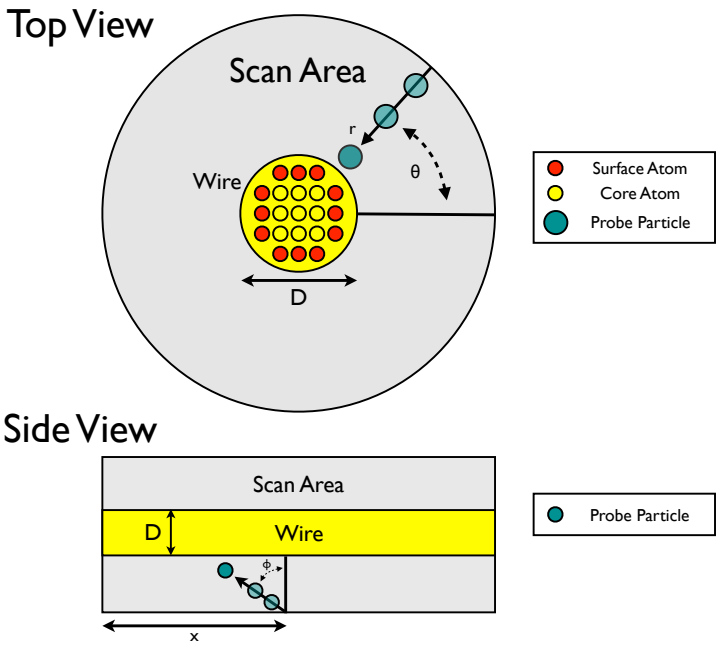

Figure 3.12. Schematic illustrating the surface atom identification procedure. Probe particles originating at various points (x,θ) on the surface of a cylinder are fired at the NW in various directions, ϕ.

while sizes that are too large may miss surface atoms in certain environments. A size equal to that of a Au atom (2.88 Å) is selected and yields results that are consistent with visual inspection.

3.4.2 Calculations of Monolayer Diffusion

In Chapter IV the mobility of an adsorbed monolayer on unstretched NWs is calculated using the Green-Kubo[158] velocity autocorrelation function:

$$D_i = \int_0^{t_f} \Big\langle v_i(t) v_i(0) \Big\rangle \, dt \tag{3.19}$$

where v_i and D_i are the velocity and average diffusion coefficient in the i direction, respectively, of an individual monolayer molecule. While a value approaching infinity for t_f is ideal for bulk diffusion calculations, a relatively small value of t_f is appropriate for calculating properties of a monolayer. A smaller value is appropriate because diffusion is a function of the local density around a Au NW and a molecule adsorbed to a Au NW at one instant time can desorb only a short time later. A value of t_f = 2 ps is selected and the 100 molecules that are on average closest to the Au NW during each successive 2 ps time span are used to compute the total average for D_i. Although the selection of a finite t_f value is not appropriate for bulk diffusion calculations, this method allows for the assessment of relative differences between the various adsorbate models in Chapter IV.

3.4.3 Residence Time Correlation Function

While calculating monolayer mobility around unstretched wires is straightforward, this is more difficult for elongating Au NWs since the surface is no longer static. In Chapter IV, the mobility of the adsorbed phase on an elongating NW is instead quantified by calculating the residence time correlation function:[172]

$$R(t) = \left\langle \frac{1}{N} \sum_{i=1}^{N} \theta(t_0)\theta(t_0 + t) \right\rangle \tag{3.20}$$

where $\theta(t_0)$ equals one when a monolayer molecule is within the wire segment of interest, and zero otherwise. Similarly, $\theta(t_0{+}t)$ equals one if the molecule remains in the monolayer, and zero otherwise. R(t) decays in an exponential fashion, and can thus be written as $\sim e^{-t/\tau}$. The residence time is computed by evaluating:

$$\tau = \int_0^{t_f} R(t) \, dt \tag{3.21}$$

where a delay time, t_f, of 50 ps is selected to isolate the adsorbate mobility along specific areas of the wire and at particular stages of elongation. While τ cannot be directly compared to diffusion and adsorption rate data, it does enable comparisons for monolayer mobility along different areas of a wire.

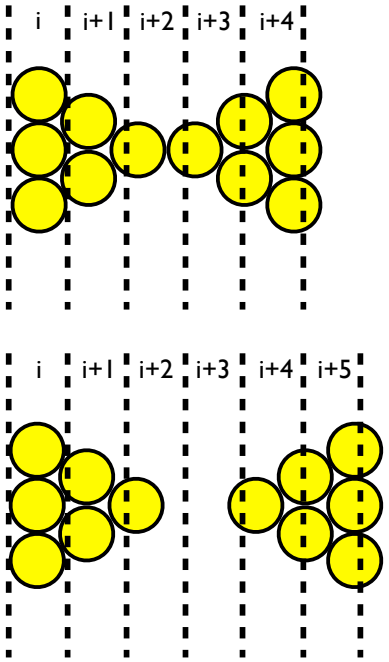

Figure 3.13. Illustration of 1-d binning method for detecting NW rupture. The yellow circles represent Au atoms. In the top image the method confirms that the NW is unbroken while in the bottom image the method detects a break. Note that in practice the bins are overlapping to ensure high precision in break detection.

3.4.4 Detection of Nanowire Failure

In Chapters IV and VII the ductile elongation is computed by using a 1-d binning algorithm to detect NW rupture. Figure 3.13 illustrates how the algorithm works. Bins with a width equal to the diameter of a Au atom (2.88 Å) are setup along the axial direction of the NW, starting at one end of the NW and ending at the other end. The algorithm counts the number of Au atoms whose center of mass is within each bin. If any of the bins are empty, the algorithm detects a break. For example, in the top image of Figure 3.13 all bins contain at least one Au atom, while in the bottom image the (i+3)th bin is empty. To increase the resolution of break detection, in practice the bins overlap with one another, such that a single Au atom may reside in multiple bins. This ensures that the break is detected as soon after rupture as possible.

3.4.5 Stress-Strain Calculations

In Chapter VII the stress-strain relationship is computed as a metric for discriminating between ductile and brittle failure. The engineering strain, ε, is calculated using the expression

$$\varepsilon = \frac{L - L_0}{L_0}, \tag{3.22}$$

where L is the instantaneous length of the wire. The stress, σ_{xx}, along the direction of stretching is calculated

using the virial expression [173,174]

$$\sigma_{xx} = \frac{1}{V}\sum_{i}\left[\frac{1}{2}\sum_{j} r_{x,ij}F_{x,ij} - mv_{x,i}v_{x,j}\right], \tag{3.23}$$

where V is the volume of the NW, $r_{x,ij}$ and $F_{x,ij}$ are the inter-atomic distance and the force between atoms i and j in the x direction, m is the mass of a Au atom, and $v_{x,i}$ ($v_{x,j}$) is the velocity of atom i (j) in the x direction. In accordance with previous work,[175] V is calculated from the hard-sphere volumes of the Au atoms and remains constant throughout elongation.

CHAPTER IV

GOLD NANOWIRE ELONGATION IN ADSORBATE

This chapter considers the mechanical and structural behavior of Au NWs elongated in the presence of physisorbing propane solvent. A wide range of adsorbing species is considered, from those exhibiting minimal adsorption to the limit of chemisorption. Three models of all-atom propane, each with different binding strengths, are employed, as well as a generic, single-site model that is easily tailored to span a large range of solvent-wire interactions. To gather a comprehensive and statistical view of the effect of molecular adsorption on Au NW elongation, a large number of simulations (390 in total) are performed spanning different wire sizes. This study provides an important first step towards the overall goal of developing a framework for the study chemisorbing single-molecule junctions. This work is published in reference 72.

4.1 Introduction

Understanding the structures of 0-d and 1-d nanomaterials is an important step towards designing and tailoring the properties of materials on the nanoscale.[176] The Au NW is an example of a 1-d nanomaterial whose structures and properties have been widely studied[77,78,112,121–129,142,177–185] and utilized for novel nanoscale applications (e.g., nanowelding[135], nanosprings[186], and molecular sensors[187]). In particular, the electrical and mechanical behaviors of Au NWs have garnered considerable attention due to unique structure-dependent features that are observed during elongation of the wires. Measurements of conductance and force of an elongating Au NW exhibit stepwise (*i.e.*, quantized)[112,121–124] and sawtooth-like[124] changes, respectively, suggesting that the structure of Au NWs undergoes sudden atomic rearrangements as a mechanism for relieving the stress induced through stretching. Experimentally, various high-energy structures have been observed during the stretching process, including disordered chunks,[177] helical ribbon-like structures,[125,127–129] and monatomic chains.[125–127] A number of strategies have been employed in an attempt to facilitate the formation of these characteristic high-energy structures. Rodrigues *et al.*[127] observed remarkable reproducibility of the appearance of monatomic chains when Au NWs were elongated in the [100] or [111] directions. Pu and co-workers[78] used MD simulations to show that the emergence of long monatomic chains is promoted by elongation rates that are high enough to preclude the relaxation of low-energy defect modes in the system.

Observing important structural events at the atomic level, as well as precisely controlling the conditions under which a Au NW is stretched, can be extremely challenging in an experimental setting. For example, despite important experimental progress that now enables electron transport measurements to be made on the nanosecond timescale,[188] such measurements remain too slow for observing the breakdown event of a Au

NW. As an alternative to running experiments, atomic-based simulations can be performed to study Au NW elongation. In simulations the features of a system can be controlled and measured with femtosecond and sub-angstrom resolution. A vast majority of simulation studies to date have focused on Au NWs undergoing elongation in vacuum,[77,78,125,179–184] even though many important applications are conducted in non-vacuum environments. One notable example is metal-molecule-metal MCBJ experiments,[6,13,34,189,190] in which a Au NW undergoes chemisorption with an adsorbate prior to elongation. By performing simulations of Au NW elongation in an adsorbate, realistic geometries for subsequent first-principles calculations of conductance can be obtained. Direct force calculations have already played a large role in an ongoing effort to reconcile experimental measurements with theoretical predictions of the conductance through metal-molecule-metal structures.[64–66,68,71,191]

Moreover, the presence of an adsorbate may lead to the appearance of certain structural motifs preferentially over others in elongating Au NWs. He *et al.*[142] performed STM-BJ experiments to test the effect of molecular adsorption on monatomic chain stability, finding that high-energy structures are stabilized by the presence of a strong adsorbate. In these experiments, the presence and stability of monatomic chains were inferred from conductance measurements through the Au NWs. However, previous work in the same group showed that the presence of adsorbate molecules can reduce the conductance through monatomic chains by as much as 50%,[192] making the results of He *et al.* somewhat ambiguous. Thus, validating the conclusions of He *et al.* by directly observing the structural features of elongating Au NWs in adsorbates would be valuable.

4.2 Simulation Details

Three [100]-oriented Au NWs with different initial diameters are used for these simulations. Each of the Au NWs is initially 12.3 nm in length. The Au NWs are generated by taking cylindrical cuts from a FCC lattice of diameter 1.1, 1.5, and 1.9 nm, as shown in Figure 5.2. Elongation is carried out using the stretch-and-relax MD technique described in subsection 3.2.1, with gripping atoms on the right end of the wire periodically displaced a small amount (0.1 Å) in the [100] direction. The core atoms are allowed to relax for 10 ps between displacements of the gripping atoms, corresponding to a nominal elongation rate of 1.0 m/s.

To prepare the simulation boxes, isobaric-isothermal (constant NPT) MD simulations of pure propane are first performed at a target temperature of 298 K and pressure of 42.5 bar. These conditions are chosen to obtain a dense liquid state of propane. The boxes of propane are sufficiently long in the direction of pulling to allow for elongation and rupture of the wire. Once the box of propane is equilibrated at constant temperature and pressure, the Au NW is inserted into the center of the box. Propane molecules overlapping with the wire are then removed from the box. Before stretching the wire, the propane and Au NW are equilibrated in the

canonical ensemble (constant NVT) for 50 ps. Elongation of the Au NWs is also performed in the canonical ensemble.

For the LJ/Prop-X systems, the equations of motion are integrated via the velocity Verlet algorithm with a time step of 1.0 fs. For the AA/Prop-Y systems, the equations of motion are integrated via the velocity Verlet algorithm combined with the rRESPA multi-timescale integrator, with an outer loop time step of 1.0 fs (for intermolecular computations) and an inner loop time step of 0.2 fs (for intramolecular computations). Excellent energy conservation is obtained for this integration scheme.

4.3 Adsorbate Behavior

Altering the strength of interaction between an adsorbate and Au NW gives rise to different adsorbed phase behaviors. As one might expect, stronger interactions result in a fluid that is more tightly bound to the

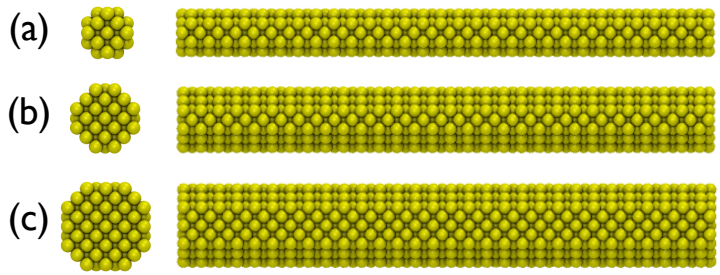

Figure 4.1. Top (left) and side (right) views of Au NWs with diameters of (a) 1.1 nm, (b) 1.5 nm, and (c) 1.9 nm. The wires contain 630, 1110, and 2070 atoms, respectively.

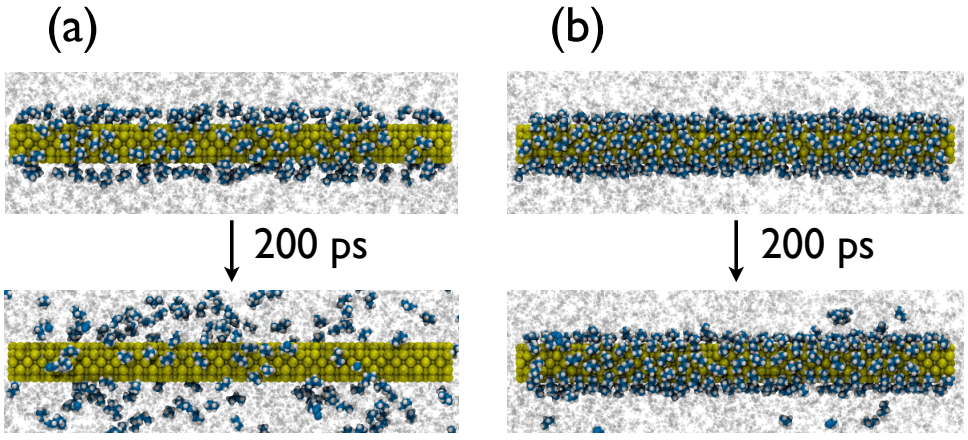

Figure 4.2. Snapshots depicting the structure and mobility of monolayer molecules around a 1.1-nm Au NW for the (a) AA/Prop-MP2 and (b) AA/Prop-FCC models. The top snapshots show the monolayer molecules (whose atoms are rendered as van der Waals spheres) at a given instant in time, while the bottom snapshots show these same molecules 200 ps later. Molecules outside of the initial monolayer are rendered as grey "ghost" molecules.

surface. This can be seen in Figure 4.2, where the top images depict the monolayers on a 1.1-nm Au NW resulting from application of the AA/Prop-MP2 and AA/Prop-FCC models. The bottom images in Figure 4.2 depict the molecules that 200 ps prior were adsorbed to the Au NW surface. While the molecules in the AA/Prop-MP2 system predominantly detach from the Au NW surface, a vast majority of the molecules in the AA/Prop-FCC system remain on the surface after 200 ps. A stronger interaction leads to higher surface densities, which, in turn, result in a lower mobility of the adsorbate on the Au NW surface while also suppressing the flux of molecules into and out of the monolayer.

Quantifying such differences can provide a convenient way to select or design an adsorbate to yield desired Au NW behavior, as it is likely that the properties of the adsorbed phase correlate with the structural or mechanical behavior of elongating Au NWs. MD simulations of propane molecules around a fixed Au NW are performed to calculate the equilibrium properties of the monolayer. Following 150 ps of equilibration, trajectories are saved every 10 fs for 200 ps to calculate various properties of the adsorbed phase.

4.3.1 Adsorbate Behavior on Unstretched Nanowires

4.3.1.1 Structure

First, the structure of the adsorbate is analyzed by computing the adsorbed phase density away from the Au NW surface. The distance from the surface of each adsorbate molecule is computed by taking the average of the pair distances between the adsorbate center of mass and its three nearest Au atoms. Representative

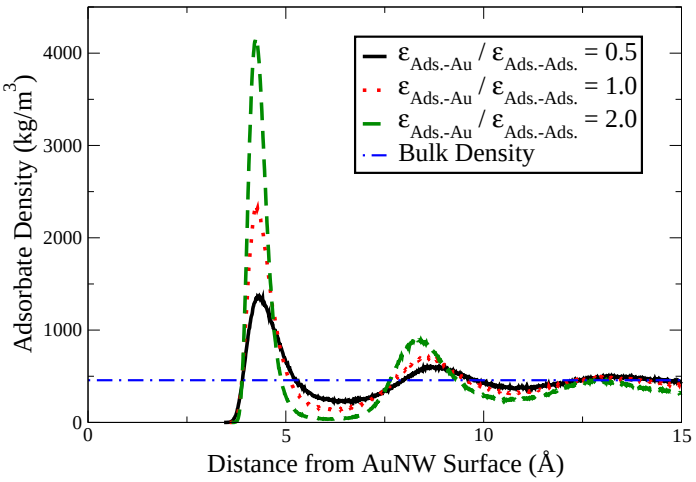

Figure 4.3. Adsorbate densities around a 1.1-nm Au NW for LJ/Prop-X model using three different interaction strengths.

curves for three different LJ/Prop-X systems are shown in Figure 4.3, with the bulk density for the LJ/Prop-X model also plotted for reference. The bulk density for the LJ/Prop-X model is 457 kg/m^3, which compares well to previous MD results of liquid propane run at slightly different conditions.[193] For all three systems, a sharp initial peak (corresponding to the adsorbed monolayer) rises well above the bulk density value at a distance from the surface of 4.22 Å. The initial peak is higher for systems in which the adsorbate-Au interaction is stronger. The second peak is shifted towards the Au NW surface for stronger adsorbate-Au interactions. The trough that occurs between the first and second peaks is similarly shifted. This trough occurs at a distance from the nanowire, r_{boundary}, that is taken to be the monolayer boundary and varies from system to system. The narrowing of the first peak for higher interaction strengths signifies that the monolayer is packed more tightly in the radial direction around the Au NW. A slight drop in density below the bulk value occurs at the box boundaries due to the adsorption of molecules onto the Au NW and out of the bulk phase.

The surface coverage, Θ, is next computed by dividing the number of molecules in the monolayer (*i.e.*, molecules located at a distance from the surface of less than r_{boundary}) by the number of Au surface atoms. Surface coverage is dictated by the interplay between entropic (packing and conformational) and enthalpic (adsorbate-adsorbent and adsorbate-adsorbate interactions) factors.[194,195] For calculations of Θ, molecules at the ends of the wire are not considered to be a part of the monolayer, so the reported values represent coverages for a Au NW that extends infinitely in the [100] direction. Results for three different wire sizes are

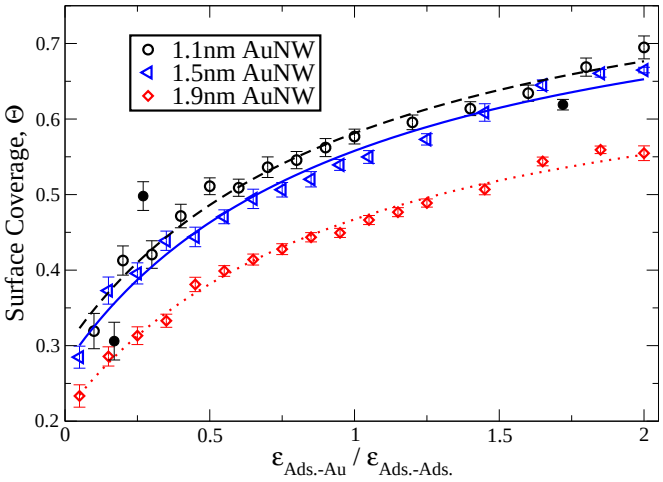

Figure 4.4. LJ/Prop-X (unfilled symbols) monolayer coverage on 1.1-nm, 1.5-nm, and 1.9-nm Au NWs. Langmuir isotherm-type curves are fit to each set of LJ/Prop-X data. AA/Prop-Y data (filled symbols) are also plotted for the 1.1-nm Au NW.

shown in Figure 4.4. The surface coverage data is fit to a Langmuir isotherm-type functional form:

$$\Theta = \alpha \frac{X}{1+X} + \beta \tag{4.1}$$

where $X = \varepsilon_{Ads.-Au}/\varepsilon_{Ads.-Ads.}$ and α and β are fitting parameters. Physically, α may be thought of as the gain in surface coverage obtained through increases in the adsorbate-Au interaction strength, while β represents the surface coverage at vanishingly small adsorbate-Au interaction strengths. Previous experimental measurements reported coverages between 0.18-0.33 for physisorbed and chemisorbed monolayers on Au(111) surfaces.[140,196] For Au nanoparticles with core diameters of less than 2 nm (representing a highly curved surface), values for Θ between 0.68-0.80 have been reported both experimentally[197] and theoretically[198] for chemisorbed monolayers. Our values for Θ on 1.1-nm Au NWs at high adsorbate-Au interaction strengths agree with these previously reported data. Results for the larger Au NWs are lower than previously reported data. Further increases in interaction strengths (*e.g.*, up to typical values for chemisorption) would likely yield better agreement. At low interaction strengths the propane does not adsorb to the Au NW, thus a low surface coverage is obtained. Molecules close to the Au NW are likely to be pulled away from the surface if $\varepsilon_{Ads.-Au} < \varepsilon_{Ads.-Ads.}$. These molecules can be thought of as generic solvent molecules that collide with the Au NW during elongation. Additionally, thermal-induced desorption may occur when $\varepsilon_{Ads.-Au}/\varepsilon_{Ads.-Ads.}$ is less than or comparable to $k_bT/\varepsilon_{Ads.-Ads.} = 1.07$.

It is well known that increasing curvature of a surface enables higher monolayer coverages due to increases in accessible free volume of the ligand tailgroups.[197–199] Figure 4.4 shows that this trend holds for adsorbates on Au NWs. Not only do smaller wires enable higher coverages, they also yield larger gains in surface coverage with increases in the adsorbate-adsorbent interaction strength. This behavior is quantified by the α parameter in equation 4.1. Table 4.1 shows values for the fitting parameters obtained for the LJ/Prop-X model on different Au NW sizes. α is significantly higher for the two smaller wires than the larger one. This large jump indicates that the larger [100] faces on the 1.9-nm wire surface enable increased intramonolayer interactions.

Table 4.1. Equation 4.1 fitting parameters for LJ/Prop-X systems.

Diameter (nm)	α	β
1.1	0.571	0.299
1.5	0.569	0.273
1.9	0.514	0.210

4.3.1.2 Mobility

In addition to measuring the structure of the adsorbed phase, the mobility of the adsorbate molecules is also analyzed. The mobility of the adsorbed phase is probed by calculating two properties: (*i*) adsorption rate and (*ii*) diffusion, D_x, across the Au NW surface. Adsorption rate describes how molecules move radially around a Au NW while D_x describes how adsorbate molecules move along the wire surface (in the [100] direction).

As shown in Figure 4.5, the adsorption rate and D_x both decrease as the adsorbate-Au interaction strength is increased. The curves in Figure 4.5 are both exponential fits, indicating that both adsorption rate and D_x behave as $\sim e^{\alpha X}$, where α is a constant and X = $\varepsilon_{Ads.-Au}/\varepsilon_{Ads.-Ads.}$. This is consistent with Arrhenius behavior, which predicts mobility of the form $\sim e^{A/kT}$, where A is the activation energy, k is the Boltzmann constant, and T is the temperature. The AA/Prop-Y model results fall mostly below the LJ/Prop-X model results for both measures of mobility. This is likely due to the AA/Prop-Y molecules needing to orient themselves properly in order to diffuse towards and along the Au NW, whereas the LJ/Prop-X molecules experience no such orientation-dependence. Figure 4.5 also shows D_x plotted as a function of adsorbate-Au interaction strength. The measured bulk diffusion value for the LJ/Prop-X model is 1.55 x 10^{-8} m^2/s, which is slightly higher than the value of 1.05 x 10^{-8} m^2/s reported elsewhere for MD simulations of liquid propane.[193] This discrepancy can be attributed to differences in the conditions of the two simulations, which

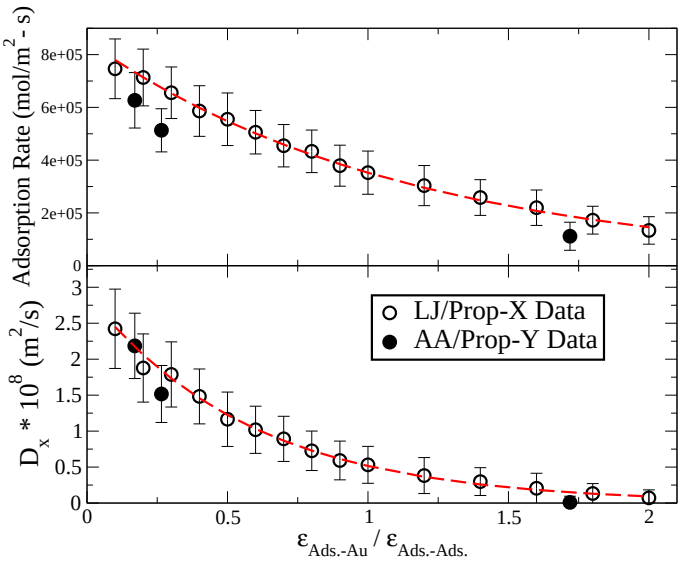

Figure 4.5. Adsorbate mobility on a 1.1-nm Au NW as a function of adsorbate-Au interaction strength. Exponential fits are applied to the LJ/Prop-X data. (Top) Adsorption rate and (Bottom) diffusion along Au NW surface (in [100] direction) are plotted.

result in a higher propane density (548 kg/m^3) in reference 193 than the value obtained here (457 kg/m^3).

4.3.2 Adsorbate Behavior on Stetched Nanowires

4.3.2.1 Structure

Results for a 1.9-nm Au NW elongated in the presence of LJ/Prop-2.0 adsorbate are presented in Figure 4.6. Properties of the monolayer are measured and presented at different stages of elongation. In Figure 4.6 the density (relative to the bulk density) of LJ/Prop-2.0 around a Au NW is presented as color intensity maps. Adsorbate density is measured along the 2.3-nm segment enclosed by the solid lines at the bottom of each Au NW image in Figure 4.6. This segment corresponds the thinning region of the wire at 30 Å of elongation. For consistency, data are averaged along this same segment for each stage of elongation. The monolayer coverage, Θ, and desorption residence time constant, τ, are also shown in Figure 4.6 along different characteristic segments of the wire. These segments are selected to investigate the adsorbate behavior as a function of the local structure along the Au NW surface.

Figure 4.6 reveals many interesting features of the adsorbed phase on an elongating Au NW. Prior to elongation, the color intensity maps reveal that the monolayer is highly ordered, with densities as much as

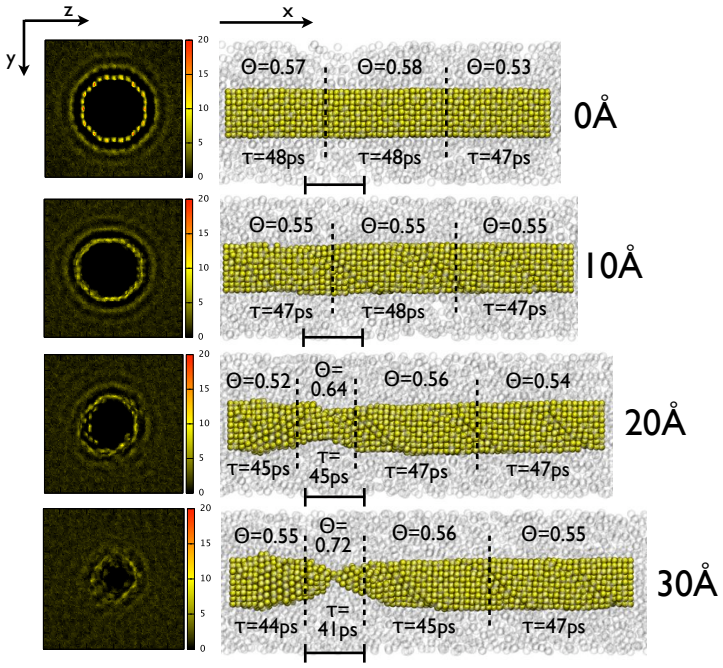

Figure 4.6. Structure and mobility of LJ/Prop-2.0 adsorbate at different stages of elongation of a 1.9-nm Au NW. (Left) Adsorbate density (normalized with respect to the bulk density) along a segment of the wire, from x=3.0 nm to x=5.3 nm. This segment corresponds to the thinning region enclosed by the solid lines at the 30 Å stage of elongation. (Right) The surface coverage, Θ, and desorption residence time, τ, along different segments of the elongating wire.

twenty times higher than that of the bulk fluid. Two additional layers of radially ordered molecules are present beyond the monolayer. As the Au NW is elongated, the monolayer becomes more diffuse and the layers of propane beyond the monolayer become increasingly faint. At 30 Å (immediately prior to rupture of the wire) the adsorbate density is significantly lower than the density prior to elongation. The rapid movement of Au atoms in the thinning region causes these drops in density.

Analyzing the local coverage and mobility of the monolayer in Figure 4.6 provides further insight into the behavior of the adsorbate. First, note that Θ and τ remain steady in regions where no large structural changes have occurred within the wire. Slight structural changes such as the slip planes present at 10 Å elongation do not significantly affect Θ or τ. The region that is most significantly affected is the thinning segment of the wire at 30 Å of elongation. Within this region the surface coverage jumps to 0.72 due to increases in curvature of the Au NW, while the residence time drops from 48 ps prior to elongation to 41 ps, a decrease of $\sim$15%.

4.3.2.2 Mobility

Interestingly, the desorption rate is higher in the region surrounding the thinning segment of the wire than in areas surrounding bulk-like regions of the Au NW. To further probe this phenomena, τ is calculated for molecules within the thinning region of elongating 1.9-nm Au NWs and compared to τ for molecules adsorbed along bulk-like regions of the wire. Ten runs for different adsorbate models are performed. A 1-nm segment in the thinning region is selected for each run, 2 Å prior to rupture of the wire. Results are presented in Figure 4.7. For the LJ/Prop-X models, the monolayer mobility around all regions of the wires gradually increases until X=3.0; the mobility does not change significantly from X=3.0 to X=4.0. For X=3.0 and X=4.0, the interaction energy is high enough to keep virtually all monolayer molecules attached to bulk regions of the wire for 50 ps. The explicit models of propane exhibit similar trends. The mobility of the AA/Prop-UFF model is much higher than that of other models due to its weak interaction with Au. AA/Prop-FCC has a slightly lower mobility than a LJ/Prop-X model with similar interaction strength. This finding is consistent with the results for mobility on an unstretched wire, and is attributed to molecular orientation effects.

Another interesting feature from Figure 4.7 is the consistently higher mobility of adsorbed molecules in neck versus bulk-like regions of the wires. The large fluctuations of Au atoms within the thinning region of the wire are the primary factor responsible for the high monolayer mobility. To demonstrate this, in Figure 4.8 the root-mean-square deviation (RMSD = $\sqrt{\langle (r(t) - r_{avg})^2 \rangle}$) is plotted along the long axis of a 1.9-nm Au NW. The system is allowed to evolve (without stretching of the Au NW) for 5 ns in the presence of different LJ/Prop-X models. The RMSD for each atom is computed relative to its average position (r_{avg}) during the 5-ns trajectory, with the atomic positions saved every 1 ps.

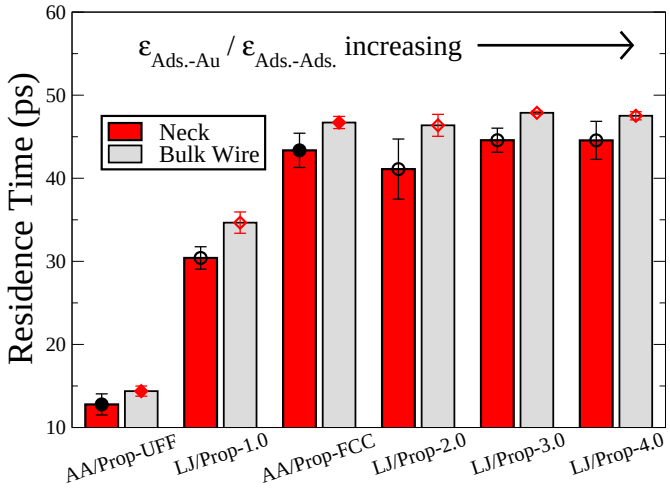

Figure 4.7. Comparison of various adsorbate desorption residence times at the neck (i.e., the thinning region) and in bulk-like regions of elongating 1.9-nm Au NWs.

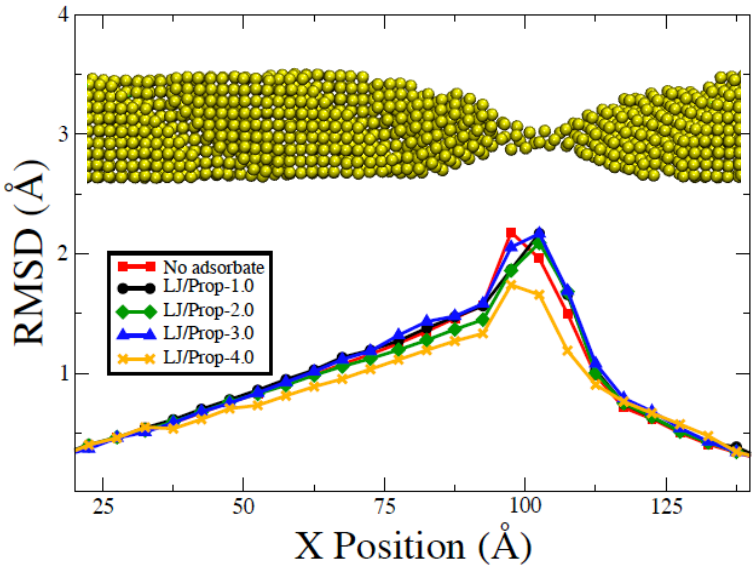

Figure 4.8. Root-mean-square deviation (RMSD) of Au atomic positions along a 1.9-nm Au NW. Curves for the RMSD in vacuum and in different LJ/Prop-X models are shown. Note, wire is shown to scale and matches the *x*-axis.

Figure 4.8 shows that the fluctuations in Au atomic positions are highest in the thinning region of the wire. This indicates that the positions of Au atoms within the thinning region are not as tightly bound as Au atoms in bulk-like regions of the wire, as caused by both the bulk motion of the Au NW and local atomic rearrangements. The large fluctuations in Au atomic positions are likely responsible for the high monolayer mobility surrounding the thinning region.

Outside of the thinning region, the RMSD changes in a linear fashion due to the bulk motion of the Au NW. Results from Figures 4.6 and 4.7 suggest that this bulk motion of the Au NW does not greatly affect the mobility or structure of the monolayer. That is to say, the monolayer properties remain approximately uniform along bulk-like regions of the Au NW during elongation, in spite of the bulk wire motion.

Finally, aside from the LJ/Prop-4.0 system, the RMSD curves in Figure 4.8 are not a strong function of the adsorbate-Au NW interaction strength. The RMSD along the thinning region for LJ/Prop-4.0 is slightly lower than all other systems, indicating that the mobility of these Au atoms is constrained by the strong adsorbate. However, the bulk motion of the Au NW does not seem to be strongly influenced by high adsorbate-Au NW interaction strengths. It is possible that this situation may change for heavier molecules, but such effects are not tested here.

4.4 Gold Nanowire Behavior

The rupture of elongating Au NWs is a stochastic process. Even for Au NWs with the same initial configuration, random fluctuations in atomic trajectories can lead to much different structural pathways during elongation. Thus, to get a comprehensive picture of the mechanical and structural evolution of elongating AuNWs, ten independent (*i.e.*, each using different initial atomic velocities scaled around 298 K) simulations are performed for various combinations of wire size and adsorbate. Results are compared to those obtained for elongation in vacuum, which are based on 50 independent runs for each wire size. The mechanical stability of Au NWs is quantified by measuring the ductile elongation of each run. Ductile elongation is defined here as the total elongation that occurs prior to rupture.

To correlate structural features to the enhanced mechanical stability of Au NWs in adsorbates, the presence of high-energy structural motifs is measured by calculating the diameter in the thinning region of elongating Au NWs. The thinning region of a Au NW is the location where the thickness of the wire is smallest; as such, it is also the area where rupturing of the wire occurs. The confinement of Au atoms to the thinning region leads to the frequent appearance of characteristic structural motifs such as monatomic chains (MACs) and helices. The distinct sizes of these two structures make their appearance straightforward to measure by calculating the diameter of the thinning region. Helix diameters span between 4.5 and 5.25 Å whereas MAC diameters are equal to the atomic diameter of a single Au atom, D_{Au} = 2.88 Å. The lengths of MACs and

helices may vary. In their most basic form, MACs represent a single point-contact between two Au atoms. Longer MACs containing one or more atoms with a coordination number of two can also form. In either case, such an atomic configuration leads to a conductance through the Au NW equal to the conductance quantum (*i.e.*, $G_o = \frac{2e^2}{h} = 77.5\ \mu S$, where e is the charge of an electron and h is Planck's constant) due to the number of conductance channels being reduced to a single channel.[122] This behavior enables experimentalists to detect the presence of MACs by collecting conductance data through Au NWs during the elongation process (*e.g.*, see reference 123). We detect the presence of MACs from a large set of Au NW trajectories by calculating the average diameter along a D_{Au} = 2.88 Å segment of the wire (in the direction of stretching, [100]). The presence of helices is similarly measured by calculating the average diameter along a $3.5*D_{Au}$ = 10.08 Å segment.

4.4.1 Mechanical Stability Enhancement in Adsorbate

4.4.1.1 Ductile Elongation

Results for ductile elongation as a function of adsorbate-AuNW interaction strength are presented in Figure 4.9. The adsorbate-Au NW interaction energy is computed prior to elongation for fixed Au NWs. Figure 4.9 shows that the ductile elongation tends to increase as the adsorbate-Au NW interaction energy is increased, irrespective of wire size. This trend is most noticeable for the 1.1-nm Au NW, as the average ductile elongation changes from 21.4 Å in vacuum (*i.e.*, where adsorbate-AuNW energy is zero) to 70.9

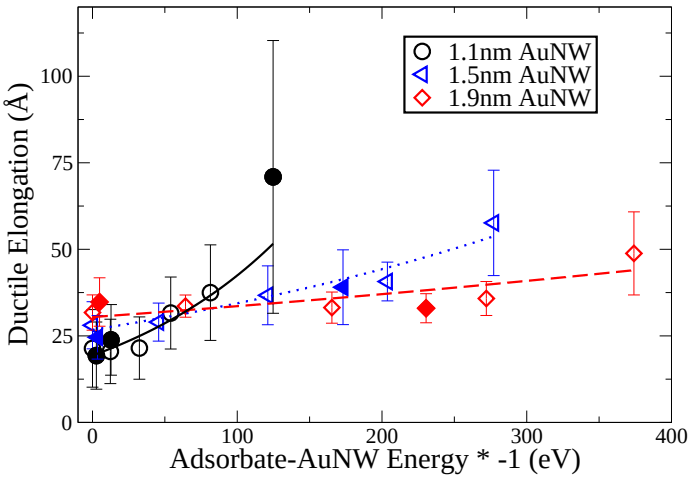

Figure 4.9. Ductile elongation of three wire sizes as a function of adsorbate-Au interaction energy. Unfilled symbols correspond to LJ/Prop-X data while the filled symbols represent AA/Prop-Y data. Exponential fits are applied to LJ/Prop-X data for each wire size.

Å in the AA/Prop-FCC adsorbate, marking a 231% increase in mechanical stability. The enhancements in mechanical stability are smaller for the larger Au NWs. For instance, the change from 31.7 to 48.8 Å marks a 54% increase in mechanical stability for the 1.9-nm Au NW. The larger wires also require higher adsorbate-Au NW interaction energy in order to yield significant improvements in mechanical stability. This is because larger wires contain a greater fraction of atoms within the core of the wire whose energies are not strongly influenced by the adsorbate. The surface coverage on the 1.9-nm Au NW is also significantly lower than the coverages for the smaller wires (see Figure 4.4), so Au atoms on the surface of the larger wire interact with fewer adsorbate molecules. As shown in Figure 4.6, the surface coverage on a large wire remains relatively uniform on all domains of the wire (excluding the thinning region) during elongation. While these domains do not exhibit large differences in surface coverage, surface structures appearing on only one side of a wire could lead to radial anisotropy in the ductility enhancement effect. The data presented here do not reveal such effects for these systems; however, the possibility of anisotropy-induced effects should not be ruled out. More detailed studies are needed in order to resolve this possibility.

While the average ductile elongation increases for higher interaction energies, the reproducibility of mechanical stability decreases with larger values of adsorbate-Au NW interaction energy. Although an adsorbate increases the probability of reaching longer elongations, the stochastic nature of Au NW rupture still results in the occasional breakage at low values of elongation.

4.4.1.2 Mechanical Stability of Au Monatomic Chains in Adsorbate

Analyzing the diameter in the thinning region of Au NWs reveals the appearance of numerous high-energy structures. MACs form in over 90% of all simulations, both in vacuum and in adsorbate, irrespective of wire size and adsorbate-Au NW energy. The fact that MACs form with such high probability is consistent with experimental studies of AuNWs elongated in the [100] direction.[127] Most of the MACs are short in length ($\sim$1-2 atoms) and no correlation between the MAC length and adsorbate-Au NW energy is observed. MACs of length greater than 3.5*D_{Au} = 10.08 Å occur rarely, forming in less than 3% of all runs.

Experimental data from reference 142 indicate that the presence of an adsorbate leads to higher MAC stability. However, it is unclear whether the adsorbate results in longer MACs or simply prolongs the lifetime of the structures. Our results support the latter explanation. Although they do not result in longer MACs, adsorbates do tend to increase the mechanical stability of MACs. This can be seen in FIgure 4.10, where histograms of MAC stability in vacuum and in LJ/Prop-3.0 adsorbate are shown. MAC stability is measured by tracking the amount of elongation that occurs while a MAC is present. The presence of a strong adsorbate shifts the distribution of MAC stability toward higher elongations. For example, 80% of the runs in vacuum result in MAC breakage before 1.2 Å of elongation, compared to just 10% of the runs in LJ/Prop-3.0. The

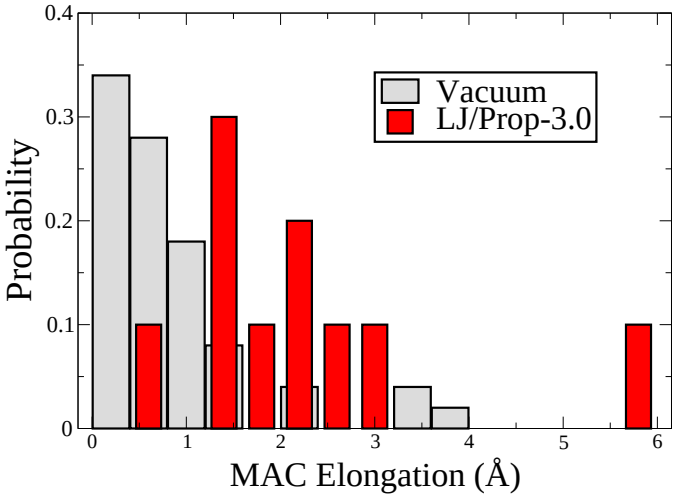

Figure 4.10. Histograms of monatomic chain stability in vacuum and in LJ/Prop-3.0 adsorbate for 1.9-nm Au NWs.

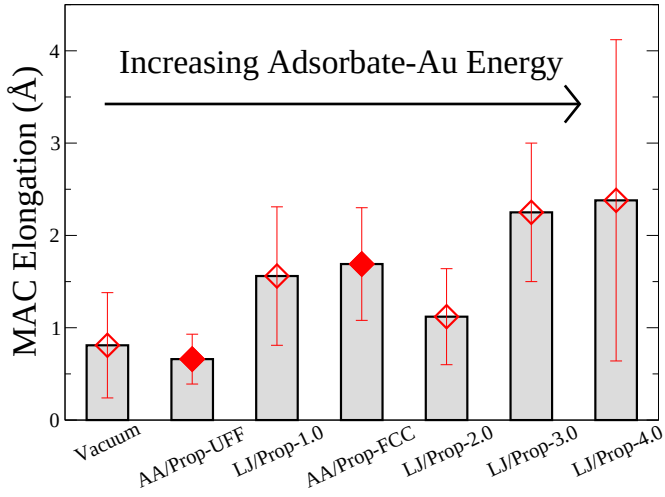

Figure 4.11. Monatomic chain elongation length in vacuum and in various adsorbates for a 1.9-nm Au NW.

presence of an adsorbate also tends to widen the distribution of MAC stability. This effect is demonstrated through the large error bars in Figure 4.11, demonstrating the high sensitivity of MAC breakage to thermal effects and adsorbate collisions with the wire. Figure 4.11 also shows that the average mechanical stability of MACs tends to increase with higher adsorbate-Au interaction strengths. For a 1.9-nm Au NW, the average MAC elongation increases from 0.8 Å in vacuum to 2.4 Å in a strong adsorbate. These values compare well with experimental results (∼1-3 Å) for Au NW elongation in the presence of a mercaptopropionic acid monolayer[142] and toluene.[190]

4.4.1.3 Mechanical Stability of Helices in Adsorbate

Further analysis of the thinning region of elongating Au NWs in adsorbate reveals the appearance of a large number of helical structures. An example of such a helical structure appearing in a 1.9-nm Au NW is shown in Figure 4.12. Multiple research groups have experimentally observed helical structures in Au NWs. For instance, helical core-shell wires with diameters around 0.6 nm have been fabricated and observed.[128,129] Additionally, rod-like helical structures with diameters just under 2 nm have been observed in elongating AuNWs.[125,127] Neither of these structures are thought to be identical to the structure in Figure 4.12; however, the properties and behavior are likely similar.

The statistics of the mechanical stability of helical structures in 1.9-nm Au NWs are shown in Figure 4.13. Helix stability is measured by tracking the amount of Au NW elongation that occurrs with at least one helical structure present. The probability of forming a helical structure is already high in vacuum (78%). However, the probability is consistently higher for Au NWs in adsorbate. Most notably, helices form for LJ/Prop-1.0 and LJ/Prop-3.0 in all ten runs. In addition to forming helical structures more often, the helices that form in the presence of an adsorbate also possess mechanical stability in excess of those that form in

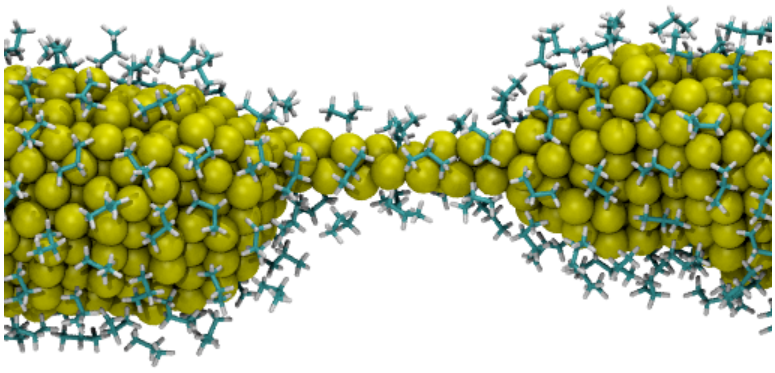

Figure 4.12. Helical formation in 1.9-nm Au NW elongating in AA/Prop-FCC adsorbate. Molecules outside of the monolayer are removed for clarity.

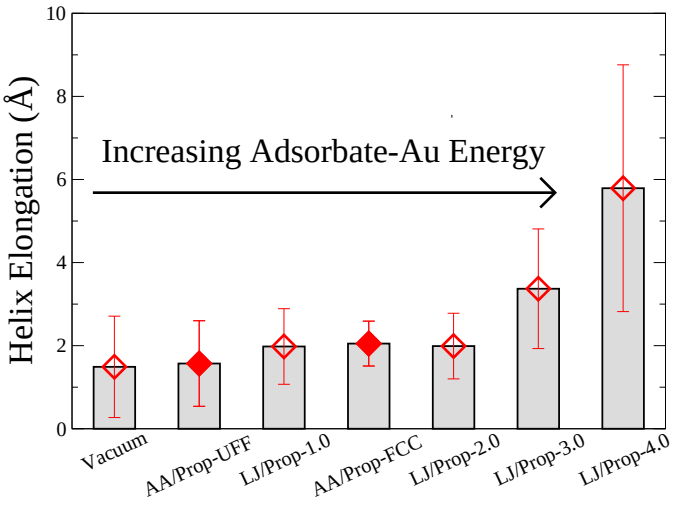

Figure 4.13. Average helix elongation length in vacuum and in various adsorbates for a 1.9-nm Au NW.

vacuum (see Figure 4.13). In fact, the average mechanical stability increases with adsorbate-Au interaction strength, with the changes being more significant after $\varepsilon_{Ads.-Au}/\varepsilon_{Ads.-Ads.}$ exceeds a value of 2.0. The average helix elongation (1.5-5.8 Å) is higher than the average MAC elongation (0.8-2.4 Å), indicating that helical structures possess higher mechanical stability than MACs. The helices that form in adsorbate are also, on average, longer than helices forming in vacuum. For example, while the helices that form for a 1.1-nm Au NW have an average length of 8.2 Å, those forming in AA/Prop-FCC have an average length of 11.7 Å. For a 1.5-nm Au NW, the increase in average helix length goes from 6.6 Å in vacuum to 10.2 Å in LJ/Prop-4.0. Similarly, the increase goes from 6.2 Å in vacuum to 9.1 Å in LJ/Prop-4.0 for 1.9-nm Au NWs.

4.4.1.4 Energetic Mechanism

The mechanism for the enhanced mechanical stability of MACs and helical structures is most easily understood by considering the pertinent energetic factors leading up to Au NW rupture. As a Au NW is elongated, clusters of Au atoms must rearrange themselves to relieve the stress that is induced through stretching of the wire. If the stress becomes too high, and atoms are unable to rearrange themselves quickly enough to counter this stress, the wire ruptures. Atoms on the surface of the wire are further destabilized since they reside in low-coordination environments resulting in higher energies. For this reason, low-coordination structures are especially prone to rupture. If an adsorbate is present during elongation, it can reduce the energy of surface atoms through strong electronic interactions (*e.g.*, dispersion interactions or covalent bonding), thereby reducing the probability of rupture and possibly prolonging the Au NW lifetime. This effect is shown

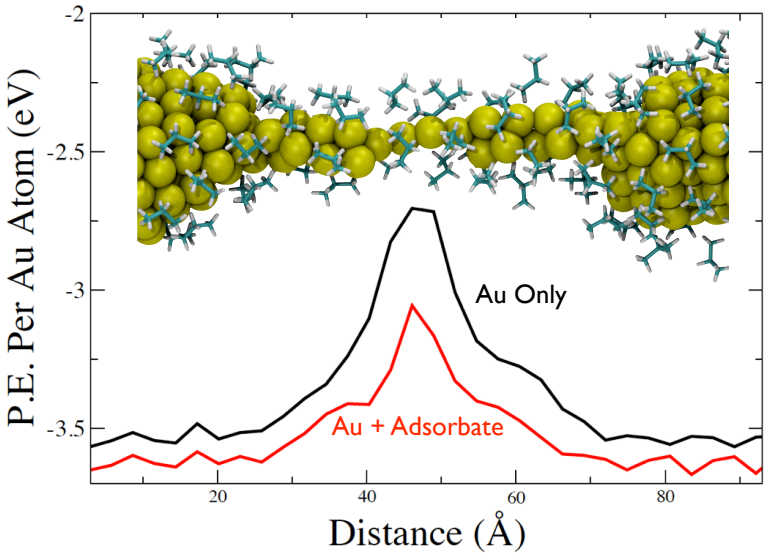

Figure 4.14. (Inset Image) Thinning region of a 1.5-nm Au NW in AA/Prop-FCC. Molecules outside of the monolayer are removed for clarity. (Top Curve) The average potential energy acting on each Au atom in vacuum. (Bottom Curve) The average potential energy acting on each Au atom, including the contribution of both the Au-Au and adsorbate-Au interactions.

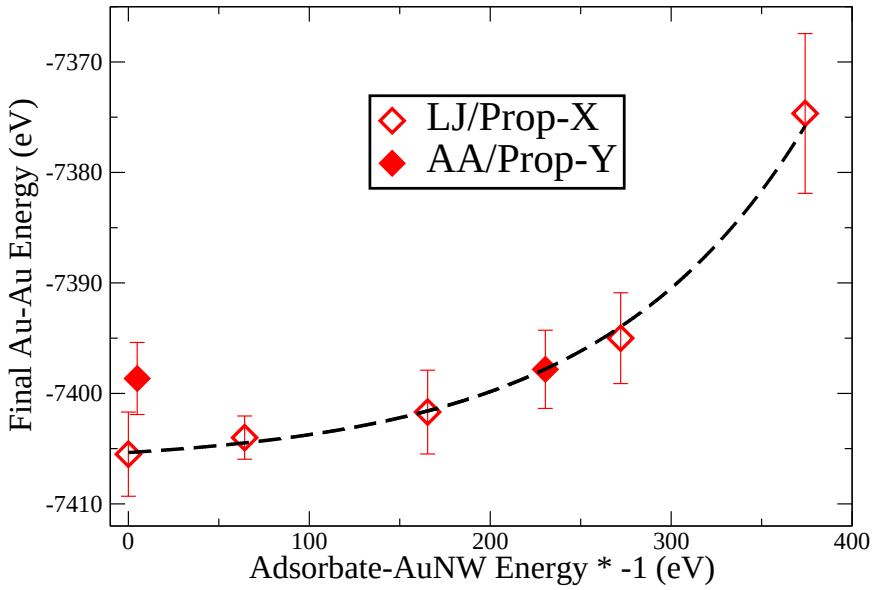

Figure 4.15. Au-Au energy immediately before rupture as a function of adsorbate-Au NW interaction strength for 1.9-nm Au NWs. An exponential fit is applied to the LJ/Prop-X data.

in Figure 4.14, where the average potential energy acting on each Au atom is plotted along the thinning region of an elongating 1.5-nm Au NW. Two scenarios are plotted: the top curve shows the potential energy per particle in vacuum, while the bottom curve includes the contributions of both the Au-Au interactions and the adsorbate-Au interactions. The top curve is obtained by removing the adsorbate molecules from the simulation box and allowing the wire to evolve in vacuum without stretching. Both curves represent the averages of configurations taken every 50 fs for 50 ps. The adsorbate reduces the potential energy acting on Au atoms considerably, especially in areas of low Au coordination.

The effect of an adsorbate on the appearance of high-energy structural motifs is further demonstrated by calculating the Au-Au interaction energy immediately prior to the rupture of 1.9-nm Au NWs. The Au-Au potential energy is plotted as a function of adsorbate-Au NW interaction energy in Figure 4.15. The Au-Au energy increases exponentially with adsorbate-Au NW interaction strength. In other words, Au NWs are able to adopt and maintain unfavorable atomic configurations better in the presence of an adsorbate than in the absence of one. This effect occurs not only because the interaction between the adsorbate and Au NW is stronger, but also by virtue of the fact that higher surface coverages result from higher interaction strengths, providing Au atoms with more adsorbate molecules to interact with. This result provides further evidence that the enhanced mechanical properties observed in Figure 4.9 are the result of the formation of high-energy structural motifs.

4.4.2 Mechanical Destabilization of Au Monatomic Chains in Solvent

The total energy associated with each Au atom is not the only factor that influences Au NW breakage. The forces acting on each atom can also play an important role. For example, a molecular species that does not interact strongly with a Au NW may destabilize high-energy structural motifs through the bombardment of molecules onto the Au NW surface. Previous work[81] in the Cummings group found that such a solvent species does not affect the overall ductile elongation of Au NWs. Although the overall ductile elongation is not affected by a solvent, the mechanical stability of high-energy structures such as MACs may still be influenced. To test this possibility, the MAC mechanical stability is measured in vacuum and in AA/Prop-UFF. AA/Prop-UFF is selected because its $\varepsilon_{Ads.-Au}$ value is the lowest among the adsorbate models tested. The results for three different wire sizes are shown in Figure 4.16. The distributions of MAC stability in vacuum and in AA/Prop-UFF are similar at MAC elongations of less than 2 Å. However, the situation changes at higher elongations. At elongation lengths greater than 2 Å, MAC breakage occurs occasionally in vacuum but never in AA/Prop-UFF. This tightening in the MAC stability distribution is reflected in the standard deviations for MAC mechanical stability relative to the in-vacuum runs. The standard deviations of MAC elongation for 1.1-, 1.5-, and 1.9-nm Au NWs are 2.31, 0.76, and 0.57 Å in vacuum and 0.43, 0.40, and

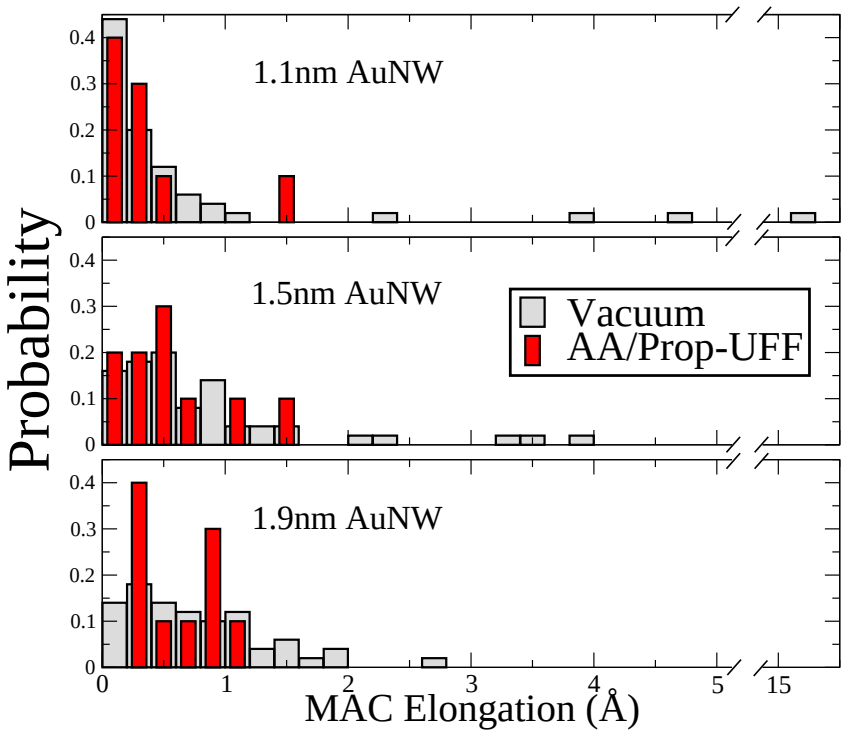

Figure 4.16. Histograms of monatomic chain stability in vacuum and in AA/Prop-UFF adsorbate for (top) 1.1-nm, (middle) 1.5-nm, and (bottom) 1.9-nm Au NWs.

0.27 Å in AA/Prop-UFF, respectively. While MACs are at times able to sustain themselves in vacuum up to high elongations, the bombardment of molecules onto the Au NW surface prevents this from occurring in AA/Prop-UFF.

This is a somewhat surprising result since the mass of propane (44.1 g/mol) is low relative to a Au atom (197.0 g/mol), and illustrates the high instability of MACs. These findings may be even more apparent for heavier molecules that interact weakly with Au and have relatively high mobility. The high monolayer mobility occurring in the thinning region of Au NWs (see Figure 4.7) may additionally help promote MAC breakage by increasing the frequency of solvent collisions with the Au NW surface.

CHAPTER V

ENVIRONMENTAL EFFECTS ON THE FORMATION AND STRUCTURE OF AU-BDT-AU JUNCTIONS

In this chapter, results from from large-scale atomistic simulations of Au-BDT-Au junction formation are presented. Realistic environmental effects such as monolayer interactions, ruptured NW tips, and temperature are incorporated into the simulations, and then compared to results for ideal simulations where these environmental effects are ignored. Specifically, effects on the number of bridged molecules, molecular tilt angle, and metal-molecule bonding geometry are considered. The application of the hybrid MD-MC tool provides opportunities to probe properties in an environment more representative of experiment than any prior theoretical work.[8,28,31,46,59] Furthermore, the computational tractability of the simulation method allows for over 1,000 simulations to be performed, resulting in statistics on par with experiment. This work is published in reference 73.

5.1 Introduction

Conductance measurements through molecular junctions (MJs) have been at the forefront of nanoscale research for over a decade.[58,101,103] This work is motivated by the potential for fabrication of molecular-based electronic circuit elements[55] and, perhaps more so, discrepancies in the experimentally[6] and theoretically[57] reported conductance through a single molecule. The discrepancies have improved over the years,[56] due in part to the development of highly automated and optimized experimental techniques (*e.g.*, scanning tunneling microscopy break junction method,[24,25,113] nanofabricated mechanically-controllable break junction technique[11,16]), as well as the emergence of theoretical tools (*e.g.*, self-consistent GW calculations,[119] approximate self-interaction corrections[67,86]) capable of more accurately describing the HOMO-LUMO gap and energy level lineup between a molecule and two leads. Moreover, it has been repeatedly demonstrated that a spectrum of structures exist in the experiments, some of which seem to appear more frequently than others based on the relative peak heights in histograms of the conductance.[11,16,22–26,28,31,49–51,113] For example, recent low-temperature (4.2 K) measurements of BDT showed several peaks between $10^{-3}G_0$ and $0.5G_0$, where $G_0=\frac{2e^2}{h}$.[22] Results such as these have shifted focus away from reproducing a single value of conductance towards, more generally, determining the structures responsible for the most-probable conductance values in a given experimental setup.[51] Taking cues from experiments, researchers on the theoretical side have recently begun calculating the conductance of an ensemble of MJ structures.[64–71] Structures are obtained using MD simulations in which the MJ is evolved through mechanical elongation[64–67] or compression,[66] or

by thermal activation.[68–71] Valuable information about how local structural conformations (*e.g*, oligomeric gold-thiolate units[65] and tilt angle[66]) influence the trends in conductance has been provided by these studies. However, environmental factors (*e.g*., monolayer interactions, non-ideal electrode geometry) have not yet been included in these simulations, despite the fact that they are likely to influence the results.[35,51]

Balancing accuracy and computational efficiency is a major challenge for simulations of MJs. Simulations need to accurately capture the preferred bonding geometries while also incorporating environmental factors found in experiment. Quantum mechanical (QM)-based methods, such as density functional theory (DFT), are capable of accurately resolving molecular-level bonding, but the high computational cost of QM methods may limit the system size, reduce the total number of independent statepoints, and require simplifications to the local junction environment (*e.g*., neglecting monolayer effects, employing ideal electrode geometries, and considering single-molecule junctions only).[63–67,84,191] Additionally, energy minimizations often included in DFT calculations[66,67] may produce configurations that are not likely for thermal systems. Methods based on classical force fields have also been used to simulate MJs.[68–71] and related systems[72,78,82] Classical force field (CFF) methods (*i.e*., MD and MC simulation[158]) are able to handle larger system sizes and more statepoints than QM methods; however, metal-molecule interfaces exhibit complex bonding with preferred bonding sites that cannot be easily captured by conventional CFF models and methods.[80] Previous CFF-based MD simulations of MJs have only considered ideal junction environments, *e.g*., a single molecule sandwiched between perfectly flat electrode surfaces.[68,69,71] This is in contrast to experimental systems, where the bridged molecule may be surrounded by other adsorbed molecules (*i.e*., a monolayer) with electrodes that have curved geometries resulting from, *e.g*., the rupturing of a Au NW, as carried out in the mechanically controllable break-junction (MCBJ) experimental technique.[6,11,16] Reactive force fields (*e.g*., ReaxFF) have shown promise as a compromise between QM and CFF methods,[130] but parameters for metal-molecule systems are still under development.

5.2 Simulation Details

To generate non-ideal electrodes that are representative of those found in MCBJ experiments, ten independent simulations of the elongation and rupture of BDT-coated 1.9-nm-diameter Au NWs (see Figure ref) are performed (see Methods). The NWs are elongated in the [001] direction at a rate of 1 m/s and temperature of 298 K using the hybrid MD-MC technique described in subsection 3.2.3. In order to model BDT chemisorption, every ten elongations (*i.e*., every 1 Å of NW elongation) MC sampling is performed, with 60,000 fixed-μVT (where μ is the chemical potential of a BDT molecule, V is volume, and T is temperature) moves followed by 160,000 fixed-NVT (where N is the number of BDT molecules) moves.

The next step in the MCBJ process, and the aspect that is the focus of this chapter, is the formation of

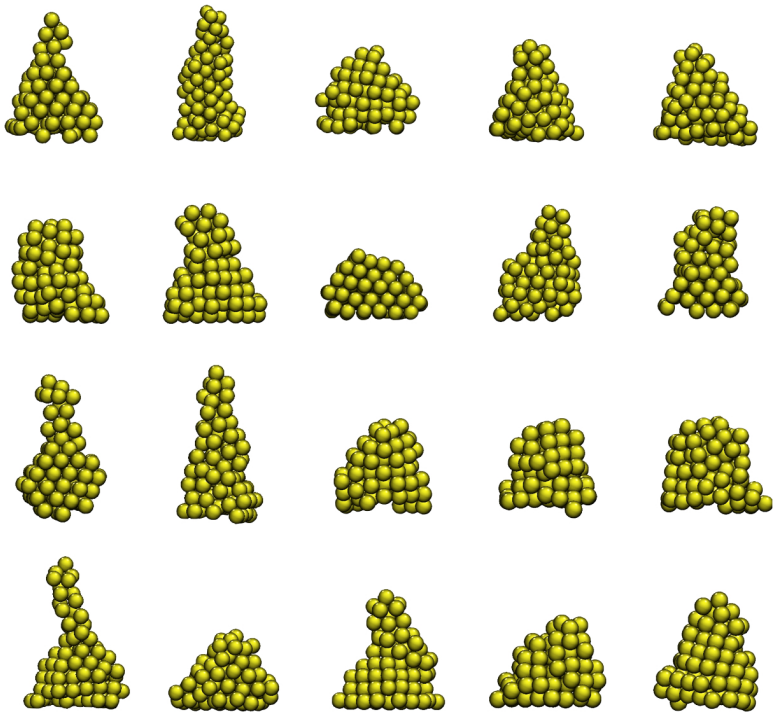

Figure 5.1. Snapshots of the twenty ruptured Au NW tips used in this study.

a molecular junction, which is simulated using a MC-based method. Coupling each ruptured NW tip with one another (including a tip with itself) yields a total of 210 unique electrode-electrode combinations for performing simulations of the molecular junction formation process. Following NW rupture, each BDT-functionalized Au tip is allowed to relax its structure at 298 K using MD. Since molecular junctions form locally in the break junction created by NW rupture, 100 Au atoms at each tip are extracted prior to pushing the tips together, which considerably reduces the computational rigor of the simulations. The twenty 100-atom bare Au tips are shown in Figure 5.1. The target surface coverage is obtained by performing MC simulations at constant μVT. To obtain different monolayer arrangements on the tips, all chemisorbed BDT are removed and simulations are performed with the bare Au tip as the starting point, initializing the psuedorandom number generator of each simulation with a different random seed. Next, the bulk BDT is "evaporated" from the simulation box, which is a standard practice[6] in real experiments. In the simulation, "evaporation" is accomplished simply by removing from the simulation box all of the BDT molecules not bonded to one or more Au atoms. Following this, the BDT SAM is equilibrated at constant NVT for 20 million MC moves. Only one S atom in a BDT molecule is allowed to bond to the electrode during this process; however, BDT molecules are allowed to lie flat on an electrode with both S atoms bonded during the subsequent molecular junction formation runs.

Before simulating junction formation, the Au tips are first displaced in the *x*-*y* plane such that the bottom-

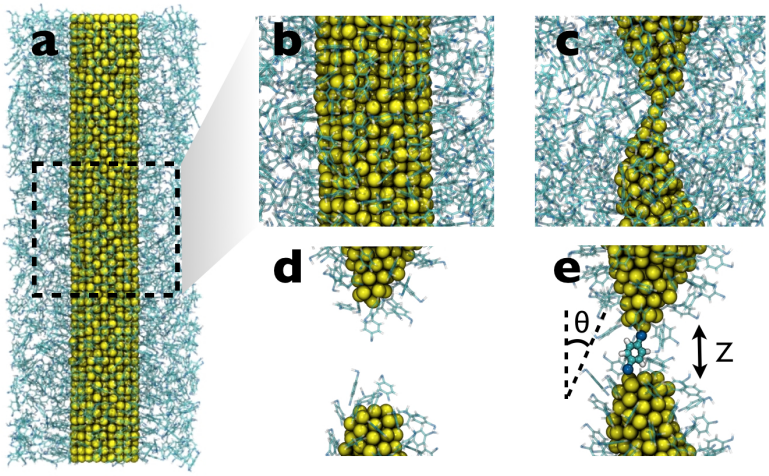

Figure 5.2. Simulation snapshots of the MCBJ method. (a) BDT self-assembles onto an unstretched Au NW; a closeup is shown in (b). (c) Au point contact in the necked region of the NW after ∼3.5 nm of elongation. (d) Following NW rupture, the bulk BDT is evaporated from the simulation box. (e) The ruptured NW tips are brought together, resulting in the formation of a molecular junction.

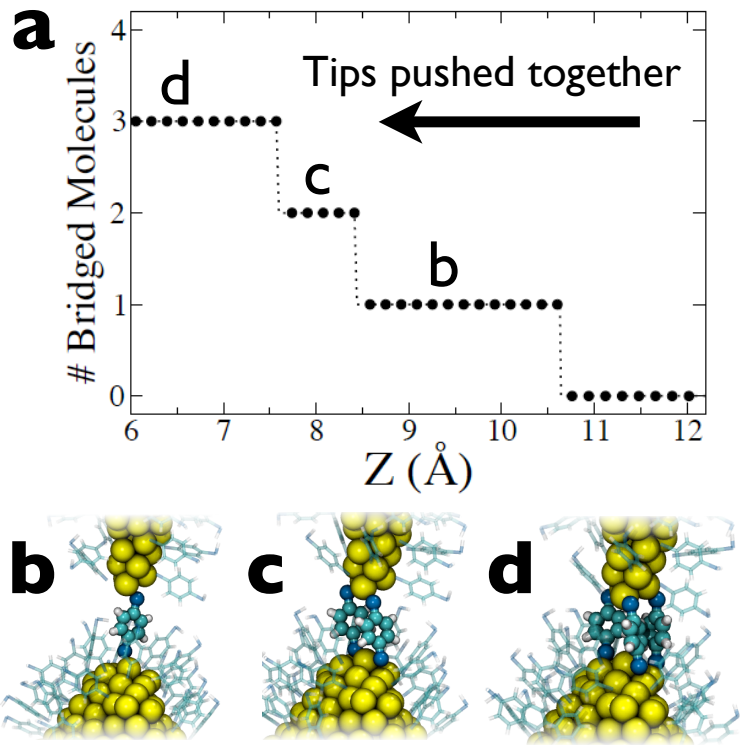

Figure 5.3. (a) Typical plot showing the number of bridged BDTs as the interelectrode separation, Z, is decreased. This particular simulation results in (b) one bridged molecule from $Z \sim$ 10.6-8.4 Å, (c) two bridged molecules from $Z \sim$ 8.4-7.6 Å, and (d) three bridged molecules from $Z \sim$ 7.6-6.0 Å, with the corresponding images shown below. The bridged and non-bridged BDT are rendered differently in the images for clarity.

most and top-most Au atoms in the top and bottom tips, respectively, are aligned along the z-axis. The tips are then gradually pushed together, from Z = 20 Å to Z = 6 Å (where Z is the inter-electrode distance), over the course of 25 million MC moves. Each run ends at Z = 6 Å since direct tunneling between electrodes has been shown to occur for $Z < 6$ Å.[66,67] The entire simulation process, from elongating and rupturing the BDT-coated NW, to forming a molecular junction, is shown in Figure 5.2.

Figure 5.3a shows a typical plot of the number of bridged BDT molecules as Z is decreased. Initially, at large values of Z, zero molecules are chemically attached to both electrodes. At $Z < 11$ Å, a single-molecule junction forms, as shown in Figure 5.3b. As Z is decreased further, two (Figure 5.3c) and eventually three (Figure 5.3d) molecules connect in parallel.

5.3 Relationship Between Monolayer Density and Number of Bridged BDT

The impact of monolayer packing is first explored by performing 210 simulations for each of four different surface coverages: 0.30, 0.40, 0.50, and 0.65 +/- 0.03. Surface coverage is defined here as the number of adsorbed molecules divided by the number of Au surface atoms. 0.65 +/- 0.03 is the maximum surface coverage obtained for the 20 ruptured Au NW tips, which closely matches the reported coverage for alkanethiolates on Au nanoparticles of diameter 1.3-1.4 nm.[197]

Using molecule number data such as those shown in 5.3a, histograms (see Figure 5.4) are constructed of the number of bridged molecules as a function of Z, with separate panels representing (from top to bottom) decreasing surface coverage and the color of the histogram bars corresponding to the number of bridged BDT molecules (n). The histograms of bridged molecules tend to increase with decreasing Z, with the exception of the n = 1 case, which exhibits a peak at all four surface coverages. These peaks, which are indicated with red arrows, appear due to the rate of formation of multi-molecule junctions exceeding that of single-molecule junctions; these peaks shift to higher Z for lower surface coverages.

Figure 5.4 also shows that n, the number of bridged molecules, depends on surface coverage. For most Z, the formation of at least one bridged molecule (n ¿ 0) is most likely for surface coverage 0.50 and least likely for 0.30. The optimal surface coverage for forming a single bridged BDT (n = 1) depends on Z; for Z ¿ 10 Å, intermediate coverages (0.40/0.50) provide the highest probability, while for Z ¡ 9 Å, n = 1 is most probable at maximum coverage (0.65 +/- 0.03). Low surface coverages (0.30/0.40) tend to result in the highest occurrence of multi-molecule junctions. Experimentally, conductance histograms often exhibit peaks at integer multiples of a fundamental conductance value.[16,23,28,113] Two- and three-molecule peaks often occur in break-junction experiments;[16,23,113] four-molecule peaks have also been observed.[28] These data match the results in Figure 5.4. Additionally, the relative peak heights in experiment generally decrease with larger n, which from Figure 5.4 holds for most surface coverages and values of Z. Thus, the simulated

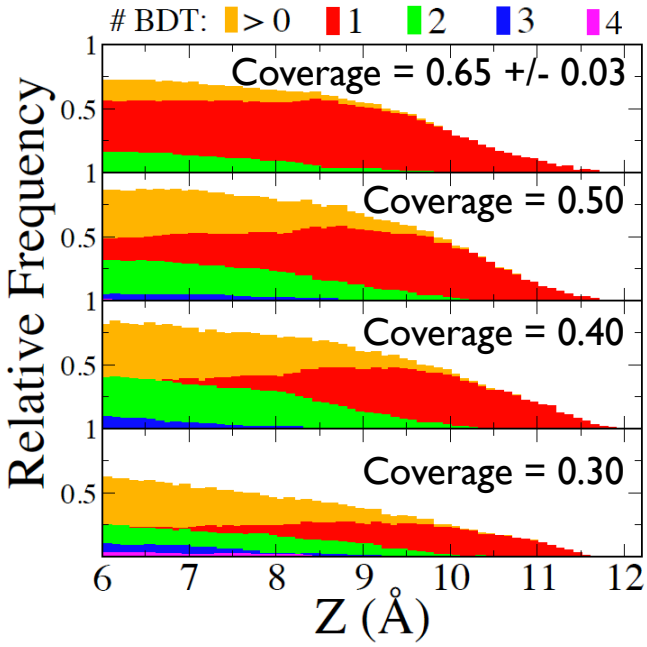

Figure 5.4. Histograms of the number of bridged molecules as a function of Z. The histogram bar colors correspond to the number of bridged molecules. The red arrows indicate the maximum Z at which the single-molecule histograms are at least 98% of their peak values.

junctions result in trends that are in good agreement with experimental results, thus validating the simulation methodology.

It is important to note that surface coverage generally varies between experimental setups, with some experiments conducted at low coverages in order to provide available bonding sites for molecular bridging,[11,18,48,50,51] and others performed with the bridging molecules diluted in a dense matrix of non-bridging adsorbate molecules.[35,44] In the seminal work of Reed and co-workers,[6] the break-junction was exposed to a solution of BDT for a long period of time, resulting in a densely packed monolayer on each of the Au nanotips. Subsequent theoretical work[59] suggested that the low conductance observed by Reed and co-workers could be attributed to weak electrical coupling between two overlapping BDT molecules; in other words, chemical contact between a single molecule and the two electrodes was not established, owing to the lack of available bonding sites on each nanotip. Figure 5.4 shows evidence of such effects, but not to the degree that a single-molecule junction cannot form. That is, squeezing a single molecule into an already dense monolayer is compensated by the addition of a S-Au chemical bond; however, the energetic penalty for fitting more than one molecule is often too great to overcome. Note that the tip curvatures considered here may differ from those of Reed *et al.*,[6] which may influence whether a molecule is able to bridge in densely packed monolayers.

In addition to changing the number of available bonding sites, the packing density of a monolayer also

affects the mobility of adsorbed BDT, and thus influences whether a molecule can adopt one of the specific geometries required for bridging. The reduced interactions between adsorbed BDTs, along with the increased availability of bonding sites, is the cause of the shifting in single-molecule peaks to larger Z at lower coverages, as a second molecule can more easily bridge. This is also the cause for the large n ¿ 0 histograms at intermediate coverages, and large multi-molecule histograms at low coverage. It is somewhat surprising that the formation of three or four bridged BDTs is more likely at low coverage since one might expect the number of molecules on each tip to be the dominant factor in determining the number of bridged molecules[200]. The reduced monolayer interactions are responsible for this somewhat counterintuitive behavior. Also note that in experiments conducted at low coverages, there is often evidence of multi-molecule junctions.[16,50,51] While the exact surface coverage in these experiments is unknown, Figure 5.4 indicates that the relative frequency at which multi-molecule junctions form will depend on Z and surface coverage.

5.4 Role of Non-Ideality

In order to examine the impact of realistic environmental features, MCBJ simulation results are compared with results for ideal junctions. Note that an intermediate surface coverage of 0.40 is used for the remainder of this chapter.

5.4.1 Electrode Geometry Effects

Ideal atomically sharp tips such as those shown in 5.5 are often used in theoretical studies of molecular transport junctions.[8,28,31,46,59] Here, the effect of using an ideal tip is compared to applying ruptured NW tips (see Figure 5.1). Figure 5.5 plots histograms of the number of bridged BDT molecules as a function of Z, with the ideal and NW tip results shown at top and bottom, respectively. The histograms demonstrate a tip geometry dependence; the probability of having $n > 0$ is higher for the ideal tips at $Z < 10$ Å, while the ideal tip histograms change more rapidly than those for the ruptured NW tips.

The impact of tip geometry is further assessed by plotting the bonding geometry as a function of Z, shown in 5.6. The separate panels display the three possible combinations of sites (*i.e.*, on-top/on-top, on-top/on-bridge, and on-bridge/on-bridge) binding a bridged molecule. In general, on-bridge sites become more available for molecular bridging at lower values of Z, especially for the ideal tips where only on-top sites are accessible for bridging at high Z. In contrast to the ideal tip, a ruptured NW tip can be relatively flat at its apex, with on-bridge sites accessible at high Z.

Lastly, Figure 5.7 plots the tilt angle of bridged molecules. Here, a simple compression model is introduced as a first approximation for relating the inter-electrode separation, Z, to the tilt angle, θ:

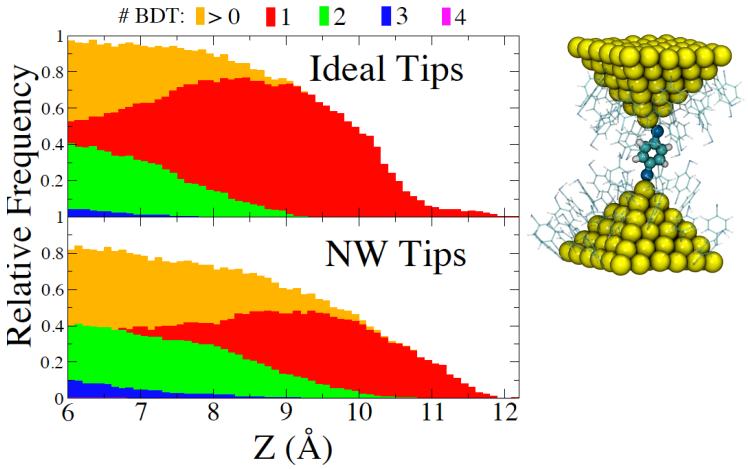

Figure 5.5. Histograms of the number of bridged molecules at various values of Z, comparing results using ideal tips (shown to the right) to ruptured NW tips.

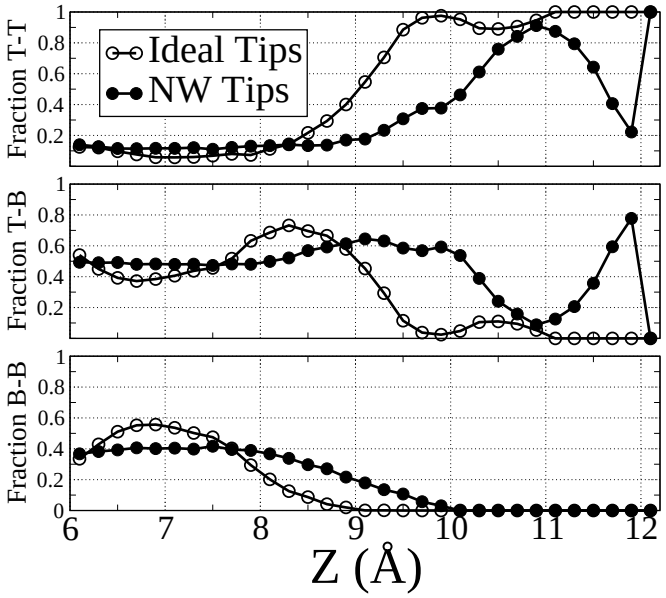

Figure 5.6. The bonding geometry for bridged BDT molecules as a function of Z. Each panel represents the fraction of different combinations of on-top and on-bridge bonding, with (from top to bottom) T-T denoting on-top bonding at both tips, T-B denoting on-top bonding at one tip and on-bridge bonding at the other, and B-B denoting on-bridge bonding at both tips.

$$Z(\theta) = D_{S-S}cos\theta + 2\sqrt{D_{S-Au}^2 - D_{S-S}^2 sin^2\theta}, \tag{5.1}$$

where D_{S-S} is the distance between S atoms in a BDT molecule (6.28 Å for our rigid model of BDT) and D_{S-Au} is the equilibrium S-Au bond distance (2.29 Å for on-top bonding). This model assumes that the S atoms remain bonded to the on-top sites of each tip (with $D_{S-Au} = 2.29$ Å), the BDT center-of-mass falls along

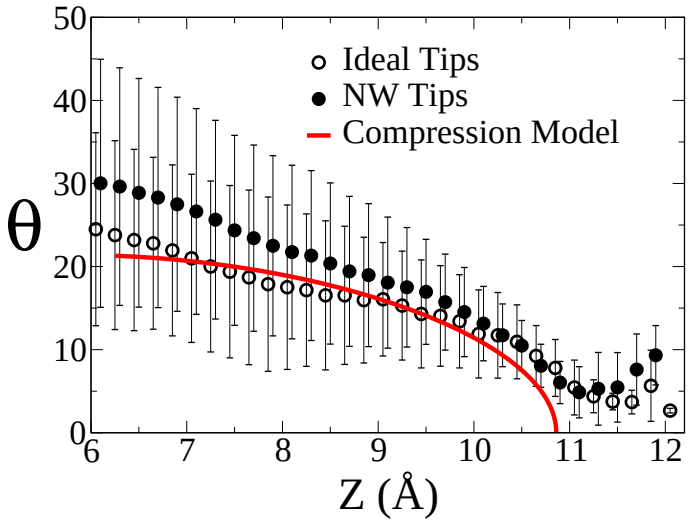

Figure 5.7. The molecular tilt angle, θ, as a function of Z.

the z axis made by the two Au tips, and the tips are aligned in the x-y plane. These first two assumptions often break down for low Z; nonetheless, equation 5.1 establishes a baseline for comparison of tilt angle data, and qualitatively captures the behavior expected from a bridged molecule that remains at the tip apex while compressed, as opposed to one that migrates to sites along the side of a tip. Reasonable agreement is established between the compression model and the tilt angle data in Figure 5.7, especially for the ideal tips. While the tilt angle trajectory of any single bridged molecule may differ significantly from the average behavior, as evidenced by the large uncertainty bars, the average trends are in qualitative agreement with the compression model, suggesting that molecules tend not to migrate to sites along the sides of the tips. For Z $<$ 10 Å the non-ideal tips result in tilt angles that are, on average, higher than those for ideal tips, indicating that the migration of bridged molecules to sites along the side of the tips is less common in systems with non-ideal tips.

5.4.2 Monolayer Effects

Next the effect of a monolayer on the bonding geometry and tilt angle of bridged molecules is demonstrated. After obtaining twenty different monolayer arrangements on the ideal tip, 210 simulations are performed using each unique combination of the twenty BDT-decorated tips. Twelve runs that result in the formation of a single-molecule junction at Z ¿ 11 Åare identified. Using these single-molecule structures as the starting point, simulations are performed in which the remaining monolayer molecules are absent from the electrodes, enabling the impact of adsorbate interactions on the bridged molecule to be assessed.

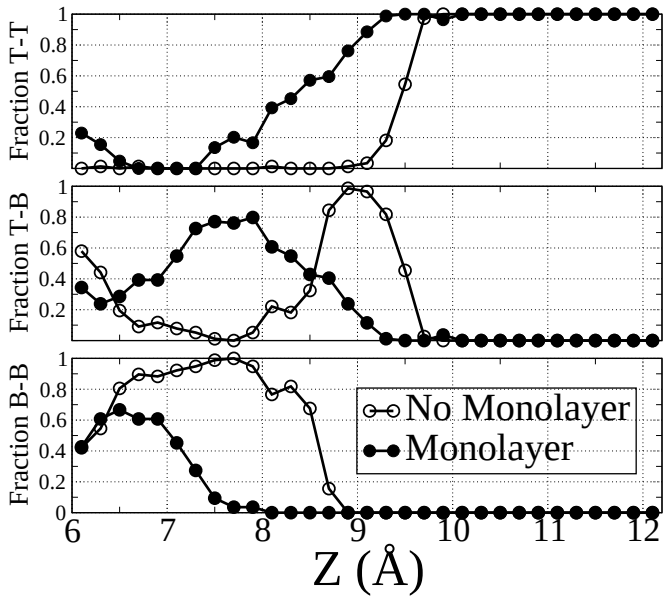

Figure 5.8. The bonding geometry for bridged BDT molecules plotted against Z. See the caption in Figure 5.6 for definitions of the abbreviated terms.

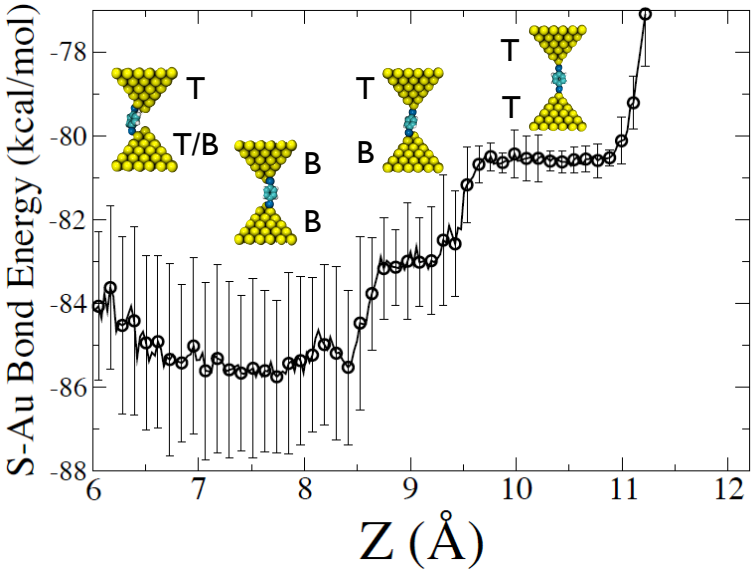

Figure 5.9. S-Au bond energy plotted against Z for a single bridged BDT molecule. No monolayer molecules are present in the simulations.

Figure 5.8 presents the bonding geometry of the bridged molecules, with similar trends observed for the monolayer and no-monolayer scenarios, but quantitative differences. Recall that high monolayer density limits the availability of bonding sites while also reducing molecular mobility, which is responsible for the larger on-bridge peak in the no-monolayer systems shown in Figure 5.8. To further investigate why the bonding geometry changes with Z, it is instructive to analyze the S-Au bond energy. In 5.9 average S-Au bond

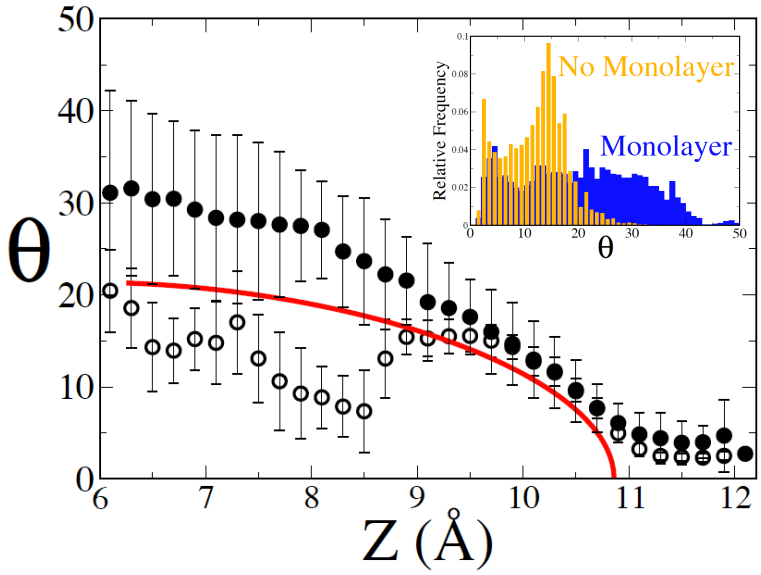

Figure 5.10. The tilt angle, θ, as a function of Z. The filled and unfilled symbols are data corresponding to simulations run with and without a monolayer present, respectively. The red curve plots the compression model (equation 5.1) for comparison. The inset histograms show the distribution of tilt angles.

energy is plotted against Z for the no-monolayer runs. Because there is no monolayer present, the bridged molecule is able to freely explore the energetically favored sites at each tip. At large Z, molecular bridging is only possible with on-top/on-top bonding geometry; as Z is decreased, the energetically more stable on-bridge sites become accessible for bridging; for low values of Z, the compression of the tips gives rise to situations where on-bridge/on-top bonding geometry becomes energetically competitive with a somewhat strained on-bridge/on-bridge connection.

Figure 5.10 plots the tilt angle of bridged molecules in the presence and absence of a monolayer. The compression model (equation 5.1) is also shown (red curve) for reference. Tilt angles of bridged BDTs for $Z > 9.5$ Å agree closely for the cases where a monolayer is present and absent. This regime is characterized by low tilt angles and, for $Z > 11$ Å, long S-Au bond lengths. The maximum value of Z for which a bridged molecule forms is 12.11 Å. This value of Z requires an average S-Au bond length of 2.92 Å, in close agreement with the reported S-Au bond rupture distance of 2.86 Å.[67] For $Z < 9.5$ Å, the monolayer and no-monolayer results differ markedly. In the presence of a monolayer the tilt angles of bridged molecules trend upward, indicative of the confinement of bridged molecules to the tip apex. In absence of a monolayer, the bridged molecules exhibit different tilt angle behavior, undergoing abrupt changes that coincide with changes in the bonding geometry (see 5.8). The inset in 5.10 shows the entire distribution of tilt angles of bridged molecules. Bridged molecules reach a maximum of $\sim 30^\circ$ in absence of a monolayer, and exhibit two preferred tilt angles at 2.5° and 14.5°. On the other hand, the tilt angle distribution for bridged molecules in

the presence of a monolayer is relatively flat from θ=2-35°, with a maximum value of ∼50°.

The highlighted differences for idealized systems are significant since the bonding geometry and tilt angle of bridged molecules have been demonstrated to affect experimentally observed properties, namely conductance and inelastic electron tunneling spectra (IETS). Conductance has been shown to scale linearly with the number of bridged molecules[201], while various studies[11,22,50,83] have demonstrated that bonding geometry and tilt angle can affect conductance by an order of magnitude or more. For example, Haiss and co-workers[50] showed that increasing the BDT tilt angle from θ = 0° to θ = 50° results in close to an order of magnitude increase in conductance, with the most pronounced increases occurring between θ = 30-50°. Recall from the histograms in 5.10 that the maximum tilt angle with a monolayer present is ∼50°, but only ∼30° with no monolayer. Thus, in this case, neglecting monolayer effects could result in significant underpredictions of conductance. In addition to affecting conductance, bonding geometry and tilt angle have also been shown to influence the IETS of molecular junctions.[84]

5.4.3 Temperature Effects

The results presented until now have been for a temperature of 298 K. Next a temperature of 77 K is considered, which corresponds to cryogenic conditions and has been used in experiments of Au-BDT-Au junctions.[16] The same twenty ruptured NW tips are employed for both temperatures, with 210 simulations

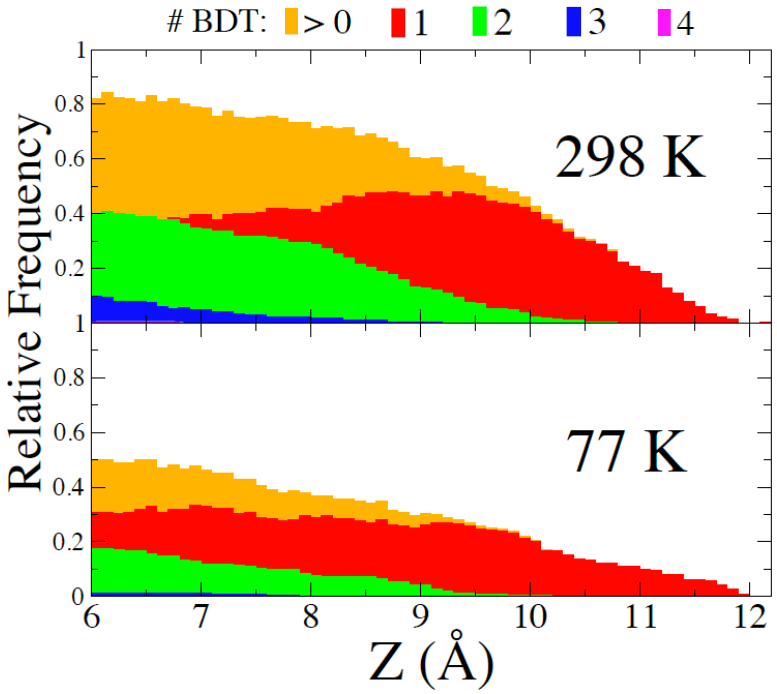

Figure 5.11. 298-K and 77-K histograms of the number of bridged molecules at various values of Z.

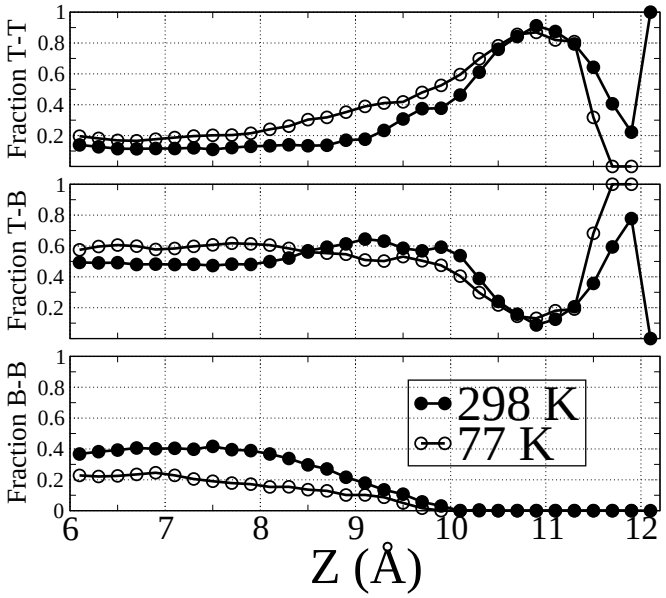

Figure 5.12. The bonding geometry for bridged BDT molecules plotted against Z at 298 and 77 K. See the caption in Figure 5.6 for definitions of the abbreviated terms.

performed in each case. Figure 5.11 shows histograms of the number of bridged molecules as a function of Z, at 298 and 77 K. Clearly, 298 K results in a significantly higher probability of forming a molecular junction composed of any number of molecules, for a majority of Z; thus, the reduced mobility of the BDT molecules at 77 K is detrimental to molecular bridging. The influence of temperature is further examined by plotting the bonding geometry and tilt angle in Figures 5.12 and 5.13, respectively. Overall, the quantitative differences between the two temperatures are small. In 5.12, the fraction of on-top sites binding a bridged molecule is slightly higher at 77 K and low Z. This is attributed to the migratation of BDT off of on-top sites after bridging there at large Z. This explanation is corroborated by data in 5.13, which displays higher tilt angles at 77 K than 298 K, indicating that confinement of bridged molecules to the tip apex takes place more often at the lower temperature.

No experimental data has been reported comparing the number, bonding geometry, or tilt angle of bridged molecules at different temperatures. Studies on temperature-dependent behavior have focused on other properties such as mechanical stability[16] and conductance.[138,202] MCBJ studies of Au-BDT-Au junctions at 77 K[16] and 4.2 K[22] have shown discernible peaks in histograms of conductance, but in neither case was an analysis of the relative peak heights at different temperatures reported. At 77 K, Tsutsui and co-workers[16] observed a peak in the BDT conductance histogram at $0.011G_0$, matching the reported value at 298 K;[11,23] this finding not only implies that coherent tunneling remains the dominant electron transport mechanism in the temperature range, but also that the most frequently occurring structures at 77 K and 298 K are similar.

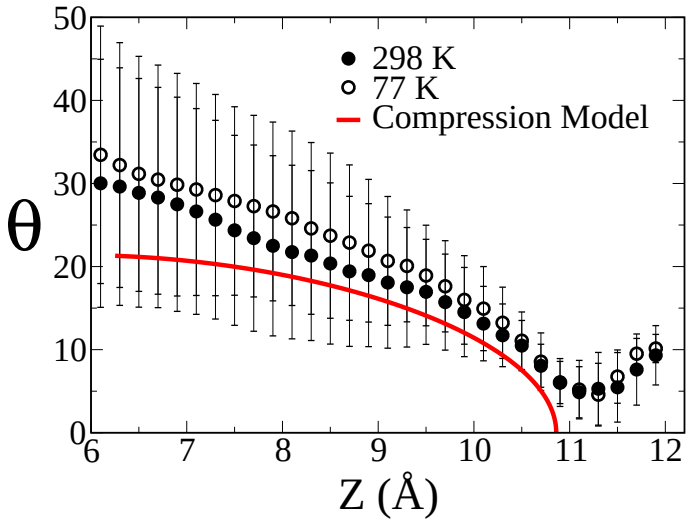

Figure 5.13. The tilt angle, θ, as a function of Z at 298 and 77 K.

The results in Figures 5.12 and 5.13 support this conclusion, especially for high Z, as the bonding geometry and tilt angle are very similar at the two temperatures.

5.5 Discussion

Though the precise causes are not fully understood, it is generally agreed that the environmental factors of a given experimental setup affect the conductance through a molecule. The conductance of a bridged molecule diluted in a monolayer of non-bridging adsorbate molecules has been shown to change when different adsorbate molecules are employed;[35] this result was explained by changes in the relative surface coverage for different adsorbates, which can alter the electrode work function. Building from this body of work, the results presented in this chapter suggest that changes in the electrode work function may not be the only factor affecting conductance, as the bonding geometry and tilt angle of bridged molecules are both influenced by monolayer density. In particular, monolayer density influences whether a molecule is able to sample the specific geometries required for bridging while also affecting the availability of preferred adsorption sites. The detailed atomic structure of the electrodes also influences the availability of bonding sites. Note that electrode geometry and bonding geometry have been linked previously.[51] Haiss *et al*.[51] performed measurements of single-molecule conductance using four different experimental techniques, with each method producing different relative populations of the conductance histogram peaks. The authors ascribed this behavior to changes in the electrode configuration between methods, which affected the most probable bonding geometries. This chapter's results also indicate that electrode geometry affects the most probable bonding geometries. While

ideal, atomically sharp tips predict a predominance of on-top/on-top bonding geometry at high Z, ruptured NW tips allow on-bridge bonding at high Z.

However, environmental factors do not greatly affect the properties of a junction in all cases. For instance, with BDT it may be reasonable to ignore certain environmental effects for inter-electrode separations of greater than $\sim$9.5 Å. In this regime, the tilt angle is similar regardless of the temperature and whether adsorbate molecules are present, and the probability of forming a multi-molecule junction is low; this makes $Z > 9.5$ Å well-suited for comparisons between experiment, theory, and simulation, since simplified treatments of the junction environment do not significantly affect the properties. On the other hand, for $Z < 9.5$ Å, tilt angle data diverge in cases where monolayer effects are ignored and the probability of forming multi-molecule junctions increases appreciably. In this regime, using simplified treatments for the junction environment may result in inaccurate predictions of structure, and thus give rise to incorrect conductance results. In this case it is necessary to perform environmentally resolved simulations to provide input or guidance for determining the most probable structures for theoretical calculations.

Although simulations performed in this chapter more closely resemble the MCBJ experimental technique than previous simulation studies, there are a few important differences compared to the experiments. The first difference is that unlike MCBJ experiments, the simulated electrodes are not contacted prior to forming each molecular junction. While molecular junctions often form immediately following NW rupture, for the purposes of gathering meaningful statistics and reducing computational expense, the spontaneous formation of molecular junctions without contacting the electrodes is simulated. In this respect, the junction formation process is more similar to that of the $I(s)$ and $I(t)$ experimental methods of Haiss and co-workers.[49–51] Note that contacting the electrodes may help overcome activation barriers involved in junction formation, especially at lower temperature, where the spontaneous formation of a molecular junction is less likely (see Figure 5.11).

Another important difference is that while in this chapter junction compression is simulated, in MCBJ experiments the conductance is typically monitored as a junction is elongated. This is an important difference considering the strength of the S-Au bond is high enough to pull short monatomic chains of Au atoms out of a surface during elongation,[120,203] and thus may result in different electrode structures than those used here. Despite not considering such effects, the compression of a junction prior to electrode contact is a fundamental aspect of the experiments that is likely to influence the structures emerging during elongation. Therefore, investigating the details of the compression process is essential to understanding the behavior of molecular junctions. Furthermore, for the results presented here, the structure of the Au tips is fixed during the compression/bridging portion of the simulation. This appears to be a reasonable assumption, as significant rearrangements of the tips were not observed during test calculations that allowed the tip structure to change

during compression/bridging. However, it is important to note that experiments typically span significantly longer timescales than accessible to simulation, thus atomic rearrangements of the Au tips may additionally be important.

Finally, the elongation rate may also play an important role. Here, simulations are performed with a fixed elongation rate of 1 m/s and temperature of 298 K. The rate of elongation will influence the resulting structural evolution of the wire, however, this effect will be much more significant at low temperature (*e.g.*, $\sim$4 K), in accordance with the universal energy release mechanism.[78,152] Moreover, in previous simulations of Au NWs elongated at 298 K in vacuum, significant differences were not observed in the spectrum of resulting tip geometries for rates ranging from 0.033 to 2 m/s, although subtle differences in the elongation pathway were observed.[152] 1 m/s is chosen for the present study as it is more computationally tractable for systems including BDT.

CHAPTER VI

CONDUCTANCE PROPERTIES OF AU-BDT-AU JUNCTIONS UNDER REALISTIC CONDITIONS

This chapter presents simulations of Au-BDT-Au junctions combined with high-fidelity conductance calculations. The junctions are simulated via mechanical elongation and/or thermal evolution, and snapshots are periodically extracted to calculate the conductance. This ensemble approach is representative of experiment and the junction structures are more realistic than prior theoretical work. First, the conductance evolution of Au-BDT-Au junction under elongation is calculated, with characteristic conductance curves emerging that depend on the structure of the junction. These results are used to explain a recent anomalous experimental finding.[43] This work is published in reference 74. Next, the conductance histograms of various junctions are computed. Structurally ideal and non-ideal junctions are considered, allowing for the effect of ideality in theoretical studies to be assessed. Additionally, simulations in which select portions of the junctions are frozen are performed to better understand the structural origins of conductance fluctuations through the junctions. These results provide important guidance to experimentalists developing strategies for controlling conductance fluctuations. This work is published in reference 75.

6.1 Introduction

The lack of reproducibility in the conductance through molecular transport junctions is a major barrier to the construction of reliable molecular-based circuitry.[10,102] Fluctuations arise from changes in the junction structure between successive junction rupture and reformation events or due to thermal motion.[204] Therefore, developing strategies for improving reproducibility and suppressing conductance fluctuations relies critically on understanding the structural origins of the experimentally observed conductance behavior. For instance, following a study[24] that showed that the conductance through biphenyl molecular wires depends on the dihedral angle between the phenyl rings, Kiguchi *et al.*[42] synthesized a rotaxane structure to limit changes in the dihedral angle, thereby suppressing the conductance fluctuations.

BDT is one molecule whose conductance behavior exhibits inconsistent behavior in experiment. Although BDT has been widely studied over the years for applications in molecular electronics,[4,6,17,22,23,43,65–67,73,82,205] recent discoveries[4,22,43] of its tunable conductance properties have generated a renewed interest in the molecule. These discoveries include counterintuitive conductance increases (exceeding an order of magnitude) during elongation of a Au-BDT-Au junction,[43] and a wide conductance window spanning three orders of magnitude.[22] The tunability of BDT's conductance is enabled by the proximity of its highest occupied molecular orbital (HOMO) to the Au electrode Fermi level (ε_F). Relatively small increases in the HOMO level result

in resonant (or near resonant) tunneling, which, as demonstrated by Bruot *et al*.[43] can be achieved through mechanical elongation of a Au-BDT-Au junction. However, elongation does not guarantee increases in conductance, as evidenced by numerous previous Au-BDT-Au studies[6,22,23] where conductance increases were not reported. The reason for this discrepancy is that the exact location of the HOMO level depends on the structural evolution of a junction, which may be influenced by the experimental setup and/or conditions. In order to make use of the desirable properties of BDT, and to facilitate experimental reproducibility, it is essential to determine the structure(s) responsible for increasing conductance.

Understanding the atomic-level origins of thermally induced conductance fluctuations is also important in Au-BDT-Au junctions. For BDT, conductance fluctuations are typically attributed to changes in the metal-molecule contact geometry (bonding site and tilt angle).[11,22,50] However, the electrode geometry may play an increasingly important role for systems involving mechanical elongation and deformation of the junction.[10,11,16,21–24,26,40,42,43,47,204] For example, Au-thiolate bonding results in significant deformation of the electrodes in break junction experiments. Several groups[21,40,47] have recently investigated the role of Au-thiolate bonding in break-junction environments, but the exact structural origins of the conductance behavior remains unclear.

Prior computational work[65–68,71,205] has thus far provided considerable insight into the behavior of BDT and the underlying mechanisms that control conductance. However, most prior computational studies of molecular junctions have adopted simplifications that may ultimately make it difficult to connect the predicted behavior with experiment. For instance, in typical computational studies of BDT, the molecule is sandwiched between ideal, planar surfaces with an arbitrary initial geometry, and then stretched via geometry optimizations.[66,67,205] This approach may not adequately capture many important aspects found in experiment, such as temperature effects, elongation rate effects, and non-ideal tip geometry. In order to better connect theory to experiment and facilitate a deeper understanding of the structure-conductance relationship, a different computational approach is needed that can capture these environmental effects and the stochastic nature of junction formation.

6.2 Simulation Details

Simulations of Au-BDT-Au junctions are performed using the hybrid MD-MC technique described in subsection 3.2.3. An example of a Au-BDT-Au junction elongation simulation procedure is illustrated in Figure 6.1 and involves trapping a single BDT molecule between ruptured Au nanowire tips by mechanical deforming a BDT coated nanowire; once a BDT connects between two tips, the junction is evolved via mechanical elongation at finite temperature (77 K), and the atomic coordinates are periodically extracted for use as input to electron transport calculations. This simulation procedure closely models the widely used me-

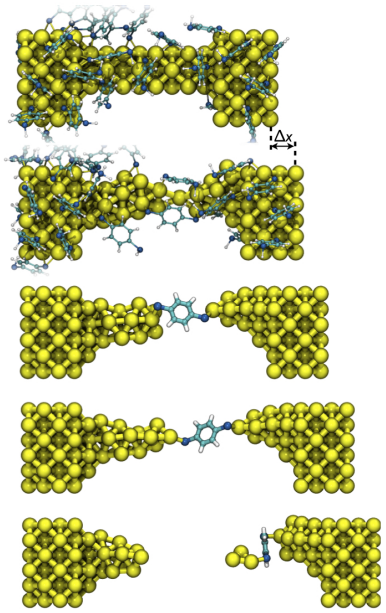

Figure 6.1. Simulation snapshots of the elongation of a BDT-coated Au nanowire, leading to the formation, elongation, and eventual rupture of a Au-BDT-Au junction. From top to bottom, Δx = 0.0, 4.0, 8.0, 12.0, and 16.0 Å. Monolayer molecules are removed after junction formation to isolate electrode geometry effects.

chanically controllable break-junction experimental method[6,22,43] and thus should produce experimentally representative configurations. Additionally, this procedure enables the efficient collection of a more statistically relevant number of configurations than typically used in quantum mechanical simulations, allowing for the assessment of ensemble behavior; specifically in this work, 104 independent simulations are performed to model break junction experiments, whereas recent quantum mechanical studies[65–67,205] considered only at most four structurally distinct junctions. The geometries predicted by our simulations should better represent break-junction experiments than previous computational work[65–67,205] due to the inclusion of (1) realistic electrodes, (2) finite temperature effects, (3) better statistics, and (4) junctions that are less biased by starting configuration.

The MD-MC simulations are initialized with a small Au NW (eight atoms long and three atoms thick) connected between two rigid [100]-oriented leads (four atoms long and six atoms thick). A monolayer of BDT (consisting of 30-36 chemisorbed molecules) is placed onto the NW by performing MC moves in the semigrand canonical ensemble. The non-adsorbed BDT are next removed from the simulation box and 20 million constant-NVT (where N is the number of BDT molecules, V is the volume, and T is the temperature) moves are performed to equilibrate the monolayer. Stretching of the BDT-coated wire is carried out by displacing the right-side lead layers in 0.1 Å intervals in the [100] direction, with 20 ps of MD and 100,000 MC moves at constant NVT applied between intervals. The stretching procedure is repeated until the rupture

of the Au NW occurs, at which point individual BDT molecules may chemically attach between the ruptured tips. In runs where a molecular junction forms, the junction is further elongated to the point of rupture. To isolate electrode structure effects, all remaining BDT molecules are removed from the simulation once a molecular junction forms. During the Au-BDT-Au stretching process, geometries are periodically (every $\sim$0.5-1.0 Å of elongation and immediately prior to rupture) extracted for use in conductance calculations. During MD, the velocity Verlet algorithm in combination with the rRESPA multiple time scale integrator is used to integrate the equations of motion, with outer and inner loop timesteps of 2.0 fs and 0.4 fs, respectively. A simulation temperature of 77 K is chosen because TB-SMA performs better at low temperature,[130] and also because 77 K is commonly used in experiments.[16]

To evaluate thermally induced conductance fluctuations in Au-BDT-Au junctions, further simulations are performed in which junctions are allowed to thermally evolve without stretching; snapshots are periodically extracted from the simulations and then used as input in electron transport calculations. 200 cycles of MD-MC sampling are performed, where a cycle consists of 0.2 ns of MD followed by 200,000 MC moves; at the end of each cycle, the conductance is computed. Previous studies[68,71] of this kind focused on ideal geometries with a single molecule sandwiched between two flat surfaces. Here, junctions are extracted from Au-BDT-Au elongation simulations, and therefore should be more representative of those likely to appear in widely used break-junction experiments.[10,11,16,22–24,26,40,42,43,47,204] In addition to simulations where all atoms are dynamic, two separate simulations are performed (from the same starting point) for each junction where either the BDT geometry or Au geometry is fixed. The BDT geometry (*i.e.*, intramolecular geometry and Au-BDT contact geometry) is fixed by treating the molecule (including the Au atoms covalently linked to the BDT) as a rigid body. In separate simulations, the positions of the Au atoms are fixed while the BDT is free to move. By eliminating specific degrees of freedom within our simulations, the independent contributions of changes in the Au and BDT geometries to the conductance fluctuations are determined.

6.3 Au-BDT-Au Junctions Under Elongation

6.3.1 Formation of Au-BDT-Au Junctions

In the break-junction simulations, a BDT molecule attaches between two ruptured nanowire tips in 31 out of 104 (30%) independent runs, in excellent agreement with values reported in Au/BDT break junction experiments (30-40%).[23] Akin to the experimental situation, the formation of a molecular junction is dictated by the proximity of adsorbed BDT molecules to the nanowire fracture location, and the availability of bonding sites on the Au tip(s). The geometry of a Au tip depends on the structural pathway of the nanowire during the elongation process, and hence can vary substantially between runs.[72,78,125,130,206] Thus, a large number of junction geometries are possible, which should better represent experiment than prior computational studies.

6.3.2 Conductance Evolution of Elongating Au-BDT-Au Junctions

Figure 6.2 plots the conductance evolution of eight representative Au-BDT-Au junctions under elongation. Distinct differences in the shape of the conductance traces are apparent in Figure 6.2; for clarity of presentation, similar traces are grouped into two separate plots shown in Figure 6.2a and Figure 6.2f. The curves in Figure 6.2 undergo large gradual increases, while the curves in Figure 6.2e are relatively flat; note that both behaviors closely match recent experimental results[43] and that previous idealized computational studies have failed to capture this range of behaviors.[66,67] Furthermore, these results demonstrate that increases in conductance depend on structure and are not a natural consequence of the increasing potential energy of a junction. The shifting of the highest occupied molecular orbital into alignment with ε_F is not necessarily a natural consequence of the increasing total potential energy of the Au-BDT-Au junction during elongation. Figure 6.3 plots the total potential energy and conductance of of a junction during elongation. The energy increases throughout elongation, up to the point of rupture at an elongation length of 6.6 Å. Although the potential energy increases, the conductance remains relatively flat throughout elongation, demonstrating that the structure connected to the BDT molecule is an important determinant of the conductance.

Interestingly, the breaking geometries shown in Figure 6.2b-e all contain a monatomic chain (MAC) of Au atoms directly connected to BDT. Of the 31 simulations resulting in molecular junction formation, 13% go on to form direct MAC-BDT connections during elongation. Each MAC-containing geometry in Figure

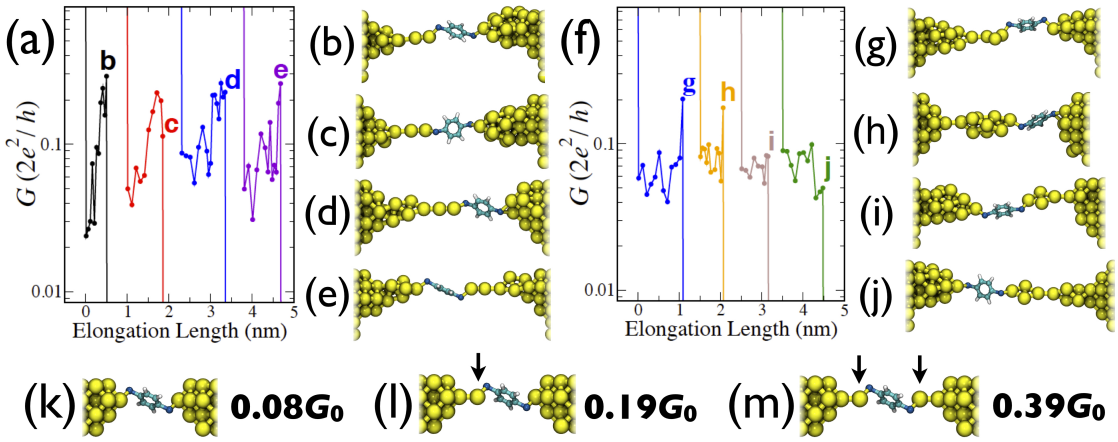

Figure 6.2. Conductance behavior of Au-BDT-Au junctions undergoing elongation. (a) Four gradually increasing conductance traces, with the corresponding geometries immediately prior to junction rupture shown to the right. The individual traces are offset along the x-axis for clarity. At a distance of 0.1 Å prior to junction formation the conductance is assumed to be $1G_0$ while at rupture the conductance is set to $0G_0$. (f) Four relatively flat conductance traces, with the corresponding break geometries shown to the right. (k-m) The effect on conductance of manually connecting Au MACs (indicated with arrows) to BDT. The BDT is initially connected between two ideal Au(100) tips.

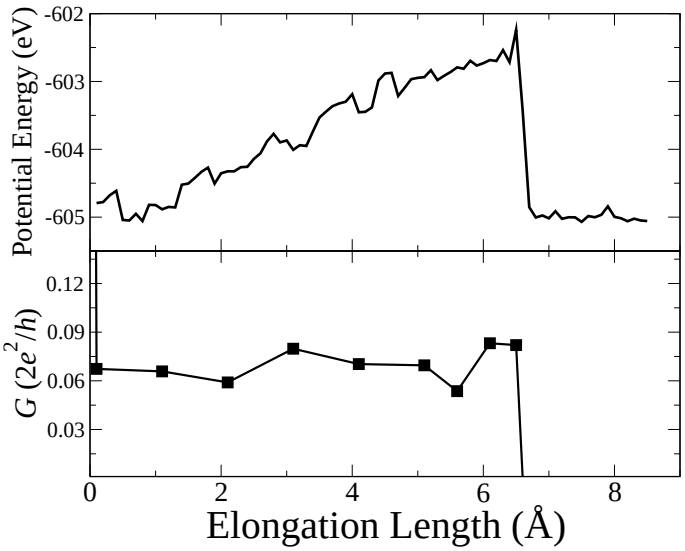

Figure 6.3. Evolution of the (top) total potential energy and (bottom) conductance of an elongating Au-BDT-Au junction.

6.2b-e results in conductance $> 0.2G_0$. Closer examination of the entire stretching trajectories reveals that the initial jumps to conductance values larger than $0.1G_0$ coincide with the appearance of a MAC at a BDT-Au interface, suggesting that the BDT-MAC connection is responsible for the increased conductance. To test this, MACs are manually inserted (the MAC Au-Au bond length is set to 2.60 Å [207]) at the BDT-Au interface of an ideal junction, as shown in Figure 6.2k-m, finding that conductance increases as MACs are inserted into otherwise static geometries.

6.3.2.1 Electronic Structure of Monatomic Chains Connected to BDT

Analysis of the electronic structure of the simulated junctions reveals that MACs broadly (+/- 1 eV) enhance the projected density of states (PDOS; see Figure 6.4) around ε_F for the MAC Au s and p_z states, thus inducing a stronger coupling of the molecular states around ε_F with the Au electrodes, resulting in a higher transmission. Importantly, this enhancement only occurs when BDT is bonded to a Au atom that bonds with one other Au atom; adatoms or atomically sharp tips (Figure 6.2k) do not result in this enhancement (see Figure 6.4).

In Figure 6.5 a MAC is first inserted at the left tip, then at the left and right tips. The transmission for the original benchmark (100) tip geometry is shown for comparison. Figure 6.4 presents the projected density of states (PDOS) for the atoms and orbitals involved in the BDT-Au bond in Figure 6.5. There are clear distinctions between the PDOS for a MAC electrode and a simple tip/adatom electrode. With a MAC present,

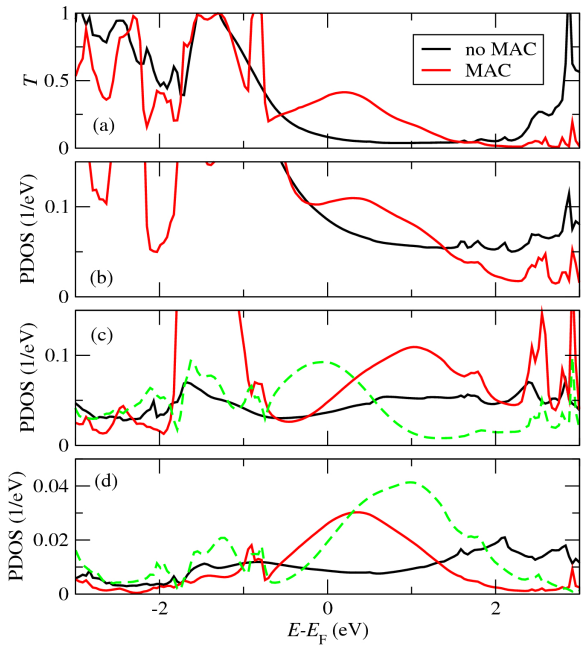

Figure 6.4. Transmission and PDOS for the junctions shown in the top (no MAC) and bottom (two ideal MACs) images of Figure 6.5. (a) Transmission; (b) PDOS for left S atom; (c) PDOS for *s* orbital of Au atom attached to the left S atom; (d) PDOS for p_z orbital of Au atom attached to the left S atom. The green dashed curves in (c) and (d) show the same PDOS, but for the MAC atom in the left electrode not directly connected to BDT.

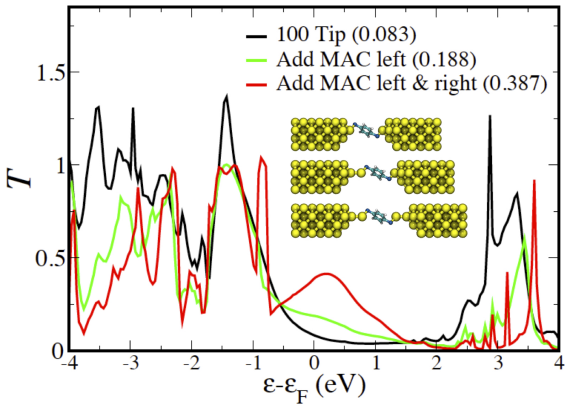

Figure 6.5. The effect on transmission of adding MACs to Au(100) tips.

the PDOS is enhanced around ε_F for the S atom connected to a MAC, and also for the Au MAC atoms. In the case of Au, the *s* and p_z orbitals dominate the transport and their PDOS is oscillatory compared to the relatively constant PDOS for Au atoms in absence of a MAC. The enhanced PDOS arises from smaller band dispersion in a Au MAC compared to bulk Au. The magnitude and shape of the enhancement depends on various factors, mainly the length of the MAC, but also the S-Au bonding and the remaining junction structure.

Note that in the simulated junctions a MAC forms on only one side of the molecule, and thus the transmission resembles the single-MAC junction in Figure 6.5 (green curve). Figure 6.5 shows that higher conductance results from the formation of a MAC on both sides of a junction, however this scenario does not occur in our simulations as the internal stress of the junction is relieved primarily through rearrangements (and eventually rupture) in the MAC electrode. In other words, the structure in the non-MAC electrode remains roughly unchanged following MAC formation.

6.3.2.2 Thermal Stability of Au Monatomic Chains Connected to BDT

In contrast to MACs, other low-coordination electrode structures such as Au-Au_2-Au units (see Figure 6.2i,j) do not increase conductance (note that Au-Au_2-Au structures have been previously observed in DFT-based studies of Au tips[206,208]). Meanwhile, the structures in Figure 6.2g,h result in high conductance, but their lifetimes are extremely short; in non-stretching MD simulations the structures shown in Figure 6.2g,h remain stable for less than 1.0 ns, which is a time scale that is too short to be measured in experiment. On the other hand, three of the four MACs in Figure 6.2b-e remain stable for the complete duration of a 1.0-μs simulation without stretching (the actual simulated junctions are taken 0.2-0.5 Å of elongation prior to the rupture structures shown in Figure 6.2b-e), indicating that MACs may possess sufficient stability to be detected in experiments performed at 77 K.

Note that MACs have been observed in experiments[123,125,209] and in simulations[78,125,206] of elongating Au nanowires without BDT. MACs have also been observed in simulations of thiolate-terminated molecules being pulled away from step edges on Au surfaces[120] and in simulations of Au-alkanedithiolate-Au junctions.[64] Thus, the appearance of MACs in Au/BDT break junction experiments is not without precedent and their formation is not an artifact of the applied simulation model. However, the significant impact of MACs on molecular conductance has not been previously demonstrated.

6.3.2.3 Conductance Histograms of Au Monatomic Chains Connected to BDT

To confirm that the conductance increases are not the result of the limited time scale of the simulations, the conductance distributions are calculated for three structurally distinct Au-BDT-Au junctions evolved at 77 K without stretching the junction. Figure 6.6 shows that the conductance of BDT connected to a MAC is statistically distinct from the two other deformed junctions with almost no overlap between the histograms, indicating that the increases seen in Figure 6.2a are indeed associated with their own unique structural motif and not simply a short-lived or improbable configuration. Additionally, the conductance fluctuations for BDT connected to a Au MAC is approximately double that of the other structures. Increased fluctuations in BDT-MAC geometries have been reported previously,[60] albeit for unrealistic, manually adjusted geometries,

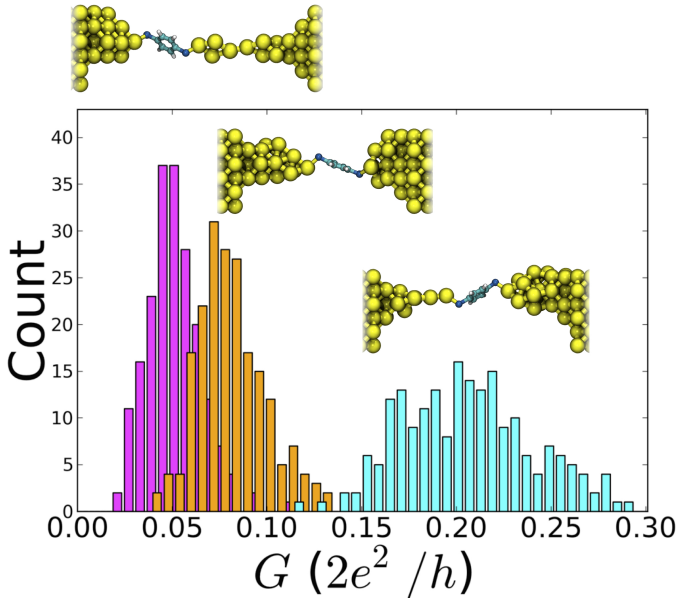

Figure 6.6. Conductance histograms of three thermally evolving Au-BDT-Au junctions. The bin width is $0.006G_0$. Standard deviations of the histograms (from left to right) are $0.014G_0$, $0.018G_0$, and $0.034G_0$.

making it difficult to assess their connection to experiment. Also note that the histograms in Figure 6.6 are similar to those in experiments by Tsutsui *et al.*,[11] where a high-conductance state at $0.1G_0$ exhibited a larger peak width than the peak at lower values ($0.01G_0$).

6.3.3 Discussion

The similarities between these results and the experiments of Bruot *et al.*[43] suggest that MAC formation is the likely cause of the large (factor of five or more) gradual increases in conductance observed in these experiments. The lack of large conductance increases in experiments performed at 300 K[43] suggests that the structural motif responsible for increased conductance has a distinct thermal dependence (*i.e.*, the structure is unstable at higher temperature). It has been previously[78] established that the formation of MACs in mechanically deformed Au nanowires will depend on temperature, where MACs form with the highest frequency and stability at low temperature. This is confirmed by performing 298-K simulations without stretching of the MAC geometries in Figure **??**b-e (the actual simulated junctions were taken 0.2-0.5 Å of elongation prior to the rupture structures shown in Figure 6.2b-e). In all four cases the junction undergoes thermoactivated spontaneous breakdown in less than 1.0 ns, indicating that MACs are not stable at high temperature. Thus, the thermal instability of MACs explains why large conductance increases were not observed in 300-K experiments.[43] While in the work of Bruot *et al.*[43] there were no large conductance increases at 300 K, large conductance values were reported in the 300-K conductance histogram, which may have been caused by other

significant conformational changes to the junction at 300 K.

Other factors, such as Au adatoms and strained S-Au bonds, have been shown[66,67,205,210] to increase conductance in idealized junctions, and may also play a role under certain conditions. For instance, adatom formation may be important in STM-BJ experiments[23] where a planar surface serves as one of the electrodes. Meanwhile, the small ($\sim 0.001 G_0$) reversible changes in conductance (with respect to junction compression and elongation) in the work of Bruot *et al*.[43] are likely caused by reversible structural change such as a strained S-Au bond. On-hollow bonding geometry,[11,22] high tilt angles,[22,50] and S atoms embedded in Au contacts[40] have all been proposed to explain large values of conductance, but these explanations do not seem likely given the very large, gradual conductance increases observed in the recent work of Bruot *et al*.[43] or the present study. Also note that since the elongated junctions are under tension, it makes it more probable for BDT to adopt an upright geometry with low tilt angle, bonded with a single Au atom at each electrode.

The lack of MAC formation in prior theoretical work focusing on flat plates[65–67,205] may have been caused by electrode geometry choice (*i.e*., flat surfaces). Flat surfaces may discriminate against the formation of MACs since the *dynamic structural fluxionality* (*i.e*., lengthening and weakening of Au-Au bonds) of flat Au surfaces is lower than that of nanostructured Au surfaces.[95] The use of DFT-based geometry optimizations,[66,67] where elongation rate and temperature effects are neglected, may also explain the absence of MACs in prior work, since the appearance of MACs has been linked to both the elongation rate and temperature.[78]

6.4 Thermally Evolving Au-BDT-Au Junctions

6.4.1 Conductance Fluctuations in Au-BDT-Au Junctions

Figure 6.6 reveals interesting differences between the conductance fluctuation behavior through structurally distinct, thermally evolving junctions. To further investigate such differences, conductance fluctuations are computed for junctions with different degrees of structural ideality. Figure 6.7 compares the conductance histograms for the three junctions and three simulation types. The fully dynamic simulation results, which reveal important differences between the ideal and non-ideal junctions, are first considered. The ideal junction (junction 1) produces conductance histograms that are much narrower than those for the non-ideal junctions (junctions 2 and 3). The peak width (standard deviation, σ) is more than an order of magnitude lower than the average conductance for the ideal junction, while for the non-ideal junctions the peak width is on the same order of magnitude as the conductance values themselves. The large peak widths in the non-ideal junctions result from increased geometric freedom, and may present challenges for applications where a device is required to maintain a target conductance value within some threshold. The shape of the conductance histogram also changes for the non-ideal junctions. While the distribution for the ideal junction

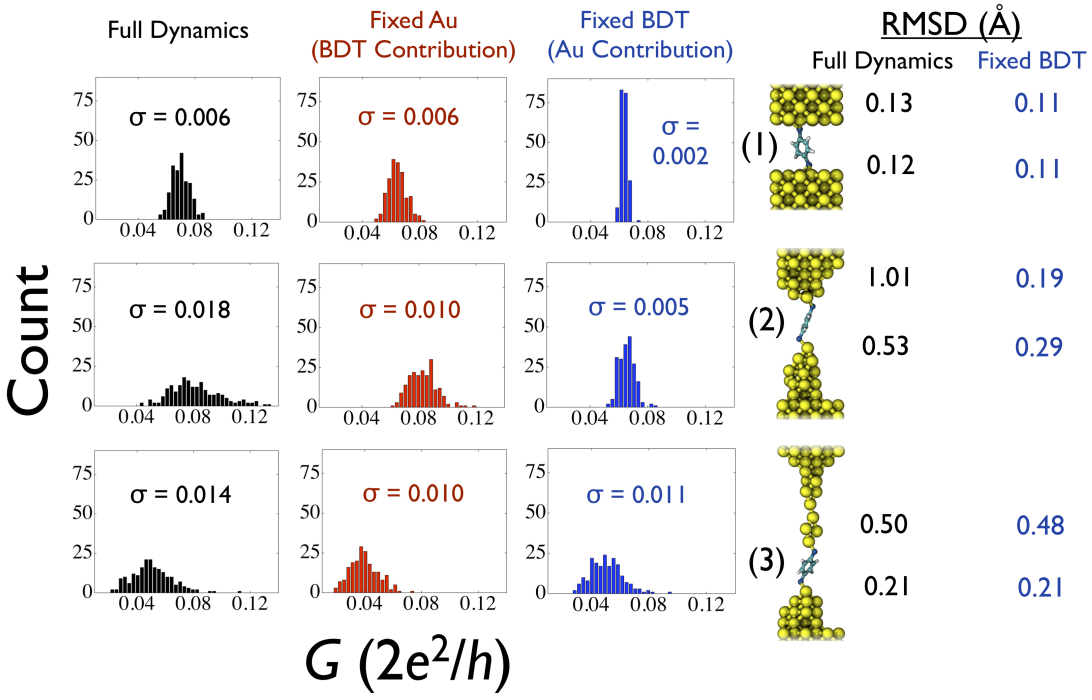

Figure 6.7. Calculated conductance histograms. (Top row) Ideal, flat-surface junction, (middle row) a junction with curved tips, and (bottom row) a highly deformed junction. For each junction, three separate simulations are run: (left column of plots) one where all atoms in the junction are dynamic, (middle column of plots) one with the Au atomic positions fixed, and (right column of plots) one with fixed BDT geometry. The standard deviation, σ, is shown with each histogram, and the RMSD of the Au atom bonded with BDT in each tip is shown on the far right.

appears Gaussian (as expected for nonresonant tunneling through molecules[211]), results for the non-ideal junctions exhibit long tails spanning conductance values much higher than the peak values. This results from a transition in the electron transport mechanism from far off resonance in ideal junctions to off resonance in non-ideal junctions.

6.4.1.1 The Role of Electrode Motion

It is apparent from the relative peak widths in the fixed BDT results that the role of the electrodes becomes increasingly important as the electrodes are deformed. For the ideal junction, the Au atoms are closely bound to their lattice sites and thus do not contribute significantly to the conductance fluctuations. In fact, the fully dynamic peak width is completely resolved in the fixed Au simulation, indicating that the conductance fluctuations are dominated by the ability of BDT to explore configuration space. The situation changes for junction 2, as the fully dynamic peak width is not completely resolved from the fixed Au simulation. This suggests that the motion of the electrodes facilitates the sampling of a greater range of contact geometries.

For junction 3, the peak widths are similar for the three types of simulations, albeit slightly wider for the fully dynamic simulation, which demonstrates the importance of the interplay between Au and BDT geometry in these systems; that is, changes in the BDT geometry are often enabled by changes in the electrode geometry, and vice versa. Importantly, the peak width in the fixed BDT simulation is larger than that for the fixed Au simulation, indicating a transition in the primary origin of conductance fluctuations from changes in the molecule geometry to changes in the Au geometry. This transition is attributed to the enhanced *dynamic structural fluxionality*[95] (lengthening and weakening of Au-Au bonds) in the top tip of junction 3. To support this explanation, the root-mean-square deviation (RMSD) of the position of the Au atom bonded to BDT relative to its average position is calculated. In cases where multiple Au atoms are bonded to BDT, the Au atom that is on average closest to the bonded S atom is considered. As shown in Figure 1, the peak widths scale with the RMSD magnitude. With the BDT geometry fixed, the top tip in junction 3 exhibits the highest RMSD due to its low coordination. In the fully dynamic simulations, junction 2 produces the highest RMSD, which is consistent with its large spread in conductance. The high RMSD results from electrode rearrangements, contributing to the mobility beyond simple fluctuations about a single position.

6.4.1.2 The Role of Molecular Tilt Angle

The sampled molecular tilt angles also changes between the different junction geometries. However, increases in the range of sampled tilt angles do not increase conductance fluctuations significantly. Figure 6.8 plots histograms of the tilt angle (angle between the S-S vector and z-axis) during the fixed Au simulations. Note that the distribution is much wider in junction 3 where the molecule can more easily rotate around the "sharp" upper tip. It has been shown that in junctions where the electrodes are represented as flat surfaces, the conductance is sensitive to the tilt angle at values greater than 20°.[50] It is therefore surprising that the increased tilting freedom of the BDT molecule in junction 3 results in conductance fluctuations that are slightly smaller than those resulting from the fixed BDT simulation. In the case of sharp tips, the strong relationship between tilt angle and conductance may not apply since the interactions between the molecule and electrode(s) are limited by the small number of metal atoms in the vicinity of the metal-molecule bond(s). In different environments (*e.g.*, higher tilt angles and relatively flat tips) where the carbon atoms in BDT can interact with the Au tips, the range in sampled tilt angles may make more significant contributions to the conductance fluctuations.

6.4.1.3 Conductance Fluctuations in Elongating Junctions

An important consideration in molecular break-junction experiments is how the conductance fluctuations change as a junction is elongated. Thus, conductance fluctuations in a junction undergoing mechanical elon-

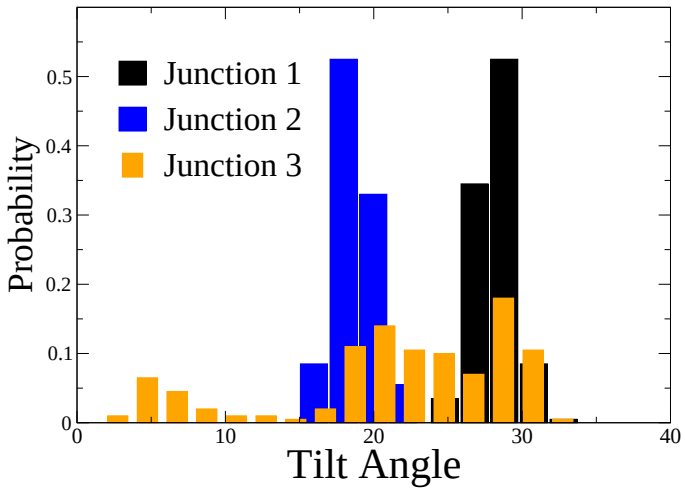

Figure 6.8. Tilt angle (°) distribution during the fixed Au simulations.

gation are next explored. The average conductance and standard deviation at each elongation length are presented in Figure 6.9, along with the RMSD value of the BDT-bonded Au atom in each tip during the MD-MC simulation; the conductance from the initial geometry at each elongation length is also plotted for comparison. The error bar sizes in Figure 6.9 strongly indicate that mechanical deformation of the junction increases the conductance fluctuations, as the error bars at the early stages 0.0 and 0.5 Å are very small, before increasing significantly at 1 Å. This behavior is dictated by high-mobility structures that form in response to mechanical elongation; that is, the tips become less ideal as the junction is deformed. The fluctuations and RMSD are largest at elongation lengths of 1.0 and 2.0 Å, where significant structural rearrangements of the electrodes occur during the simulation. Figure 6.9 also highlights the importance of considering more than a single geometry when calculating conductance, especially for systems where the relative changes in conductance are small between the various structures. It is clear that the single-geometry data fails to capture the average behavior over the entire range. Additionally, Figure 6.9 illustrates the difficulty in identifying junction structure based on experimental conductance histograms, as different junction structures may have similar average conductance values and highly overlapping distributions.

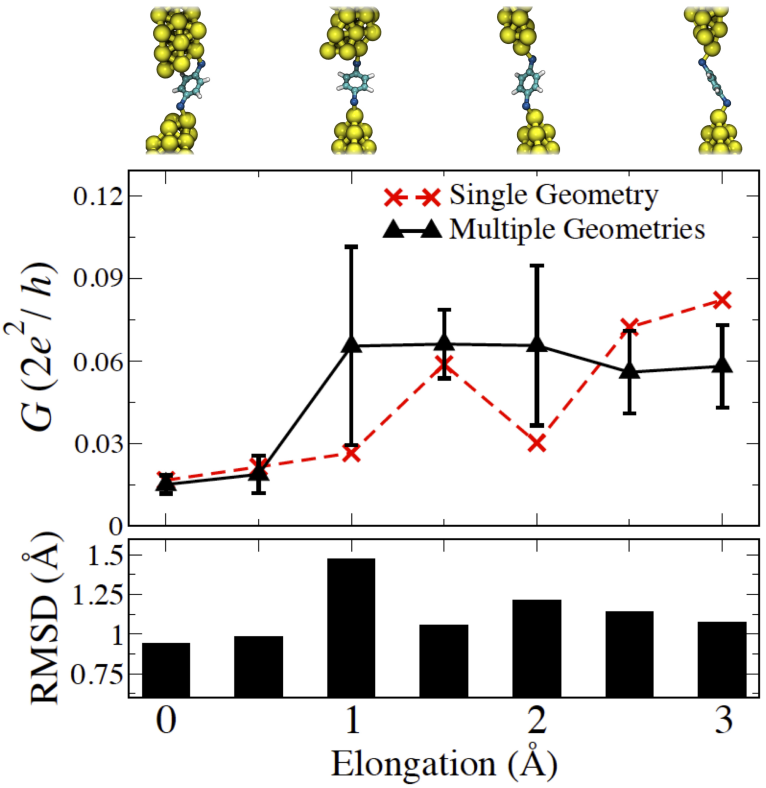

Figure 6.9. (Top) Thermally averaged and single-geometry conductance trace for Au-BDT-Au junction undergoing elongation. The initial junction geometries are shown above for every Å of elongation. (Bottom) Plot showing the average RMSD of the Au atom bonded to BDT.

CHAPTER VII

SIMULATIONS OF GOLD NANOWIRE ELONGATION IN VACUUM VIA GPU COMPUTING

In this chapter, the failure mechanism of Au NWs is investigated as a function of NW size and temperature. A large number of independent trajectories are analyzed to probe the ductile-to-brittle[88] transition, in which short NWs are predicted to fail by plastic deformation and long NWs are predicted to undergo brittle, catastrophic failure. Since the failure mechanism is intimately linked with post-rupture tip structure, this study is pertinent to single-molecule junctions, where the properties of the device are highly sensitive to the tip geometry.[51,73,212] In order to facilitate the simulation of a large number of independent trajectories, TB-SMA is ported to HOOMD-Blue, a MD package implemented on massively parallel graphics processing units (GPUs). The resulting speedup enables the simulation of over 2000 independent trajectories.

7.1 Introduction

Understanding the rupture process of elongating metallic NWs[131–134] under a range of conditions is important in areas such as nanoelectronics[58] and nanoscale cold welding,[135] where the properties and behavior are sensitive to the atomic level structure. For example, the deformation of a NW can significantly alter the electron transport properties of atomic-scale junctions.[130] Recently, Wu and co-workers[88] suggested a transition from ductile-to-brittle failure of mechanically deformed NWs as the NW length increases. The ductile regime, where virtually all previous simulation studies have focused,[72,77,78,125,130,175,179,181,182,213,214] exhibits a diverse set of structural evolution modes, which, while important for producing novel nanoscale structures such as monatomic chains,[72,122,123,125,175,179,182] helices,[72,175,214] and polytetrahedra,[130] may be undesirable in certain applications. In contrast, brittle failure is characterized by a sudden shearing of the wire that is more reproducible but less structurally diverse; this consistent structure may be important in studies of molecular electronics, as molecules are often bridged across the tips of a broken NW,[6] and it has been established that tip structure may strongly influence the transport properties of the bridged molecule.[51,73,212] Thus, adjusting the length of a NW may provide a method for controlling its structure and properties.

In order to facilitate reproducibility and improved control for device applications, it is important to understand the validity and scope of the ductile-to-brittle transition under a range of conditions. In their study, Wu *et al*.[88] focused on very large (from a computational cost standpoint) NWs, with diameters of 20 nm and lengths spanning from 188 to 1503 nm. However, different breaking behavior may occur for significantly thinner NWs, such as 1.8-nm core-shell[128] or 3-nm single crystalline[135] Au NWs fabricated in experiment, where the impact of surface energy is more prominent, stochastic atomic motion may play an increased role,

and classical dislocation plasticity may no longer apply. It also remains unclear what role temperature plays in the length-dependent mechanism. Moreover, due to the high computational cost of their simulations, Wu *et al.*[88] were limited to a single run for each NW size, and thus their results may not be representative of typical behavior since NW elongation and rupture is a stochastic process,[72,78,130] especially within the ductile regime. Dislocation events occurring in response to mechanical loading are highly sensitive to the relative positions of metal atoms; thus, slight differences in atoms' relative positions induced by thermal motion can cause vastly different structural pathways for two independent runs of a NW elongated under identical conditions. Thus, a follow-up study that considers a large number of independent trajectories for each state point would provide statistical insight into the NW elongation process and be valuable for clarifying the validity and scope of the ductile-to-brittle transition.

Running MD simulations on a graphics processing unit (GPU) provides an efficient means for running a large number of replicates in order to better describe the statistical behavior of NW rupture. HOOMD-Blue is a MD package built from the ground up with GPU computing in mind, and large performance boosts have been achieved with HOOMD-Blue relative to CPU-based simulations.[90] Early development of HOOMD-Blue emphasized basic MD functionality and interaction models. More recently, features that enable the simulation of hard-matter systems have been added, such as the embedded-atom method (EAM).[215] EAM is a many-body potential designed to capture metallic bonding interactions, with resulting performance gains on par with a pairwise potential. However, prior work[77] has shown that the EAM potential overestimates the surface energy, resulting in energetic and structural evolution that does not match quantum mechanical calculations. The second-moment approximation to the tight-binding (TB-SMA) potential is better suited for describing NW elongation.[77]

7.2 Simulation Details

Au NW elongation is simulated using the stretch-and-relax technique described in subsection 3.2.1. The gripping atoms on the left and right sides of the wire are periodically displaced by 0.05 Å in the [$\bar{1}$00] and [100] directions, respectively, between 20 ps of MD in the canonical ensemble (constant NVT). The equations of motion are integrated using the velocity Verlet algorithm with a time step of 2.0 fs. The NWs vary in their initial diameter, D_0, from 3.1-5.0 nm, while the initial length, L_0, is varied between 20-140 nm. The smallest NW is shown in Figure 7.1. Note that a small, ring-shaped notch is introduced in the center of the NW to control the break location. Each independent elongation simulation is initialized with a random Gaussian distribution of atomic velocities resulting in a temperature of 0.01 K. Prior to simulating elongation, we equilibrate the NW using the following method: (1) 100 ps of MD in the isobaric-isothermal ensemble (constant NPT) with a target pressure of zero in the [100] direction and a target temperature of 0.01 K; (2)

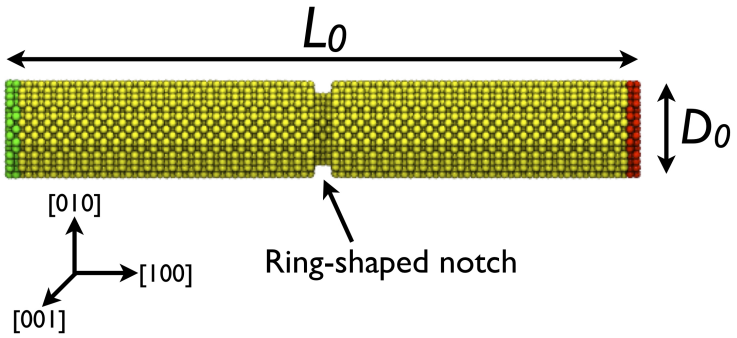

Figure 7.1. Schematic of an initial NW geometry. In this case, D_0 = 3.1 nm and L_0 = 20.4 nm. The ring-shaped notch is approximately three atoms wide and two atoms deep. The gripping atoms are colored in green and red, while dynamic atoms are colored yellow.

400 ps of MD in the canonical ensemble, ramping the temperature from 0.01 K to the target value; (3) 400 ps of MD in the canonical ensemble at the target temperature.

7.3 Hardware/Software Details

Benchmark simulations presented here were conducted on the National Science Foundation supported Keeneland Initial Delivery System (for GPU benchmarks) and the Carver cluster as part of the National Energy Research Scientific Computing Center (for CPU benchmarks); a full description of the compute nodes are given below.

7.3.1 HOOMD-Blue Simulations

Keeneland, hybrid CPU/GPGPU supercomputer at Georgia Tech University; Device: Tesla M2090, 1300 MHz, 512 cores, 6 GB GDDR5 RAM; Host: 2 x Eight-core Intel Xeon E5-2670 (Sandy Bridge), 2.6 GHz, 32 GB DDR3 RAM; OS: CentOS 6.2. Software: HOOMD-Blue version 0.9.2 compiled on the hybrid Keeneland CPU/GPGPU supercomputer at Georgia Tech with GCC 4.4.6 and NVCC 4.2.

7.3.2 LAMMPS Simulations

Carver, IBM iDataPlex cluster at National Energy Research Scientific Computing Center; 2 x Quad-core Intel Xeon E5550 (Nehalem), 2.67 GHz, 24 GB DDR3 RAM; OS: Red Hat 4.1.2; Software: LAMMPS version 21 March 2012, extended to include TB-SMA, compiled with Intel 12.1.3 and OpenMPI-Intel 1.4.5.

7.4 Performance of TB-SMA in HOOMD-Blue

The performance of the TB-SMA potential in HOOMD-Blue is first evaluated. For comparison, CPU-based simulations are performed in LAMMPS,[153] extended to include the TB-SMA potential. The LAMMPS

simulations are performed in parallel across 8, 16, or 32 CPU cores. The benchmark simulations consider unstretched Au NWs for 400 ps at 10 and 298 K. In all cases the CPU and GPU implementations of TB-SMA yield identical equilibrium results. For the best comparison, the CPU and GPU-based simulations are carefully tuned to obtain optimal performance. It is important to tune the CPU and GPU-based simulations separately since the algorithms they implement vary in their relative performance. A neighbor list buffer radius, r_{buff}, of 0.20 and 0.29 Å is used in LAMMPS and HOOMD-Blue, respectively. The neighbor list is rebuilt when the maximum atomic displacement since the last build exceeds $r_{buff}/2$. The larger r_{buff} value for the GPU reflects the relatively high cost of the neighbor list rebuild operation in HOOMD-Blue. Ensuring a uniform workload across each CPU core in LAMMPS is another important performance consideration. While HOOMD-Blue parallelizes the force computation by assigning each atom to a CUDA thread that is responsible for calculating the force on that atom, LAMMPS breaks up the workload by domain decomposition. In LAMMPS the best performance is obtained by decomposing the simulation box into equally sized domains along the [100] axis. No attempts are made to apply multi- or hyper-threading[215] to the LAMMPS simulations, which may yield a slight performance boost. Additionally, HOOMD-Blue was compiled using the GNU compiler suite (v4.4) and CUDA 4.1; LAMMPS was compiled using the Intel 13.0.1 compiler suite, as it was found to provide significant speed gains as compared to the GNU compiler suite on the Intel-based hardware.

A critical performance feature in HOOMD-Blue is the particle re-sort algorithm, which re-orders the particles in memory such that neighboring particles are nearby each other in memory, thereby improving cache coherency.[90] LAMMPS has a similar re-sorting algorithm but noticeable performance gains were not observed by adjusting the default parameters. The particle re-sorting algorithm in HOOMD-Blue periodically re-orders the particles on the Hilbert Curve,[216] improving performance drastically for liquid simulations in which particle diffusion is prominent. However, for NW simulations, where the relative positions of atoms change very little, particle re-sorts are unnecessary. In fact, optimal performance is obtained by setting the particle re-sorting frequency to a value above the total number of time steps in the simulation. An additional performance issue for the NW GPU simulations is the effect of the large void spaces in the simulation box surrounding the NW, which render the Hilbert Curve ineffective at determining the optimal particle order in memory. To address this, the Au atoms are initially ordered along the [100] axis of the NW (atoms in the same layer are, in turn, ordered randomly). This is the optimal initial ordering scheme of those tested; however, there may be an improved method that yields better performance.

Figure 7.2 shows the speedup for the single-GPU HOOMD-Blue simulations relative to the LAMMPS simulations run on 8, 16, or 32 CPU cores at 10 and 298 K. Comparing to 8-core GPU simulations, the TB-SMA GPU implementation yields speedups between 5 and 11, depending on the temperature. The improved

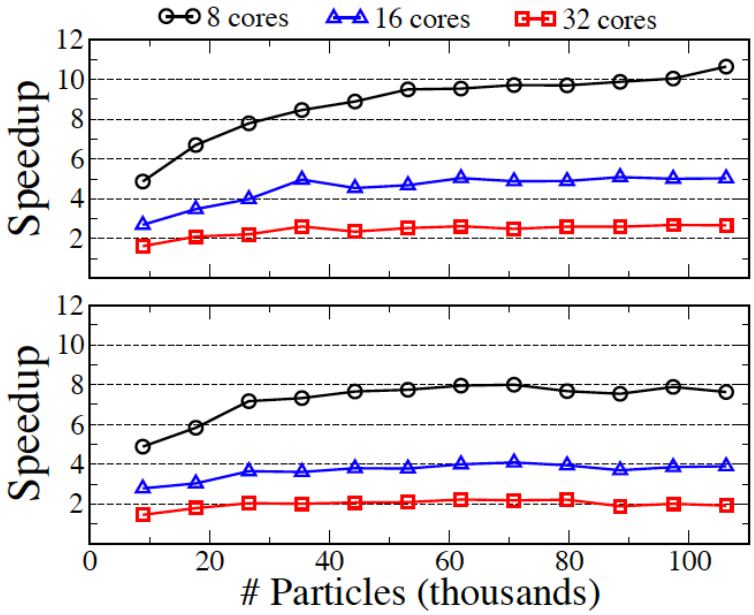

Figure 7.2. Performance speedup of TB-SMA in HOOMD-Blue running on a single GPU relative to the LAMMPS implementation run on 8, 16, or 32 CPU cores at (top) 10 K and (bottom) 298 K. Speedup is the ratio of the timesteps completed per second on a GPU to that on the CPU implementation.

performance at low temperature (10 K) results from the smaller number of neighbor list rebuilds brought about by the reduced atomic motion. As the CPU simulations are scaled to multiple nodes, the CPU performance approaches that of the GPU implementation. The scaling is approximately linear in the range of 8-32 cores, especially for the larger NWs. Additional benchmarks of the largest NW on 64 cores demonstrate speedups of $\sim$1.5 and $\sim$1.1 at 10 and 298 K, respectively, suggesting continued linear behavior. Thus, the HOOMD-Blue code on a single Nvidia M2090 GPU performs equally to 64-80 CPU cores on Carver. This outstanding performance gain enables the study of a large number of independent trajectories for mapping out the landscape of Au NW failure behavior. For example, Figure 7.2 indicates that in the time required to run 10 replicates of a $\sim$100,000-atom NW at 10 K on eight CPU cores, roughly 110 replicates could be run on a GPU. The ability to rapidly simulate NW elongation makes large-scale statistical studies more feasible.

Additional benchmarks on Carver using the GNU compiler suite scales the GPU to CPU scaleup by a factor of $\sim$1.2 compared to 7.2; consistent performance is obtained on various in-house resources. Other benchmarks using the Nvidia GTX 580 GPU on an in-house Intel Core-i7 based system show similar trends in terms of GPU to CPU scaleup shown in Figure 7.2, but scaled by a factor of approximately $\sim$0.75. Additionally, the GPU benchmarks did not show a significant dependence on the host architecture (*i.e.*, the CPU type and clock speed) when examining performance for identical cards on different systems. Also, for calculations using the GTX 580, the speedups at both temperatures are very similar to those obtained with a

GTX 480 for bulk Al and Cu crystals using EAM.[215] Thus, like EAM, porting TB-SMA to the GPU yields significant performance gains.

Note that elongation of a NW may change the relative performance of the CPU and GPU implementations of the TB-SMA potential. Tests indicate that performance on the GPU decreases during the initial stretching of the NW, due to increases in neighbor list sizes. Simulations on the CPU tend to behave consistently until significant necking of the NW has occurred, at which point the distribution of atoms in each processor's domain becomes uneven.

7.5 Statistical Evaluation of Failure Mode in Replicate MD Simulations

7.5.1 Stochastic Behavior in Nanowire Failure

The GPU implementation of TB-SMA is next applied to study the variance in failure behavior of elongating Au NWs. Figure 7.3 shows a typical stress-strain curve for a NW with D_0 = 3.1 nm and L_0 = 20.4 nm elongated at 10 K. The serrations in the stress-strain curve indicate discreet dislocation events characteristic of ductile failure. Wu *et al.*[88] defined a critical NW length, L_C, that predicts the mode of NW failure; initial NW lengths exceeding L_C undergo brittle failure, while initial lengths less than L_C result in ductile failure. L_C is given by

$$L_C = \frac{D_0}{\varepsilon_y} cot(\alpha), \tag{7.1}$$

where ε_y represents the yield strain and α is the angle between the direction of dislocation slipping and the direction of the tensile load. Han and co-workers[217] noted that α depends on whether deformation occurs via partial or perfect dislocation(s). For a [100]-oriented nanowire, $cot(\alpha)$ ranges from 1 for perfect-dislocation-mediated deformation to $\sqrt{2}$ for partial-dislocation-mediated deformation. Applying these values to 7.1 for a NW with D_0 = 3.1 nm and ε_y = 0.076, L_C falls between 40.8-57.7 nm. Thus, the NW in Figure 7.3, whose initial length of 20.4 nm is well below L_C, undergoes the failure mode (ductile) predicted by equation 7.1.

To investigate the role of stochastic events on the rupture process, a total of 380 simulations like the one in Figure 7.3 are next performed, with the only difference between replicates being the initial atomic velocity distribution. Figure 7.4 plots the stress-strain relationship for these 380 runs as a heat map, with bright areas corresponding to frequently occurring pathways. Prior to the yield point, the stress-strain pathway is very consistent between runs; however, after the yield point a region of diverse behavior emerges. This region is characterized by brightly colored diagonal streaks, which represent common stress-strain pathways and indicate the presence of plasticity. The streaks are faint at high values of strain as it becomes less likely for independent pathways to coincide. Finally, a bright horizontal area appears between strain values of ∼0.12-

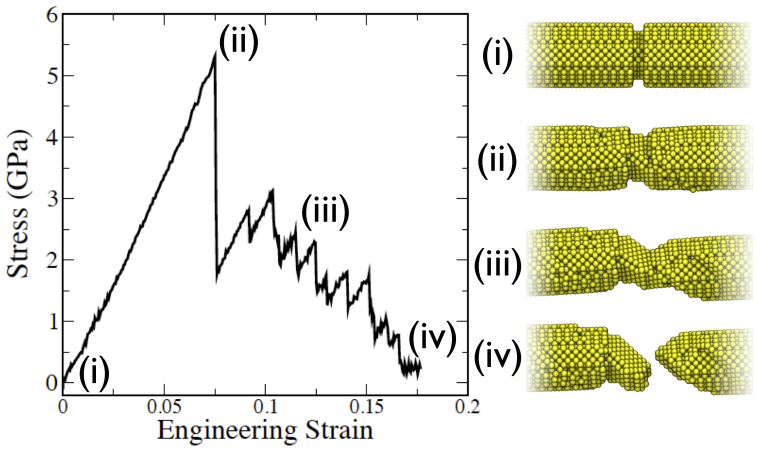

Figure 7.3. Stress-strain curve of an elongating Au NW (D_0 = 3.1 nm, L_0 = 20.4 nm), with zoomed-in images of the NW neck at select points.

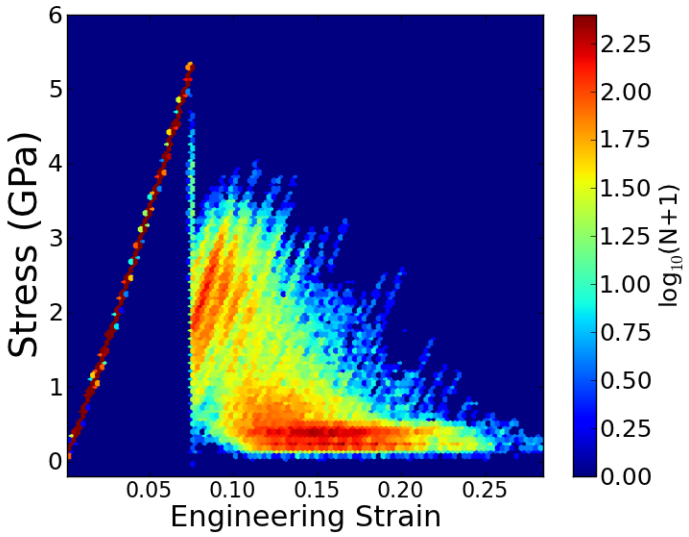

Figure 7.4. Stress-strain heat map constructed from 380 independent simulations of a NW with D_0 = 3.1 nm and L_0 = 20.4 nm elongated at 10 K.

0.19 where many of the NWs have ruptured and exhibit a small residual stress following failure (note that stress-strain data is collected for 2 Å of elongation following failure). Figure 7.5 plots the histogram of failure strains, confirming that many of the NWs fail in the ∼0.12-0.19 range. The wide range of failure strains in Figure 7.5 is surprising given the extremely low temperature at which the NWs are stretched, demonstrating the strong sensitivity of dislocation formation and behavior to variance in relative atomic positions arising from stochastic thermal fluctuation.

Figure 7.4 suggests that a vast majority of the 380 runs undergo ductile failure, in accordance with the predicted behavior from 7.1. However, there are a small number of cases in which the NW exhibits stress-

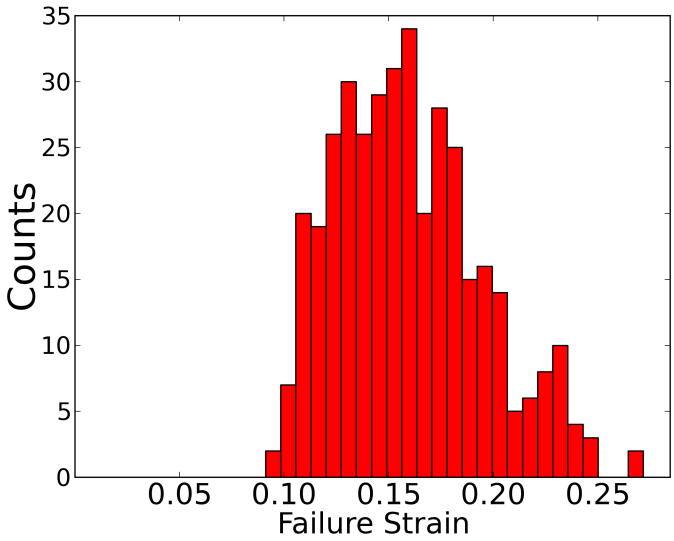

Figure 7.5. Histogram of the failure strain from 380 independent simulations of a NW with D_0 = 3.1 nm and L_0 = 20.4 nm elongated at 10 K.

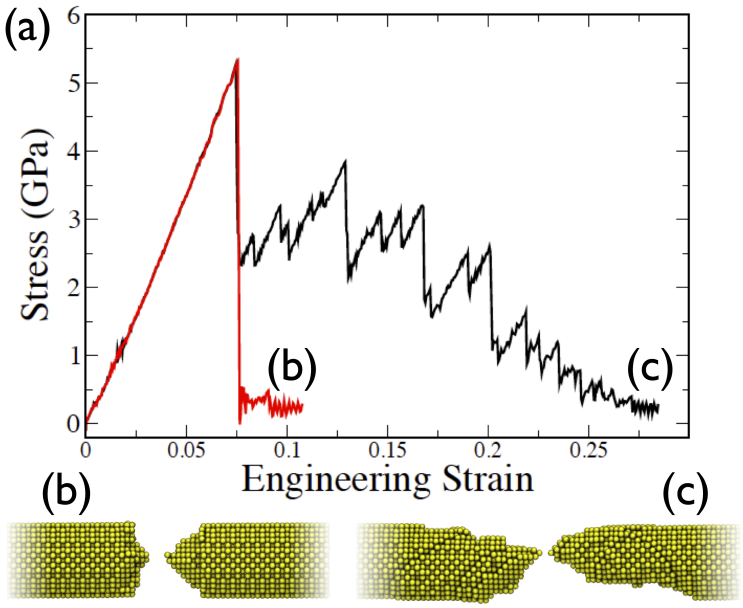

Figure 7.6. (a) Stress-strain curves for replicate runs of a Au NW (D_0 = 3.1 nm, L_0 = 20.4 nm) elongated at 10 K. In one case the NW undergoes (b) brittle failure while in another the wire undergoes (c) ductile failure. Zoomed-in snapshots immediately after NW failure are shown below.

strain behavior and post-rupture structure characteristic of brittle failure. This is illustrated in Figure 7.6a, where stress-strain data is plotted for the runs resulting in the lowest and highest failure strains. The red curve in Figure 7.6a drops off quickly following the yield point, and then remains relatively flat until the NW eventually fails. The lack of serrations in the stress-strain curve suggests that the NW experiences little

plastic deformation during elongation. The snapshot of the rupture region of the NW in Figure 7.6b also shows evidence of shearing along a single plane and no necking. In contrast, the black curve in Figure 7.6a exhibits numerous stress-strain serrations while the snapshot in Figure 7.6c shows evidence of significant slipping and necking. This result indicates that for this small-diameter NW elongated at 10 K, stochastic events are prominent enough to occasionally overcome rupture mechanisms dictated by NW size.

7.5.2 Role of Temperature

To investigate the role of temperature in NW failure, additional sets of simulations are performed for a NW with D_0 = 3.1 nm and L_0 = 40.6 nm. Note that this length is just below the transition value (L_C = 43.0 nm) predicted by the ductile-to-brittle model (equation 7.1) for partial-dislocation mediated deformation. Two hundred independent simulations are performed for each of four temperatures: 10, 100, 200, and 298 K. Note that this temperature range encompasses values applied in experiment,[112,122,123] and is well below the melting point of small Au NWs.[81]

Distinct temperature-dependent behavior is apparent from Figure 7.7. Prominent brittle failure can be

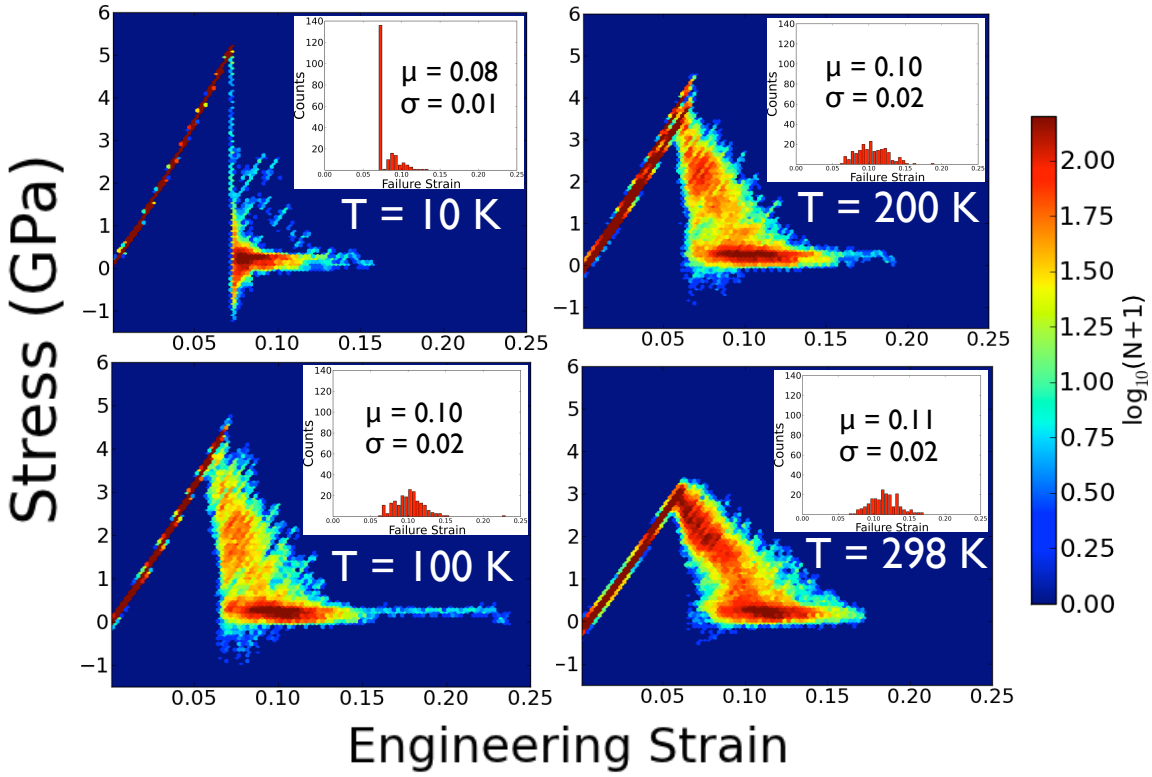

Figure 7.7. Stress-strain heat maps for a Au NW with D_0 = 3.1 nm and L_0 = 40.6 nm at four different temperatures. Two hundred independent simulations are performed at each temperature. The failure strain histograms, along with their corresponding average (μ) and standard deviation (σ), are inset.

observed in the heat maps by the presence of bright spots close to zero stress immediately after the yield point, whereas ductile failure exhibits brightly colored serrations extending well beyond the yield point. In Figure 7.7, the NWs fail in a predominantly brittle manner at 10 K, and become significantly more ductile as the temperature is increased. Enhanced ductility and plasticity have been reported previously [175] for NWs elongated at higher temperatures, owing to the increased magnitude of atomic oscillations about the atoms' equilibrium positions, which promotes reconstruction of the crystal lattice. This effect decreases the yield strain, ε_y, and yield stress, σ_y, of the NW at higher temperatures, effectively reducing the amount of energy available to drive deformation. The result of this is a tendency towards higher ductility and a reduction in the size and slope of the stress-strain serrations at high temperature, as seen in Figure 7.7.

At 10 K, the NW experiences predominantly brittle failure, with a majority of the NWs failing immediately after yielding. This behavior is striking in comparison to Figures 7.4 and 7.5, where a NW with half the initial length exhibits predominantly ductile failure behavior. The NW with D_0 = 3.1 nm undergoes a clear ductile-to-brittle transition when L_0 is increased from 20.4 to 40.6 nm. Equation 7.1, which predicts L_C between 40.8-57.7 nm, appears to overpredict L_C for NWs with D_0 = 3.1 nm elongated at 10 K.

7.5.3 Role of Nanowire Size

Figure 7.8 shows a clear transition from ductile to brittle failure with increasing L_0 at both temperatures. Serrations are present at lower values of L_0 but disappear at larger lengths. The transition occurs at a higher value of L_0 at 298 K compared to 10 K due to the aforementioned enhanced ductility effect. This behavior is also predicted by equation 7.1, with higher temperatures resulting in lower yield strain values. An instructive metric for quantifying failure mode is the total amount of strain that occurs after NW yielding. NWs that fail catastrophically feature very little strain following the yield point, while NWs undergoing plastic deformation are able to withstand some degree of strain after yielding. Figure 7.9 plots the strain after NW yielding as a function of L_0 for the two different temperatures. At 10 K, the strain after yielding is relatively high for the smallest value of L_0, but drops off quickly at L_0 = 40.6 nm. These data correspond to the NWs discussed previously (see Figures 7.3 and 7.7), and agree well with the previous interpretation that for L_0 = 20.4 nm the NW fails by a predominantly ductile mode while at L_0 = 40.6 nm a brittle mechanism is dominant. At initial lengths exceeding 40.6 nm the strain after yielding is minimal, indicating that the NWs are failing in a purely brittle manner. The exception to this is at L_0 = 60.8 nm, where there is evidence of occasional plasticity in the stress-strain heat map. The small error bars at high initial NW lengths also demonstrate the decreased variability in failure behavior within the brittle regime. At 298 K, the NWs experience extensive plasticity and exhibit high ductility at $L_0 < 60.8$ nm. The strain after yielding drops to a small value of $\sim$0.01 at L_0 = 60.8 nm, where brittle failure is the prominent rupture mode. Occasional plasticity is observed at L_0 = 80.9

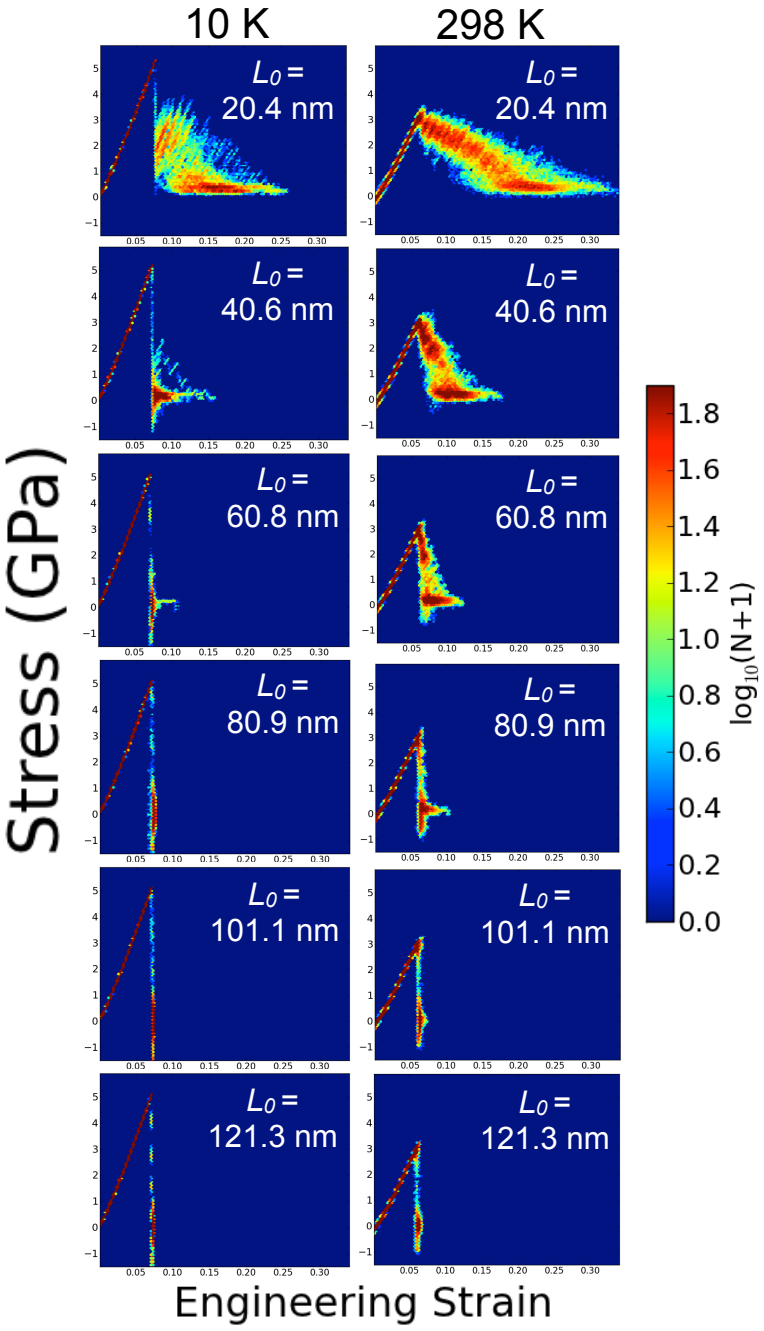

Figure 7.8. Stress-strain heatmaps for NWs with D_0 = 3.1 nm and varying lengths. The left column corresponds to simulations run at 10 K while the right column shows results at 298 K.

nm and L_0 = 101.1 nm before exclusively brittle behavior occurs at L_0 = 121.3 nm.

A summary of the mechanical properties of the 6 NWs at 10 and 298 K is presented in 7.1. The yield stress, σ_y, yield strain, ε_y, and Young's modulus, E, are higher at 10 K, and are not a strong function of NW length at either temperature. The values for σ_y and E agree well with previously reported values from Au

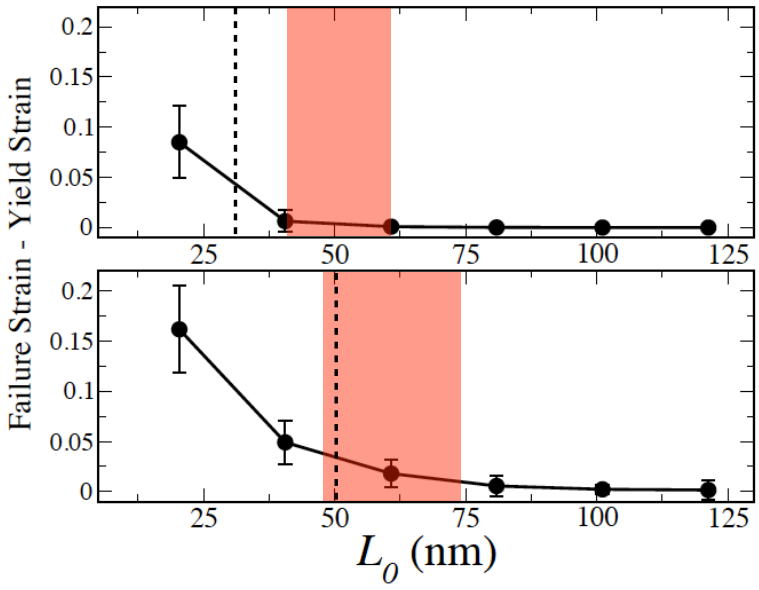

Figure 7.9. Strain after yielding for NWs with D_0 = 3.1 nm as a function of initial NW length at (top) 10 K and (bottom) 298 K. The dashed lines separate the ductile (left of the dashed line) and brittle (right of the dashed line) failure regions, as indicated by our simulation results. The colored region corresponds to the range of L_C values predicted by 7.1.

Table 7.1. Summary of mechanical properties for Au NWs with D_0 = 3.1 nm. The standard deviation is only reported when the relative uncertainty exceeds 10%.

L_0	σ_y (GPa)		ε_y		E (GPa)		ε_f	
(nm)	10 K	298 K	10 K	298 K	10 K	298 K	10 K	298 K
20.4	5.29	3.2	0.076	0.063	69.6	54.4	0.16 ± 0.04	0.23 ± 0.04
40.6	5.18	3.1	0.073	0.061	71.6	54.8	0.08 ± 0.01	0.11 ± 0.02
60.8	5.10	3.0	0.072	0.060	72.2	54.9	0.073	0.07 ± 0.01
80.9	5.07	3.0	0.072	0.060	71.9	54.7	0.072	0.065
101.1	5.13	3.0	0.072	0.059	72.3	54.8	0.072	0.062
121.3	5.10	3.0	0.072	0.059	72.3	54.5	0.072	0.060

NW simulations,[182,214,217] and the strength of the Au NWs are significantly larger than bulk Au, in agreement with experimental results.[131] It is important to note that, even though the Young's modulus is a measure of the stiffness of the material and clearly demonstrates a temperature dependence, it does not demonstrate a significant length dependence and thus it alone is not likely to be a meaningful predictor of the ductile-to-brittle transition.

Also plotted in Figure 7.9 are the predicted L_C ranges and the observed L_C values from the GPU simulations. The observed L_C value is taken as the midpoint between the largest L_0 exhibiting ductile behavior

and the smallest L_0 exhibiting brittle failure. As discussed previously, the NW with D_0 = 3.1 nm undergoes a ductile-to-brittle transition below the predicted L_C range. On the other hand, at 298 K the observed L_C value falls in the range predicted by equation 7.1. The observed L_C value has some uncertainty ($\sim$10 nm) associated with it, as the length of the simulated NWs is changed in $\sim$20 nm increments. Nevertheless, equation 7.1 predicts L_C with a fair amount of quantitative accuracy, and provides a reasonable initial guess for the true value of L_C. Equation 7.1 also accurately predicts the amount of increase in L_C occurring between 10 and 298 K. As noted previously, the failure behavior can exhibit some variability, especially close to L_C. From the simulated NW sizes, the failure behavior is always a predominance ($\geq$95%) of one failure mode (ductile or brittle). However, there may be characteristic NW sizes where an approximately even mixture of ductile and brittle failure occurs.

There is a clear tendency towards ductile behavior with decreases in NW length, and likewise, an increased tendency to brittle failure as NW length is increased. According to equation 7.1, changes to the NW diameter should also affect the NW failure behavior. To test this, additional simulations are performed at 10 K for two NWs, one with D_0 = 4.4 nm, L_0 = 20.5 nm and the other with D_0 = 6.0 nm, L_0 = 20.5 nm, to confirm the increased ductility effect for NWs with larger diameters. 204 independent simulations are performed for these NWs; in all simulations the NWs fail via a purely ductile mechanism as demonstrated by the stress-strain heatmaps in Figure 7.10, with the NWs becoming more ductile with increases in D_0. In particular, there is a clear decrease in the amount of stress-strain data appearing at low values of stress immediately following the yield point. Thus, the NW aspect ratio (L_0/D_0) is a critical parameter that may be used to adjust the degree of NW ductility.

It is somewhat surprising that the ductile-to-brittle model works well for the small-diameter NWs we consider here, as equation 7.1 was derived assuming the NWs obey classical dislocation theory. Prior work[130] has shown that the formation of noncrystalline structure (*e.g.*, polytetrahedra) is promoted in small-diameter NWs elongated at high temperature. However, the formation of polytetrahedra was significantly reduced with increases in NW diameter from 1.1 to 1.9 nm. As the NWs in the present study are even larger, limited noncrystalline structure formation is expected, and thus significant departures from classical dislocation behavior are unlikely. While shrinking the NW to diameters as low as $\sim$3.1 nm does not seem to impact the applicability of the ductile-to-brittle transition, temperature clearly plays an important role for the ductile-to-brittle transition, as higher temperatures promote ductile failure. These differences may be less pronounced for large-diameter NWs, where barriers to crystal reconstruction are significant.

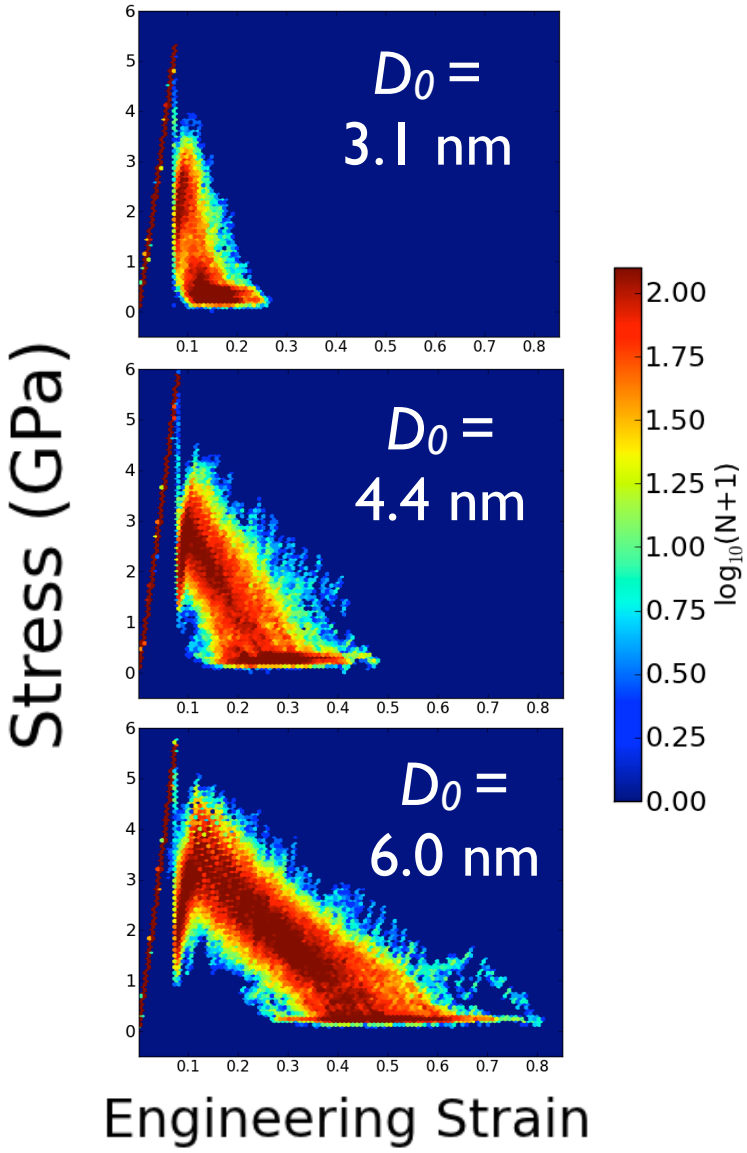

Figure 7.10. Stress-strain heatmaps for NWs with D_0 = 3.1, 4.4 , 6.0 nm and L_0 = 20.5 nm.

CHAPTER VIII

CONCLUSIONS AND RECOMMENDATIONS

8.1 Conclusions

Through the application of efficient, high-fidelity computational tools and models, significant new insight into the structural, mechanical, and electrical properties of common molecular electronics (ME) building blocks has been provided in this dissertation. These findings build upon the community's atomic-level understanding of common ME-based experiments, in particular the MCBJ technique. Several methods for tuning the properties and behavior of various systems and building blocks have also been provided. These methods should aid the development of new strategies for improved control in ME devices, towards the ultimate goal of practical application and commercialization.

Specifically, in Chapter IV, molecular dynamics simulations were performed to test the effect of molecular adsorption on the mechanical and morphological evolution of elongating Au NWs. A simple Lennard-Jones sphere model and a fully atomistic model for the adsorbate were tested on three different wire sizes (1.1, 1.5, and 1.9 nm in diameter). With each adsorbate model the adsorbate-Au interaction strength was systematically altered to get a comprehensive picture of the effect of different adsorbates on elongating AuNWs. The structure and mobility of an adsorbed monolayer was characterized on static and elongating Au NWs. The process of mechanically elongating a Au NW was found to not impact the monolayer surrounding bulk-like regions of the wire, however, along the thinning region of a Au NW, the adsorbed phase was found to be less structured and more mobile. This effect was attributed to fluctuations in the atomic positions of Au atoms that occur in the thinning region.

The ductile elongation of Au NWs in the presence of an adsorbate was enhanced relative to elongation in vacuum, by 231% for 1.1-nm Au NWs and 54% for 1.9-nm Au NWs. This result was rationalized by the lowering of the Au NW surface energy due to the presence of an adsorbate, which prolongs the lifetime of low-coordination structures that are especially prone to rupture in vacuum environments. Specifically, the stability of Au monatomic chains (MACs) was enhanced in adsorbate, in good quantitative agreement with experimental data from Refs.[142,190] On the other hand, molecules that interacted weakly with Au NWs worsened the mechanical stability of MACs. Helices that formed in the presence of adsorbate were found to (*i*) occur with higher frequency, (*ii*) possess higher mechanical stability, and (*iii*) display greater lengths than those that appear in vacuum environments.

Importantly, the simple Lennard-Jones model was found to adequately describe the impact of an adsorbate

on the properties of the monolayer and the mechanical stability of Au NWs, with only minor differences noted in monolayer mobility when compared to a fully atomistic adsorbate model. This is an important result since varying the interaction strength for a LJ model is straightforward and also because the LJ model is a computationally cheaper alternative than an explicit model. These results should enable the use of simple models in future simulation studies of Au NW elongation in solvent and/or an adsorbing species.

In Chapter V, important environmental factors were incorporated into simulations of the formation of molecular junctions. The study focused on important aspects of molecular junction formation and structure that were previously inaccessible with simulation. The results offer guidance on the design of monolayers and electrode geometries to yield desired properties, such as specific bonding geometries and/or tilt angles to control conductance. The extent of surface coverage was shown to affect the number of bridged molecules. Single-molecule junctions were found to occur commonly at intermediate to high surface coverages; however, at low inter-electrode separations maximum surface coverage was found to provide the highest probability of yielding single-molecule junctions, owing to the limited occurrence of multi-molecule junctions in densely packed monolayers. For low to intermediate surface coverages, the reduced adsorbate-adsorbate interactions resulted in relatively high probabilities for forming multi-molecule junctions.

The simulation results in Chapter V also demonstrated that electrode geometry affects the number, bonding geometry, and tilt angle of bridged molecules. In addition to influencing the number of bridged molecules, monolayer interactions were found to give rise to bonding geometry that is higher in energy than the preferred bonding geometry and tilt angles that are higher than those of bridged molecules in absence of a monolayer. These are important findings since it has been previously demonstrated that both bonding geometry and tilt angle can affect conductance by at least an order of magnitude,[11,22,50,83] while also impacting the measured IETS.[84] In addition to electrode structure and monolayer effects, a low simulated temperature (77 K) was found to significantly reduce the number of bridged molecules; however, the low temperature resulted in only small changes in the bonding geometry and tilt angle, in comparison to 298 K.

Chapter VI presented results from realistic simulations of Au-BDT-Au junction formation and elongation combined with high-fidelity conductance calculations. This work provided important new insight into the conductance behavior of Au-BDT-Au junctions. Namely, the computational approach demonstrated that BDT connected directly to a MAC results in enhanced conductance, and is caused by enhancements in the s and p_z density of states around ε_F in Au MAC atoms. This result offers an excellent explanation for the large, anomalous conductance increases observed in Au-BDT-Au break junction experiments,[43] and may additionally explain the large transmission observed in experiments by Kim and co-workers.[22] BDT-MAC structures were shown to be stable for long simulation times performed at 77 K, and exhibited very little overlap in their conductance distributions with those of other realistic junction geometries. Thus this specific

structural motif should be detectable in experiment.

Conductance fluctuations in structurally distinct Au-BDT-Au junctions were also investigated in Chapter VI. Conductance fluctuations in non-ideal junctions were demonstrated to be higher than those in an ideal junction. While changes in the molecule geometry dominated conductance fluctuations in structurally ideal junctions, the enhanced motion of the Au atoms in deformed electrodes led to an increased contribution to the conductance fluctuations from changes in the electrode geometry. The minimal role of Au geometry in flat-surface junctions and its significant role in highly deformed junctions highlight the importance of controlling structure in single-molecule conductance measurements. These results also showed that conductance fluctuations in thiolate-based break junctions, where significant deformation to the electrodes occurs,[26,40,47] may be difficult to control as both the molecule and electrode motion make significant contributions to the fluctuations. The presence of other complex bonding arrangements (e.g., Au-S-Au-S-Au "staple" motifs[147]) at the Au-S interface may further complicate this issue.[65,148] In contrast, linkers with weaker coupling (*e.g.*, amines) are unlikely to result in the formation of structures such as Au-Au_2-Au, and thus efforts to control molecular motion[42] may prove highly effective for controlling conductance fluctuations. These results also demonstrate the importance of employing realistic electrode models in computational studies.

In Chapter VII, porting of the TB-SMA potential to HOOMD-Blue, an open-source MD package that runs on GPUs, is described. The resulting speedups enable the failure mechanism of elongating Au NWs to be probed. Significant speedups from the single-GPU simulations were obtained, on the order of 5-11 relative to 8-core CPU simulations, 3-5 relative to 16-core CPU simulations, and 1-2.5 relative to 32-core CPU simulations. These speedups enabled a large number of simulations ($>$ 2000) to be carried out in order to map out the landscape of stress-strain behavior in NWs ranging in length from $\sim$20-120 nm and diameter from $\sim$3-5 nm. The applicability of the ductile-to-brittle transition was statistically confirmed for NWs with small diameters of 3.1 nm, although L_C was slightly over-predicted at low temperature (10 K). The important role of temperature in the ductile-to-brittle transition was demonstrated; it was shown that temperature can be used to tune failure behavior. Stochastic events due to thermal fluctuation were found to be prominent enough to occasionally cause non-characteristic failure behavior based on the NW size. These results provided comprehensive, statistical insight into NW failure that should be helpful for the controllable construction of nano- and atomic-scale devices. Additionally, these results demonstrated the utility of GPU computing in MD simulation studies requiring many independent trajectories for statistical purposes.

8.2 Recommendations for Future Work

8.2.1 Multi-Molecule Effects in Electron Transport Calculations

In Chapter VI, the effect of nonideal electrode configurations on the conductance properties of Au-BDT-Au junctions was considered. The presence of an adsorbed monolayer surrounding the bridged molecule is another factor that will likely influence the calculated conductance. It is likely that the presence of a surrounding monolayer will influence the conductance through a Au-BDT-Au junction, possibly accounting for the discrepancy between the experimentally measured and theoretically calculated values. The chemical composition of a non-bridged monolayer has already been shown to alter the electrode work function, giving rise to changes in conductance.[35] A more detailed study considering more realistic junction structures and environments would be valuable. Additionally, the presence of a monolayer may reduce the conductance fluctuations through a bridged molecule by confining its structure. Chapter V demonstrated that bridged molecules in the presence and absence of a monolayer adopt very different bonding geometries and tilt angles. Prior experimental work[42] reduced conductance fluctuations through a biphenyl molecule by synthesizing a rotaxane structure around the bridged molecule, which reduced the geometric freedom of the bridged molecule. The presence of a monolayer is likely to have a similar effect.

Another potential area to pursue is the conductance behavior of multi-molecule junctions, as work in Chapter V showed strong evidence supporting their formation. The conductance through molecules connected in parallel is often assumed to be the sum of each molecule's independent contribution to the conductance.[201] However, this assumption may break down in cases where molecules are strongly interacting, connected at adjacent electrode sites, or in the presence of a dense, non-bridged monolayer. Interference[218–220] and crosstalk[221] effects in molecular junctions have been studied previously, but not for BDT and not under environmentally realistic conditions.

8.2.2 Inelastic Electron Tunneling Spectroscopy Calculations of Simulated Au-BDT-Au Junctions

Inelastic electron tunneling spectroscopy (IETS) has recently emerged as a powerful tool for detecting the presence of molecular junctions and inferring their structural features.[4,17,22,43] IETS calculations[64,84,222] for molecular junctions provide a method for interpreting IETS experimental measurements. IETS calculations of Au-BDT-Au junctions would extend the applicability of the realistic molecular junction simulations by accounting for inelastic transport process through the junctions. One specific example where IETS calculations may provide considerable insight is for BDT connected directly to Au monatomic chains (MACs). Chapter VI showed that this configuration enhanced the transmission of the junction around the electrode Fermi level, thus causing increased conductance. In recent MCBJ experiments performed by Kim and co-workers,[22] the authors observed transmission values as high as 0.56 through Au-BDT-Au junctions. A crossover in the

IETS signal from peaks to dips in the inelastic excitations of the molecule accompanied these high values of transmission. It is possible that the presence of MACs could explain this IETS crossover, which would further demonstrate the importance of these structures in molecular devices. Similar case studies may provide additional explanations for the experimentally relevant structures in Au-BDT-Au junctions.

8.2.3 ReaxFF Simulations of Au-Thiol Systems

In addition to using the hybrid MD-MC approach, applying the ReaxFF force field to simulate the formation and elongation of Au-BDT-Au junctions could provide considerable insight into the mechanical and structural properties of molecular junctions. The advantage of ReaxFF is that the metal-molecule bonding geometry is modeled in a more continuous manner, such that unanticipated structures may emerge. Simulations could be performed with ReaxFF to investigate the bonding geometry as a function of monolayer coverage, temperature, and monolayer density, to compare with prior studies using the MD/MC approach. Many poorly understood experimental features, such as the reduced mechanical stability at low temperature [16] and Au-BDT bonding geometry, [119] may be deduced from such studies. Setting up these simulations would also require minimal time and effort, as parameters have been previously developed for Au [223,224] and Au/S/C/H, [225] and ReaxFF is implemented in LAMMPS, [153] a freely available MD package.

REFERENCES

[1]Moore, G. *Electronics* **1965**, 114–117.

[2]Zhirnov, V.; Cavin, R.; Hutchby, J.; Bourianoff, G. *Proc. IEEE* **2003**, *91*, 1934–1939.

[3]Lortscher, E.; Ciszek, J. W.; Tour, J.; Riel, H. *Small* **2006**, *2*, 973–977.

[4]Song, H.; Kim, Y.; Jang, Y. H.; Jeong, H.; Reed, M. A.; Lee, T. *Nature* **2009**, *462*, 1039–1043.

[5]Diez-Perez, I.; Hihath, J.; Lee, Y.; Yu, L.; Adamska, L.; Kozhushner, M. A.; Oleynik, I. I.; Tao, N. *Nature Chem.* **2009**, *1*, 635–641.

[6]Reed, M. A.; Zhou, C.; Muller, C. J.; Burgin, T. P.; Tour, J. M. *Science* **1997**, *278*, 252–254.

[7]Kergueris, C.; Bourgoin, J.; Palacin, S.; Esteve, D.; Urbina, C.; Magoga, M.; Joachim, C. *Phys. Rev. B* **1999**, *59*, 12505–12513.

[8]Weber, H.; Reichert, J.; Weigend, F.; Ochs, R.; Beckmann, D.; Mayor, M.; Ahlrichs, R.; von Lohneysen, H. *Chem. Phys.* **2002**, *281*, 113–125.

[9]Gonzalez, M. T.; Wu, S.; Huber, R.; van der Molen, S. J.; Schoenenberger, C.; Calame, M. *Nano Lett.* **2006**, *6*, 2238–2242.

[10]Ulrich, J.; Esrail, D.; Pontius, W.; Venkataraman, L.; Millar, D.; Doerrer, L. *J. Phys. Chem. B* **2006**, *110*, 2462–2466.

[11]Tsutsui, M.; Teramae, Y.; Kurokawa, S.; Sakai, A. *Appl. Phys. Lett.* **2006**, *89*, 163111.

[12]Lortscher, E.; Weber, H. B.; Riel, H. *Phys. Rev. Lett.* **2007**, *98*, 176807.

[13]Wu, S.; Gonzalez, M. T.; Huber, R.; Grunder, S.; Mayor, M.; Schoenenberger, C.; Calame, M. *Nat. Nanotech.* **2008**, *3*, 569–574.

[14]Tsutsui, M.; Shoji, K.; Morimoto, K.; Taniguchi, M.; Kawai, T. *App. Phys. Lett.* **2008**, *92*, 223110.

[15]Teramae, Y.; Horiguchi, K.; Hashimoto, S.; Tsutsui, M.; Kurokawa, S.; Sakai, A. *App. Phys. Lett.* **2008**, *93*.

[16]Tsutsui, M.; Taniguchi, M.; Kawai, T. *Nano Lett.* **2009**, *9*, 2433–2439.

[17]Tsutsui, M.; Taniguchi, M.; Shoji, K.; Yokota, K.; Kawai, T. *Nanoscale* **2009**, *1*, 164–170.

[18]Horiguchi, K.; Tsutsui, M.; Kurokawa, S.; Sakai, A. *Nanotech.* **2009**, *20*, 025204.

[19]Taniguchi, M.; Tsutsui, M.; Shoji, K.; Fujiwara, H.; Kawai, T. *J. Am. Chem. Soc.* **2009**, *131*, 14146.

[20]Zotti, L. A.; Kirchner, T.; Cuevas, J.-C.; Pauly, F.; Huhn, T.; Scheer, E.; Erbe, A. *Small* **2010**, *6*, 1529–1535.

[21]Yokota, K.; Taniguchi, M.; Tsutsui, M.; Kawai, T. *J. Am. Chem. Soc.* **2010**, *132*, 17364–17365.

[22]Kim, Y.; Pietsch, T.; Erbe, A.; Belzig, W.; Scheer, E. *Nano Lett.* **2011**, *11*, 3734–3738.

[23]Xiao, X.; Xu, B.; Tao, N. *Nano Lett.* **2004**, *4*, 267–271.

[24]Venkataraman, L.; Klare, J. E.; Nuckolls, C.; Hybertsen, M. S.; Steigerwald, M. L. *Nature* **2006**, *442*, 904–907.

[25]Venkataraman, L.; Klare, J.; Tam, I.; Nuckolls, C.; Hybertsen, M.; Steigerwald, M. *Nano Lett.* **2006**, *6*, 458–462.

[26]Huang, Z.; Chen, F.; Bennett, P. A.; Tao, N. *J. Am. Chem. Soc.* **2007**, *129*, 13225–13231.

[27]Fujii, S.; Akiba, U.; Fujihira, M. *Chem. Lett.* **2008**, *37*, 408–409.

[28]Li, C.; Pobelov, I.; Wandlowski, T.; Bagrets, A.; Arnold, A.; Evers, F. *J. Am. Chem. Soc.* **2008**, *130*, 318–326.

[29]Lu, Q.; Liu, K.; Zhang, H.; Du, Z.; Wang, X.; Wang, F. *ACS Nano* **2009**, *3*, 3861–3868.

[30]Kamenetska, M.; koentopp, M.; Whalley, A. C.; Park, Y. S.; Steigerwald, M. L.; Nuckolls, C.; Hybertsen, M. S.; Venkataraman, L. *Phys. Rev. Lett.* **2009**, *102*, 126803.

[31]Mishchenko, A.; Vonlanthen, D.; Meded, V.; Buerkle, M.; Li, C.; Pobelov, I. V.; Bagrets, A.; Viljas, J. K.; Pauly, F.; Evers, F.; Mayor, M.; Wandlowski, T. *Nano Lett.* **2010**, *10*, 156–163.

[32]Zhou, J.; Chen, G.; Xu, B. *J. Phys. Chem. C* **2010**, *114*, 8587–8592.

[33]Xing, Y.; Park, T.-H.; Venkatramani, R.; Keinan, S.; Beratan, D. N.; Therien, M. J.; Borguet, E. *J. Am. Chem. Soc.* **2010**, *132*, 7946–7956.

[34]Schneebeli, S. T.; Kamenetska, M.; Cheng, Z.; Skouta, R.; Friesner, R. A.; Venkataraman, L.; Breslow, R. *J. Am. Chem. Soc.* **2011**, *133*, 2136–2139.

[35]Fatemi, V.; Kamenetska, M.; Neaton, J. B.; Venkataraman, L. *Nano Lett.* **2011**, *11*, 1988–1992.

[36]Meisner, J. S.; Kamenetska, M.; Krikorian, M.; Steigerwald, M. L.; Venkataraman, L.; Nuckolls, C. *Nano Lett.* **2011**, *11*, 1575–1579.

[37]Guo, S.; Hihath, J.; Diez-Perez, I.; Tao, N. *J. Am. Chem. Soc.* **2011**, *133*, 19189–19197.

[38]Leary, E.; Teresa Gonzalez, M.; van der Pol, C.; Bryce, M. R.; Filippone, S.; Martin, N.; Rubio-Bollinger, G.; Agrait, N. *Nano Lett.* **2011**, *11*, 2236–2241.

[39]Li, Z.; Borguet, E. *J. Am. Chem. Soc.* **2012**, *134*, 63–66.

[40]Arroyo, C. R.; Leary, E.; Castellanos-Gomez, A.; Rubio-Bollinger, G.; Teresa Gonzalez, M.; Agrait, N. *J. Am. Chem. Soc.* **2011**, *133*, 14313–14319.

[41]Cheng, Z. L.; Skouta, R.; Vazquez, H.; Widawsky, J. R.; Schneebeli, S.; Chen, W.; Hybertsen, M. S.; Breslow, R.; Venkataraman, L. *Nature Nanotech.* **2011**, *6*, 353–357.

[42]Kiguchi, M.; Nakashima, S.; Tada, T.; Watanabe, S.; Tsuda, S.; Tsuji, Y.; Terao, J. *Small* **2012**, *8*, 726–730.

[43]Bruot, C.; Hihath, J.; Tao, N. *Nature Nanotech.* **2012**, *7*, 35–40.

[44]Cui, X.; Primak, A.; Zarate, X.; Tomfohr, J.; Sankey, O.; Moore, A.; Moore, T.; Gust, D.; Harris, G.; Lindsay, S. *Science* **2001**, *294*, 571–574.

[45]Beebe, J.; Engelkes, V.; Miller, L.; Frisbie, C. *J. Am. Chem. Soc.* **2002**, *124*, 11268–11269.

[46]Frei, M.; Aradhya, S. V.; Koentopp, M.; Hybertsen, M. S.; Venkataraman, L. *Nano Lett.* **2011**, *11*, 1518–1523.

[47]Frei, M.; Aradhya, S. V.; Hybertsen, M. S.; Venkataraman, L. *J. Am. Chem. Soc.* **2012**, *134*, 4003–4006.

[48]Haiss, W.; van Zalinge, H.; Higgins, S.; Bethell, D.; Hobenreich, H.; Schiffrin, D.; Nichols, R. *J. Am. Chem. Soc.* **2003**, *125*, 15294–15295.

[49]Haiss, W.; Wang, C.; Grace, I.; Batsanov, A. S.; Schiffrin, D. J.; Higgins, S. J.; Bryce, M. R.; Lambert, C. J.; Nichols, R. J. *Nature Mat.* **2006**, *5*, 995–1002.

[50]Haiss, W.; Wang, C.; Jitchati, R.; Grace, I.; Martin, S.; Batsanov, A. S.; Higgins, S. J.; Bryce, M. R.; Lambert, C. J.; Jensen, P. S.; Nichols, R. J. *J. Phys. Cond. Matt.* **2008**, *20*, 374119.

[51]Haiss, W.; Martin, S.; Leary, E.; van Zalinge, H.; Higgins, S. J.; Bouffier, L.; Nichols, R. J. *J. Phys. Chem. C* **2009**, *113*, 5823–5833.

[52]Leary, E.; Hobenreich, H.; Higgins, S. J.; van Zalinge, H.; Haiss, W.; Nichols, R. J.; Finch, C. M.; Grace, I.; Lambert, C. J.; McGrath, R.; Smerdon, J. *Phys. Rev. Lett.* **2009**, *102*.

[53]Kay, N. J.; Nichols, R. J.; Higgins, S. J.; Haiss, W.; Sedghi, G.; Schwarzacher, W.; Mao, B.-W. *J. Phys. Chem. C* **2011**, *115*, 21402–21408.

[54]Akkerman, H.; Blom, P.; de Leeuw, D.; de Boer, B. *Nature* **2006**, *441*, 69–72.

[55]Bandyopadhyay, A.; Pati, R.; Sahu, S.; Peper, F.; Fujita, D. *Nature Phys.* **2010**, *6*, 369–375.

[56]Lindsay, S. M.; Ratner, M. A. *Adv. Mat.* **2007**, *19*, 23–31.

[57]Di Ventra, M.; Pantelides, S.; Lang, N. *Phys. Rev. Lett.* **2000**, *84*, 979–982.

[58]Nitzan, A.; Ratner, M. *Science* **2003**, *300*, 1384–1389.

[59]Emberly, E.; Kirczenow, G. *Phys. Rev. B* **2001**, *64*, 235412.

[60]Basch, H.; Cohen, R.; Ratner, M. A. *Nano Lett.* **2005**, *5*, 1668–1675, PMID: 16159203.

[61]Hu, Y.; Zhu, Y.; Gao, H.; Guo, H. *Phys. Rev. Lett.* **2005**, *95*, 156803.

[62]Pontes, R. B.; Novaes, F. D.; Fazzio, A.; da Silva, A. J. R. *J. Am. Chem. Soc.* **2006**, *128*, 8996–8997.

[63]Sen, A.; Kaun, C.-C. *ACS Nano* **2010**, *4*, 6404–6408.

[64]Paulsson, M.; Krag, C.; Frederiksen, T.; Brandbyge, M. *Nano Lett.* **2009**, *9*, 117–121.

[65]Strange, M.; Lopez-Acevedo, O.; Hakkinen, H. *J. Phys. Chem. Lett.* **2010**, *1*, 1528–1532.

[66]Sergueev, N.; Tsetseris, L.; Varga, K.; Pantelides, S. *Phys. Rev. B* **2010**, *82*, 073106.

[67]Pontes, R. B.; Rocha, A. R.; Sanvito, S.; Fazzio, A.; Roque da Silva, A. J. *ACS Nano* **2011**, *5*, 795–804.

[68]Andrews, D. Q.; Van Duyne, R. P.; Ratner, M. A. *Nano Lett.* **2008**, *8*, 1120–1126.

[69]Cao, H.; Jiang, J.; Ma, J.; Luo, Y. *J. Am. Chem. Soc.* **2008**, *130*, 6674–6675.

[70]Maul, R.; Wenzel, W. *Phys. Rev. B* **2009**, *80*, 045424.

[71]Kim, H. S.; Kim, Y.-H. *Phys. Rev. B* **2010**, *82*, 075412.

[72]French, W. R.; Iacovella, C. R.; Cummings, P. T. *J. Phys. Chem. C* **2011**, *115*, 18422–18433.

[73]French, W. R.; Iacovella, C. R.; Cummings, P. T. *ACS Nano* **2012**, *6*, 2779–2789.

[74]French, W. R.; Iacovella, C. R.; Rungger, I.; Souza, A. M.; Sanvito, S.; Cummings, P. T. *Nanoscale, In Press.*

[75]French, W. R.; Iacovella, C. R.; Rungger, I.; Souza, A. M.; Sanvito, S.; Cummings, P. T. *J. Phys. Chem. Lett.* *4*, 887–891.

[76]French, W. R.; Pervaje, A. K.; Santos, A. P.; Iacovella, C. R.; Cummings, P. T. *In Preparation.*

[77]Pu, Q.; Leng, Y.; Tsetseris, L.; Park, H. S.; Pantelides, S. T.; Cummings, P. T. *J. Chem. Phys.* **2007**, *126*.

[78]Pu, Q.; Leng, Y.; Cummings, P. T. *J. Am. Chem. Soc.* **2008**, *130*, 17907–17912.

[79]Leng, Y.; Krstic, P.; Wells, J.; Cummings, P.; Dean, D. *J. Chem. Phys.* **2005**, *122*, 244721.

[80]Leng, Y. S.; Dyer, P. J.; Krstic, P. S.; Harrison, R. J.; Cummings, P. T. *Mol. Phys.* **2007**, *105*, 293–300.

[81]Pu, Q.; Leng, Y.; Tsetseris, L.; Park, H. S.; Pantelides, S. T.; Cummings, P. T. *J. Chem. Phys.* **2007**, *126*, 144707.

[82]Pu, Q.; Leng, Y.; Zhao, X.; Cummings, P. T. *J. Phys. Chem. C* **2010**, *114*, 10365–10372.

[83]Bratkovsky, A.; Kornilovitch, P. *Phys. Rev. B* **2003**, *67*, 115307.

[84]Lin, L.-L.; Wang, C.-K.; Luo, Y. *ACS Nano* **2011**, *5*, 2257–2263.

[85]Pemmaraju, C. D.; Archer, T.; Sanchez-Portal, D.; Sanvito, S. *Phys. Rev. B* **2007**, *75*, 045101.

[86]Toher, C.; Sanvito, S. *Phys. Rev. Lett.* **2007**, *99*, 056801.

[87]Toher, C.; Sanvito, S. *Phys. Rev. B* **2008**, *77*, 155402.

[88]Wu, Z.; Zhang, Y.-W.; Jhon, M. H.; Gao, H.; Srolovitz, D. J. *Nano Lett.* **2012**, *12*, 910–914.

[89]Cleri, F.; Rosato, V. *Phys. Rev. B* **1993**, *48*, 22–33.

[90]Anderson, J. A.; Lorenz, C. D.; Travesset, A. *J. Comp. Phys.* **2008**, *227*, 5342–5359.

[91]Nie, Z.; Petukhova, A.; Kumacheva, E. *Nature Nanotech.* **2010**, *5*, 15–25.

[92]Kumar, C. S. S. R. *Mat. Today* **2010**, *12*, 24–30.

[93]Xu, S.; Qin, Y.; Xu, C.; Wei, Y.; Yang, R.; Wang, Z. L. *Nature Nanotech.* **2010**, *5*, 366–373.

[94]Hodes, G. *Adv. Mat.* **2007**, *19*, 639–655.

[95]Rashkeev, S. N.; Lupini, A. R.; Overbury, S. H.; Pennycook, S. J.; Pantelides, S. T. *Phys. Rev. B* **2007**, *76*, 035438.

[96]*International Technology Roadmap for Semiconductors*; 2012; pp 1–66.

[97]Vuillaume, D. *Comptes Rendus Phys.* **2008**, *9*, 78–94.

[98]Roy, S.; Asenov, A. *Science* **2005**, *309*, 388–390.

[99]Shinada, T.; Okamoto, S.; Kobayashi, T.; Ohdomari, I. *Nature* **2005**, *437*, 1128–1131.

[100]Heath, J.; Ratner, M. *Phys. Today* **2003**, *56*, 43–49.

[101]Tao, N. J. *Nature Nanotech.* **2006**, *1*, 173–181.

[102]McCreery, R. L.; Bergren, A. J. *Adv. Mat.* **2009**, *21*, 4303–4322.

[103]Nichols, R. J.; Haiss, W.; Higgins, S. J.; Leary, E.; Martin, S.; Bethell, D. *Phys. Chem. Chem. Phys.* **2010**, *12*, 2801–2815.

[104]Aviram, A.; Ratner, M. *Chem. Phys. Lett.* **1974**, *29*, 277–283.

[105]Ulman, A. *Chem. Rev.* **1996**, *96*, 1533–1554.

[106]Xu, S.; Cruchon-Dupeyrat, S.; Garno, J.; Liu, G.; Jennings, G.; Yong, T.; Laibinis, P. *J. Chem. Phys.* **1998**, *108*, 5002–5012.

[107]Love, J.; Estroff, L.; Kriebel, J.; Nuzzo, R.; Whitesides, G. *Chem. Rev.* **2005**, *105*, 1103–1169.

[108]Vericat, C.; Vela, M. E.; Benitez, G.; Carro, P.; Salvarezza, R. C. *Chem. Soc. Rev.* **2010**, *39*, 1805–1834.

[109]Fuechsle, M.; Miwa, J. A.; Mahapatra, S.; Ryu, H.; Lee, S.; Warschkow, O.; Hollenberg, L. C. L.; Klimeck, G.; Simmons, M. Y. *Nature Nanotech.* **2012**, *7*, 242–246.

[110]Park, J.; Pasupathy, A.; Goldsmith, J.; Chang, C.; Yaish, Y.; Petta, J.; Rinkoski, M.; Sethna, J.; Abruna, H.; McEuen, P.; Ralph, D. *Nature* **2002**, *417*, 722–725.

[111]Muller, C.; Vanruitenbeek, J.; Dejongh, L. *Phys. Rev. Lett.* **1992**, *69*, 140–143.

[112]Tsutsui, M.; Shoji, K.; Taniguchi, M.; Kawai, T. *Nano Lett.* **2008**, *8*, 345–349.

[113]Xu, B.; Tao, N. *Science* **2003**, *301*, 1221–1223.

[114]Nara, J.; Higai, S.; Morikawa, Y.; Ohno, T. *J. Chem. Phys.* **2004**, *120*, 6705–6711.

[115]Stokbro, K.; Taylor, J.; Brandbyge, M.; Mozos, J.; Ordejon, P. *Comp. Mat. Sci.* **2003**, *27*, 151–160.

[116]Tomfohr, J.; Sankey, O. *J. Chem. Phys.* **2004**, *120*, 1542–1554.

[117]Faleev, S.; Leonard, F.; Stewart, D.; van Schilfgaarde, M. *Phys. Rev. B* **2005**, *71*, 195422.

[118]Varga, K.; Pantelides, S. T. *Phys. Rev. Lett.* **2007**, *98*, 076804.

[119]Strange, M.; Rostgaard, C.; Hakkinen, H.; Thygesen, K. S. *Phys. Rev. B* **2011**, *83*, 115108.

[120]Kruger, D.; Fuchs, H.; Rousseau, R.; Marx, D.; Parrinello, M. *Phys. Rev. Lett.* **2002**, *89*, 186402.

[121]Rubio, G.; Agrait, N.; Vieira, S. *Phys. Rev. Lett.* **1996**, *76*, 2302–2305.

[122]Scheer, E.; Agrait, N.; Cuevas, J.; Yeyati, A.; Ludoph, B.; Martin-Rodero, A.; Bollinger, G.; van Ruitenbeek, J.; Urbina, C. *Nature* **1998**, *394*, 154–157.

[123]Yanson, A.; Bollinger, G.; van den Brom, H.; Agrait, N.; van Ruitenbeek, J. *Nature* **1998**, *395*, 783–785.

[124]Marszalek, P.; Greenleaf, W.; Li, H.; Oberhauser, A.; Fernandez, J. *Proc. Nat. Acad. Sci. Unit. St. Am.* **2000**, *97*, 6282–6286.

[125]Coura, P.; Legoas, S.; Moreira, A.; Sato, F.; Rodrigues, V.; Dantas, S.; Ugarte, D.; Galvao, D. *Nano Lett.* **2004**, *4*, 1187–1191.

[126]Rodrigues, V.; Ugarte, D. *Phys. Rev. B* **2001**, *63*, 1–4.

[127]Rodrigues, V.; Fuhrer, T.; Ugarte, D. *Phys. Rev. Lett.* **2000**, *85*, 4124–4127.

[128]Oshima, Y.; Kondo, Y.; Takayanagi, K. *J. Electron Microscropy* **2003**, *52*, 49–55.

[129]Kondo, Y.; Takayanagi, K. *Science* **2000**, *289*, 606–608.

[130]Iacovella, C. R.; French, W. R.; Cook, B. G.; Kent, P. R. C.; Cummings, P. T. *ACS Nano* **2011**, *5*, 10065–10073.

[131]Seo, J.-H.; Yoo, Y.; Park, N.-Y.; Yoon, S.-W.; Lee, H.; Han, S.; Lee, S.-W.; Seong, T.-Y.; Lee, S.-C.; Lee, K.-B.; Cha, P.-R.; Park, H. S.; Kim, B.; Ahn, J.-P. *Nano Lett.* **2011**, *11*, 3499–3502.

[132]Richter, G.; Hillerich, K.; Gianola, D. S.; Monig, R.; Kraft, O.; Volkert, C. A. *Nano Lett.* **2009**, *9*, 3048–3052.

[133]Yue, Y.; Liu, P.; Zhang, Z.; Han, X.; Ma, E. *Nano Lett.* **2011**, *11*, 3151–3155.

[134]Yue, Y.; Liu, P.; Deng, Q.; Ma, E.; Zhang, Z.; Han, X. *Nano Lett.* **2012**, *12*, 4045–4049.

[135]Lu, Y.; Huang, J. Y.; Wang, C.; Sun, S.; Lou, J. *Nature Nanotech.* **2010**, *5*, 218–224.

[136]Daw, M.; Baskes, M. *Phys. Rev. B* **1984**, *29*, 6443–6453.

[137]Ercolessi, F.; Parrinello, M.; Tosatti, E. *Phil. Mag. A* **1988**, *58*, 213–226.

[138]Chen, F.; Li, X.; Hihath, J.; Huang, Z.; Tao, N. *J. Am. Chem. Soc.* **2006**, *128*, 15874–15881.

[139]Bilic, A.; Reimers, J. R.; Hush, N. S.; Hoft, R. C.; Ford, M. J. *J. Chem. Theory and Comp.* **2006**, *2*, 1093–1105.

[140]Cafe, P. F.; Larsen, A. G.; Yang, W.; Bilic, A.; Blake, I. M.; Crossley, M. J.; Zhang, J.; Wackerbarth, H.; Ulstrup, J.; Reimers, J. R. *J. Phys. Chem. C* **2007**, *111*, 17285–17296.

[141]Piana, S.; Bilic, A. *J. Phys. Chem. B* **2006**, *110*, 23467–23471.

[142]He, H.; Shu, C.; Li, C.; Tao, N. *J. Electroanalyt. Chem.* **2002**, *522*, 26–32.

[143]Humphrey, W.; Dalke, A.; Schulten, K. *J. Mol. Graph.* **1996**, *14*, 33–38.

[144]Jorgensen, W.; Maxwell, D.; TiradoRives, J. *J. Am. Chem. Soc.* **1996**, *118*, 11225–11236.

[145]Rappe, A.; Casewit, C.; Colwell, K.; Goddard, W.; Skiff, W. *J. Am. Chem. Soc.* **1992**, *114*, 10024–10035.

[146]Heinz, H.; Vaia, R. A.; Farmer, B. L.; Naik, R. R. *J. Phys. Chem. C* **2008**, *112*, 17281–17290.

[147]Cossaro, A.; Mazzarello, R.; Rousseau, R.; Casalis, L.; Verdini, A.; Kohlmeyer, A.; Floreano, L.; Scandolo, S.; Morgante, A.; Klein, M. L.; Scoles, G. *Science* **2008**, *321*, 943–946.

[148]Hakkinen, H. *Nature Chem.* **2012**, *4*, 443–455.

[149]Fischer, D.; Curioni, A.; Andreoni, W. *Langmuir* **2003**, *19*, 3567–3571.

[150]Wan, L.; Terashima, M.; Noda, H.; Osawa, M. *J. Phys. Chem. B* **2000**, *104*, 3563–3569.

[151]Mulliken, R. *J. Chem. Phys.* **1962**, *36*, 3428.

[152]Iacovella, C.; French, W.; Cummings, P. *Proc. SciDAC* **2011**, Denver, CO, July 10–14.

[153]Plimpton, S. *J. Comp. Phys.* **1995**, *117*, 1–19.

[154]Hoover, W. *Phys. Rev. A* **1985**, *31*, 1695–1697.

[155]Nose, S. *J. Chem. Phys.* **1984**, *81*, 511–519.

[156]Metropolis, N.; Rosenbluth, A.; Rosenbluth, A.; Teller, A.; Teller, E. *J. Chem. Phys.* **1953**, *21*, 1087–1092.

[157]Zhao, X.; Leng, Y.; Cummings, P. *Langmuir* **2006**, *22*, 4116–4124.

[158]Frenkel, D.; Smit, B. *Understanding Molecular Simulation: From Algorithms to Applications*; Academic Press: San Diego, 2002.

[159]Kofke, D.; Glandt, E. *Mol. Phys.* **1988**, *64*, 1105–1131.

[160]Hohenberg, P.; Kohn, W. *Phys. Rev.* **1964**, *136*, B864.

[161]Kohn, W.; Sam, L. J. *Phys. Rev.* **1965**, *140*, A1133.

[162]Ordejon, P.; Artacho, E.; Soler, J. *Phys. Rev. B* **1996**, *53*, 10441–10444.

[163]Sanchez-Portal, D.; Ordejon, P.; Artacho, E.; Soler, J. *Int. J. Quantum Chem.* **1997**, *65*, 453–461.

[164]Neaton, J. B.; Hybertsen, M. S.; Louie, S. G. *Phys. Rev. Lett.* **2006**, *97*.

[165]Ashcroft, N. W.; Mermin, N. D. *Solid State Physics*; Saunders College Publishing and harcourt Brace College Publishing: Fort Worth, 1976.

[166]Datta, S. *Electron Transport in Mesoscopic Systems*; Cambridge University Press: Cambridge, 1997.

[167]Koentopp, M.; Chang, C.; Burke, K.; Car, R. *J. Phys. Cond. Matt.* **2008**, *20*, 083203.

[168]Strange, M.; Kristensen, I. S.; Thygesen, K. S.; Jacobsen, K. W. *J. Chem. Phys.* **2008**, *128*, 114714.

[169]Ke, S.-H.; Baranger, H. U.; Yang, W. *J. Chem. Phys.* **2007**, *127*, 144107.

[170]Rocha, A.; Garcia-Suarez, V.; Bailey, S.; Lambert, C.; Ferrer, J.; Sanvito, S. *Phys. Rev. B* **2006**, *73*, 085414.

[171]Rungger, I.; Sanvito, S. *Phys. Rev. B* **2008**, *78*, 035407.

[172]Yang, A.-C.; Weng, C.-I. *J. Phys. Chem. C* **2010**, *114*, 8697–8709.

[173]Zimmerman, J.; Webb, E.; Hoyt, J.; Jones, R.; Klein, P.; Bammann, D. *Mod. Sim. Mat. Sci. Eng.* **2004**, *12*, S319–S332.

[174]Subramaniyan, A. K.; Sun, C. T. *Int. J. Sol. Struct.* **2008**, *45*, 4340–4346.

[175]Koh, S.; Lee, H.; Lu, C.; Cheng, Q. *Phys. Rev. B* **2005**, *72*, 085414.

[176]Pan, N.; Wang, B.; Wang, X.; Hou, J. G. *J. Mat. Chem.* **2010**, *20*, 5567–5581.

[177]Kondo, Y.; Takayanagi, K. *Phys. Rev. Lett.* **1997**, *79*, 3455–3458.

[178]Huo, Z.; Tsung, C.-k.; Huang, W.; Zhang, X.; Yang, P. *Nano Lett.* **2008**, *8*, 2041–2044.

[179]Sato, F.; Moreira, A.; Coura, P.; Dantas, S.; Legoas, S.; Ugarte, D.; Galvao, D. *App. Phys. A-Mat. Sci. & Proc.* **2005**, *81*, 1527–1531.

[180]Lin, J.; Ju, S.; Lee, W. *Phys. Rev. B* **2005**, *72*, 1–6.

[181]Wang, D.; Zhao, J.; Hu, S.; Yin, X.; Liang, S.; Liu, Y.; Deng, S. *Nano Lett.* **2007**, *7*, 1208–1212.

[182]Koh, S. J. A.; Lee, H. P. *Nanotech.* **2006**, *17*, 3451–3467.

[183]Wang, B.; Yin, S.; Wang, G.; Buldum, A.; Zhao, J. *Phys. Rev. Lett.* **2001**, *86*, 2046–2049.

[184]Wen, Y.-H.; Wang, Q.; Liew, K. M.; Zhu, Z.-Z. *Phys. Lett. A* **2010**, *374*, 2949–2952.

[185]Weinberger, C. R.; Cai, W. *Nano Lett.* **2010**, *10*, 139–142.

[186]Xu, J.; Wang, H.; Liu, C.; Yang, Y.; Chen, T.; Wang, Y.; Wang, F.; Liu, X.; Xing, B.; Chen, H. *J. Am. Chem. Soc.* **2010**, *132*, 11920–11922.

[187]Shi, P.; Zhang, J.; Lin, H.-Y.; Bohn, P. W. *Small* **2010**, *6*, 2598–2603.

[188]Guo, S.; Hihath, J.; Tao, N. *Nano Lett.* **2011**, *11*, 927–933.

[189]Tsutsui, M.; Shoji, K.; Morimoto, K.; Taniguchi, M.; Kawai, T. *App. Phys. Lett.* **2008**, *92*, 223110.

[190]Tsutsui, M.; Taniguchi, M.; Kawai, T. *Nano Lett.* **2009**, *9*, 2433–2439.

[191]Velez, P.; Dassie, S. A.; Leiva, E. P. M. *Phys. Rev. B* **2010**, *81*, 235435.

[192]Bogozi, A.; Lam, O.; He, H.; Li, C.; Tao, N.; Nagahara, L.; Amlani, I.; Tsui, R. *J. Am. Chem. Soc.* **2001**, *123*, 4585–4590.

[193]Krishna, R.; van Baten, J. *Ind. & Eng. Chem. Res.* **2005**, *44*, 6939–6947.

[194]Jayaraman, A.; Schweizer, K. S. *J. Chem. Phys.* **2008**, *128*, 1–13.

[195]Jayaraman, A.; Schweizer, K. S. *Langmuir* **2008**, *24*, 11119–11130.

[196]Dubois, L.; Nuzzo, R. *Ann. Rev. Phys. Chem.* **1992**, *43*, 437–463.

[197]Hostetler, M.; Wingate, J.; Zhong, C.; Harris, J.; Vachet, R.; Clark, M.; Londono, J.; Green, S.; Stokes, J.; Wignall, G.; Glish, G.; Porter, M.; Evans, N.; Murray, R. *Langmuir* **1998**, *14*, 17–30.

[198]Jimenez, A.; Sarsa, A.; Blazquez, M.; Pineda, T. *J. Phys. Chem. C* **2010**, *114*, 21309–21314.

[199]Singh, C.; Ghorai, P. K.; Horsch, M. A.; Jackson, A. M.; Larson, R. G.; Stellacci, F.; Glotzer, S. C. *Phys. Rev. Lett.* **2007**, *99*, 1–4.

[200]Asar, J. A. O.; Mariscal, M. M.; Leiva, E. P. M. *Electrochim. Acta* **2009**, *54*, 2977–2982.

[201]Kushmerick, J.; Naciri, J.; Yang, J.; Shashidhar, R. *Nano Lett.* **2003**, *3*, 897–900.

[202]Selzer, Y.; Cabassi, M.; Mayer, T.; Allara, D. *J. Am. Chem. Soc.* **2004**, *126*, 4052–4053.

[203]Kim, Y.; Hellmuth, T. J.; Burkle, M.; Pauly, F.; Scheer, E. *ACS Nano* **2011**, *5*, 4104–4111.

[204]Malen, J. A.; Doak, P.; Baheti, K.; Tilley, T. D.; Majumdar, A.; Segalman, R. A. *Nano Lett.* **2009**, *9*, 3406–3412.

[205]Romaner, L.; Heimel, G.; Gruber, M.; Bredas, J.-L.; Zojer, E. *Small* **2006**, *2*, 1468–1475.

[206]Tavazza, F.; Levine, L. E.; Chaka, A. M. *Phys. Rev. B* **2010**, *81*, 235424.

[207]Zarechnaya, E. Y.; Skorodumova, N. V.; Simak, S. I.; Johansson, B.; Isaev, E. I. *Comp. Mat. Sci.* **2008**, *43*, 522–530.

[208]Li, X.-B.; Wang, H.-Y.; Yang, X.-D.; Zhu, Z.-H.; Tang, Y.-J. *J. Chem. Phys.* **2007**, *126*, 084505.

[209]Ohnishi, H.; Kondo, Y.; Takayanagi, K. *Nature* **1998**, *395*, 780–783.

[210]Hoft, R. C.; Ford, M. J.; Cortie, M. B. *Chem. Phys. Lett.* **2006**, *429*, 503–506.

[211]Reuter, M. G.; Hersam, M. C.; Seideman, T.; Ratner, M. A. *Nano Lett.* **2012**, *12*, 2243–2248.

[212]Muller, K. *Phys. Rev. B* **2006**, *73*, 045403.

[213]Gall, K.; Diao, J.; Dunn, M. *Nano Lett.* **2004**, *4*, 2431–2436.

[214]Park, H.; Zimmerman, J. *Phys. Rev. B* **2005**, *72*, 054106.

[215]Morozov, I. V.; Kazennov, A. M.; Bystryi, R. G.; Norman, G. E.; Pisarev, V. V.; Stegailov, V. V. *Comp. Phys. Comm.* **2011**, *182*, 1974–1978.

[216]Moon, B.; Jagadish, H.; Faloutsos, C.; Saltz, J. *IEEE Trans. Knowl. Data Eng.* **2001**, *13*, 124–141.

[217]Han, J.; Fang, L.; Sun, J.; Han, Y.; Sun, K. *J. App. Phys.* **2012**, *112*, 114314.

[218]Vazquez, H.; Skouta, R.; Schneebeli, S.; Kamenetska, M.; Breslow, R.; Venkataraman, L.; Hybertsen, M. S. *Nature Nanotech.* **2012**, *7*, 663–667.

[219]Guedon, C. M.; Valkenier, H.; Markussen, T.; Thygesen, K. S.; Hummelen, J. C.; van der Molen, S. J. *Nature Nanotech.* **2012**, *7*, 304–308.

[220]Markussen, T.; Stadler, R.; Thygesen, K. S. *Nano Lett.* **2010**, *10*, 4260–4265.

[221]Reuter, M. G.; Solomon, G. C.; Hansen, T.; Seideman, T.; Ratner, M. A. *J. Phys. Chem. Lett.* **2011**, *2*, 1667–1671.

[222]Demir, F.; Kirczenow, G. *J. Chem. Phys.* **2012**, *136*, 014703.

[223]Keith, J. A.; Fantauzzi, D.; Jacob, T.; van Duin, A. C. T. *Phys. Rev. B* **2010**, *81*, 235404.

[224]Jarvi, T. T.; Kuronen, A.; Hakala, M.; Nordlund, K.; van Duin, A. C. T.; Goddard, W. A., III; Jacob, T. *Eur. Phys. J. B* **2008**, *66*, 75–79.

[225]Jarvi, T. T.; van Duin, A. C. T.; Nordlund, K.; Goddard, W. A., III *J. Phys. Chem. A* **2011**, *115*, 10315–10322.